Simulating Many-Body States of Light & Matter with Tensor Networks

by

Jacob R. Taylor

A thesis
presented to the University of Waterloo
in fulfillment of the
thesis requirement for the degree of
Master of Science
in
Physics (Quantum Information)

Waterloo, Ontario, Canada, 2022

Author's Declaration

This thesis consists of material all of which I authored or co-authored: see the Statement of Contributions included in the thesis. This is a true copy of the thesis, including any required final revision, as accepted by my examiners.

I understand that my thesis may be made electronically available to the public after an embargo period.

Statement of Contributions

1. J. Taylor, J. Sinclair, K. Bonsma-Fisher, D. England, M. Spanner, K. Heshami, Generation of doubly excited Rydberg states based on Rydberg antiblockade in a cold atomic ensemble, arXiv. 1912.05675 (2019); under review at Phys. Rev. A.

2. J. Taylor, S. Goswami, V. Walther, M. Spanner, C. Simon, K. Heshami, Simulation of many-body dynamics using Rydberg excitons, Quantum Sci. Technol. 7 035016 (2022)

3. J. Taylor et al, Mesoscopic Scale Quantum Information Processing with Rydberg Atoms, in Preparation

4. **Chapter 3:** Y. Dong, J. Taylor, Y.-S. Lee, H. R. Kong, K. S. Choi. Waveguide-QED platform for synthetic quantum matter. Physical Review A, 104(5), 053703 (2021).

5. **Chapter 4:** J. Taylor, H. R. Kong, Y. Dong, K. S. Choi, Quantum phases of strongly-coupled many-body QED in reactive regime. arXiv:XXXX.XXXX (2022).

Abstract

When Feynman originally proposed the concept of a quantum computer, his purpose was to perform quantum simulation of complex materials. It is thus a key requirement that quantum resources can emulate physical processes that occur in nature. This is not only true for advancing our understanding of physics, but also for validating that these quantum devices work "at scale" in the first place. With recent developments, the realization of fully-controllable quantum devices of $N \sim 200$ qubits has become a reality. The memory requirements to store the state of such a device is soon to surpass the total memory capacities available on earth.

Given a physical state, full quantum-state tomography requires an exponential number of measurement basis for the characterization. Hence, it is also necessary to develop qualitative methods and phenomenology to make conclusive statements without direct access to the full physical state in the laboratory. One inherently useful aspect for this type of "benchmarking" is to understand quantum phases of low-energy states of a many-body system. Being able to simulate complex ground states is not only useful for discovery of novel phases of matter, but is also necessary requirement to validate the "supremacy" of a quantum device. Moreover, simulating physics on quantum devices currently is very difficult and, due to their noisy nature, untrustworthy. Both as a stop gap in device validation and in laboratory limitations where some access to the wavefunctions is required, improving the state-of-art methodology for classical simulation of many-body systems will remain an important direction in the foreseeable future. This thesis focuses mainly on state-of-art tensor-network toolboxes to simulate static and dynamical behaviours of highly-complex many-body systems, exemplified by both local and non-local properties of the quantum matter.

In chapter 1, I motivate the rest of the thesis and provide an introduction to the physics of cavity quantum electrodynamics (QED), and its generalized cousin, waveguide QED. In particular, I describe how the range of quantum phases can be expanded using local constraints and site-independent cavity modes. Finally, I provide a summary for the remaining chapters.

In chapter 2, I describe state-of-art numerical toolboxes to efficiently represent and manipulate quantum states, namely the tensor network method that controls the approximation of wavefunctions in an exponentially-large Hilbert spaces with the entanglement degree of freedom spread across a network of heavily sparse and compressed tensors. The crucial insight of these so-called tensor network states is discussed, where the approximation of the wavefunction is made by limiting its entanglement degree of freedom, also known as the bond dimension. We provide a physically relevant picture of the AKLT

representation of matrix product states (MPS) for the compressability and expressibility of most low-energy states of many-body systems in low dimensions, colloquially known as the area law of entanglement.

We describe two well-known examples for variational 1D-like tensor network states, known as MPS. The two prominent optimization toolboxes are the density-matrix renormalization-group (DMRG) and time-dependent variational protocol (TDVP), as well as their infinite-size variants. We conclude this chapter by discussing new methods of simulating open-system dynamics for many-body systems in the Markov limit using tensor network methods. The first is to perform a direct MPS-based quantum trajectory simulation of an open quantum system. The second is to create a new MPS representation of a vectorized density matrix for the open quantum system, and to determine the steady-state using DMRG-based methods.

In chapter 3, I provide an experimental protocol for generating universal quantum matter in a waveguide QED platform by coupling collective atomic motions of the trapped atoms to the continuum of waveguide modes. This spin-mechanical coupling generates universal (QMA-complete) 2-local Hamiltonian. Using this platform, we extend the methodology to generalized interacting SU(n) models. We describe several models implementable with the platform, such as the chiral spin liquids with DMI term, Kitaev honeycomb model, and an interacting SU(n)-model. I will discuss the application of tensor network states in emulating 1D SU(n)-spin chain across a quantum critical phase known as a quantum Luttinger liquid. This conformal phase, described by a Wess-Zumino-Witten (WZW) conformal field theory (CFT), is a proximate gapless spin liquid phase in one-dimensions. From this, we extract conformal data, such as the central charge and critical exponents from the physical spin model. Finally, we discuss the engineering challenge for realizing such a photonic crystal waveguide, including the effects of Casimir-Polder forces on the trapped atoms. We discuss a controlled renormalization procedure to obtain the gauge-invariant Hamiltonian analytically as well as the gauge-invariant matrix product state through the applications of isometric tensors. This chapter is largely based upon Ref. [1].

In chapter 4, I discuss how novel quantum phases can be created in strongly-coupled many-body QED. Reactive many-body QED for a chequerboard lattice generates a Rydberg ice coupled to the cavity back-action. The long-range quantum fluctuations disseminate dimer coherence across the system size, generating long-range entanglement. The "infinite-range" quantum fluctuations have a profound impact on the stability and projective symmetry group of the spin liquid state in a dynamical U(1)-lattice gauge theory. We discuss the physical model underlying this platform. We find that Higgs-condensation of scalar charges spontaneously breaks the U(1) gauge group to a Z2 sub-group. A genuine deconfined phase persists in this setting, enabling the exploration of topological order

within the Rydberg quantum ice. We discuss and utilize several methods for detecting quantum spin liquids. This work supplements our experimental observations, which will be discussed elsewhere. This chapter is largely based upon the Ref. [2].

Finally, in chapter 5, I provide an overview of future directions for this work. The utilization of tensor networks within a quantum device, so called quantum tensor networks, could offer deep insight to the physics of strongly-correlated quantum systems. This is utilized to the physics of many-body QED for dissipative universal quantum computation.

Acknowledgements

I would like to thank every co-author on the papers, and especially my supervisor Dr. Kyung Soo Choi. We have done some amazing things, and I have learned a lot with your help. Your prodigious knowledge and guidance were invaluable. I would also like to thank IQC and NSERC for the financial contributions.

Dedication

This thesis is dedicated to my mother, love you mom.

Table of Contents

List of Figures

List of Tables

Chapter 1

Introduction

Quantum information science offers new and exciting methods of processing data not feasible within classical systems. The most well-known example is Shor's algorithm, which allows the factoring of integer number in a polynomial time. Factoring of prime numbers is important, because modern commerce relies on RSA encryption, namely the exponential complexity of factoring on classical computers [3]. Another more direct and potentially disruptive use case is the utilization of quantum information to understand physical systems. Some examples include the expansion of our knowledge in the fundamentals of physics, such as holography and quantum gravity [4], the creation of stable quantum memories through topological spin liquids, or discovering new useful substances with quantum chemistry [5]. However, to bring any of these visions to fruition, we require the ability to understand, control, and describe quantum systems in some way [6].

Quantum states in their most general representation grow exponentially in their complexities as a function of their system size N. Even for a two-level qubits, a general state of only 300 qubits would require more classical bits than the number of nucleons in the observable universe. Thus, no matter how powerful classical computers could get, storing states of large system size N will always remain elusive [7]. Luckily, we can achieve a large class of challenging tasks without ever needing to represent the general wavefunction $|\psi\rangle$.

The first obvious situation is when we have a state that can be written as a sum of a handful of Fock-state basis. Instead of storing the full wavefunction, we only need to store the coefficients of the non-zero elements. If we keep track of what basis states correspond to which coefficients and truncate those basis states with very small coefficients, we could reduce the data required into a sparse form. We can even do this compression for the operators. In both cases, this is called a sparse matrix [8]. We could even compress the rows or columns to reduce the amount of data we need. This is the method used in common quantum optics packages like QuTIP [9].

Another common trick is to restrict your computational space to some global symmetry, such as conserving total S_z or particle number N [10]. Generally, for the utilization of global symmetry groups, one needs a Hamiltonian that conserves those global symmetries. When you have such conservation rules, it significantly reduces the computational Hilbert space. More often than not, these methods are not general, and can only serve to slightly expand the number of qubits that you could simulate.

Even in a simple 1D Heisenberg spin-chain with a total $S_z = 0$, the global conservation is insufficient to reduce the required Hilbert space for efficient computation with a large number of atoms. Moreover, mean field methods are only adequate for a set of semi-classical problems. Indeed, in all of these methods, the problem of exponential scaling has not been fixed, but only delayed to complex problems that do require the full non-sparse wavefunction.

One exception has been the discovery of quantum Monte-Carlo (QMC) methods. At its most fundamental core, QMC methods utilize the duality of the quantum Hamiltonian with a classical one, which can be efficiently described by a thermodynamic partition function. However, QMC is not a well-controlled method for solving the ground-state problem in computationally-complex Hamiltonians. Sign-problematic Hamiltonians (also known as non-stoquastic Hamiltonians) are the class of problems that pose the most difficulty in many-body physics. For these computationally-complex ground-state problems, it is no longer possible to maintain the positivity of the partition function and the statistical description of the theory breaks down. That is, there is no semi-classical probabilistic interpretation for the ground-state wavefunction, and prohibits the utilization of QMC updates and any of their related cousins. [11]

Luckily, there exists a physically-inspired unbiased numerical scheme for a large class of Hamiltonian and their long-range structure, known as tensor network states. In a tensor networks, instead of storing the macroscopic quantum state directly, one stores the state in a series of "site"-dependent tensors in an enlarged Hilbert space that can locally be manipulated. By not storing the wavefunction and only storing the tensors, the effective Hilbert space scaling can be reduced to polynomial scaling, and the tensors can be utilized for computing observables up to some cut off in the Schmidt decomposition. The control parameter for truncating the quantum state in the entanglement basis is known as the bond dimension [7]. Furthermore, tensor network states mimics the many-body low-energy wavefunctions, in that they inherit their entanglement structure from the local Hamiltonian. Furthermore, the properties of these tensor network states encode the long-wavelength information content in their bonds, enabling the computation of entanglement entropy [7] and, in more complex cases, the transfer matrices [12], as well as their full entanglement spectrum, which fully prescribes the low-energy excitations of the system.

Furthermore, tensor network states are not limited by simple sparse matrix constraints, whether they be matrix product states (MPS) [7] or projected entangled pair states (PEPS) [13], 2D generalization of MPS, or some other tensor network states (e.g., MERA) are still limited on a computational level to a class of states with geometrically-limited entanglement [14]. For a general highly-entangled state (e.g., excited states), tensor networks still require exponential scaling to represent them in their bond dimensions. However, as will be discussed in more detail in chapter 2, it can be shown that, for any gapped Hamiltonian with local interactions, the entanglement entropy that cut the ground state into two bipartitions depends only on the "surface area" of the physical cut [14].

Since we can use entanglement entropy as a proxy to determine the level of entanglement in the states, the "area" law of entanglement is a surprising manifestation [15]. To see this, let us remind that, first, the "area" of the cut scales based on the number of bonds cut. Second, the physical systems experience local interactions. As a result, tensor networks enable a wide range of problems to be solved numerically that would not otherwise be possible. Furthermore, even in some gapless systems, tensor networks can sometimes approach a reasonable approximation of the ground state to obtain their long-wavelength properties in certain calculations [16].

Regardless, there are still some systems in which high entanglement is intrinsic and can not be avoided. If one had a universal quantum computer, they could simulate most Hamiltonian with reasonable efficiency [17]. Let me just caution that the ground-state problem of some Hamiltonians is so complex that even a universal quantum computer would take an exponential number of step to simulate its ground-state energy. In addition, such a universal device appears to be a long way off. There is, however, a intermediate solution to perform the simulation of quantum systems with noisy devices, "analog quantum simulation".

The goal of quantum simulation is to use a well-controlled physical system to simulate the physics of another more complex quantum system. One simple reason why analog quantum simulators are easier to manipulate is because quantum simulators made with trapped ions [18] or Rydberg atoms [19] are often in micrometers size scales, while an electronic model in a solid or a molecule [5] can be on sizes of angstrom. The dynamics can also be slower on the simulator than the real physical system. This provides practical means to observe the evolution that would otherwise be too fast to do so [20]. The most important advantage of a quantum simulator is that it often allows models to be easily interrogated and controlled, in order to understand their finer details [6].

An example of this will be seen in the later chapter on the quantum simulation of spin liquids. Computing expectation values of Wilson Loops for a natural model is generally

incredibly difficult and, if not, impossible. Despite having several candidate substances that could realize a spin liquid, such as $(BEDT-TTF)_2Cu_2(CN)_3$ [21], $ZnCu_3(OH)_6Cl_2$ [22], and Na_4Ir_3O [23], actually performing the required measurements to validate their deconfinement is often not possible. Quantum simulators, on the other hand, can have direct access to non-local observables such as the Wilson loops via snap-shot based measurements.

1.1 Background on cavity QED

To introduce the concept of cavity QED [24], let us first try to understand the simple case of a single atom coupled to the single mode of an optical cavity. In this case, the atom will have two spin states $|g\rangle$ and $|s\rangle$, and a cavity field in the Fock-state basis states $|n\rangle$. Experimentally, the spin states are normally represented by the hyperfine ground states. The Hamiltonian for such a system can be understood as being comprised of three parts:

$$H_{atom} = \hbar\Delta_a\hat{\sigma}_+\hat{\sigma}_- \tag{1.1}$$

$$H_{field} = \hbar\Delta_c\hat{a}^\dagger\hat{a} \tag{1.2}$$

$$H_{int} = \hbar g(\hat{a}^\dagger\hat{\sigma}_- + \hat{a}\hat{\sigma}_+) \tag{1.3}$$

H_{atom} is the Hamiltonian of an isolated atom with no field, where σ_- is the spin lowering operator and σ_+ is the raising operator and Δ_a is the atomic detuning. H_{field} is the Hamiltonian of an empty single-mode cavity with detuning Δ_c. H_{int} is the interaction Hamiltonian between the radiation field and the internal state of the atom with coupling constant g. The resulting Hamiltonian

$$H_{JCM} = H_{atom} + H_{field} + H_{int} \tag{1.4}$$

$$H_{JCM} = \hbar\Delta_a\hat{\sigma}_+\hat{\sigma}_- + \hbar\Delta_c\hat{a}^\dagger\hat{a} + \hbar g(\hat{a}^\dagger\hat{\sigma}_- + \hat{a}\hat{\sigma}_+) \tag{1.5}$$

is known as the Jaynes-Cummings model [25].

This Hamiltonian can be solved exactly to obtain the dressed eigenstates and their respective energies for $n = 1, 2, 3...$ and $\delta = \Delta_c - \Delta_a$ [26]:

$$|\pm_n\rangle = \delta \pm \sqrt{4g^2n + \delta^2}\,|g, n\rangle + 2g\sqrt{n}\,|s, n-1\rangle \tag{1.6}$$

$$E_{\pm_n} = \frac{\hbar}{2}(2n\Delta_c - \delta \pm \sqrt{4g^2n + \delta^2}) \tag{1.7}$$

1.2 Dispersive cavity QED

Let us now see how a trivial many-body model might arise through the collective coupling to the radiation field. In the dispersive limit $\Delta_c \gg g, \Delta_a$, we can write the Hamiltonian as $H = H_0 + V$ where $H_0 = \hbar\Delta_c \hat{a}^\dagger \hat{a}$ and $V = \hbar\Delta_a \hat{\sigma}_+ \hat{\sigma}_- + \hbar g(\hat{a}^\dagger \hat{\sigma}_- + \hat{a}\hat{\sigma}_+)$ to treat V as a perturbation on the field. Looking at the vacuum $n = 0$ subspace, the cavity field can be adiabatically eliminated to produce an effective Hamiltonian for just the spin system:

$$H_{\text{eff}} = [\Delta_a + \frac{g_0^2}{\Delta_c}]\sigma_+\sigma_-. \tag{1.8}$$

This is precisely the Lamb shift modified by the large density of states within the cavity field.

Let us now see how this Lamb shift manifests into a many-body term when the system is expanded to a multi-atom model. Namely, let us now consider the Tavis-Cummings limit, where all atoms are equally coupled to a single-mode cavity as follows:

$$H_{\text{TCM}} = \hbar\Delta_c \hat{a}^\dagger \hat{a} + \sum_i \hbar\Delta_a \hat{\sigma}_+^{(i)} \hat{\sigma}_-^{(i)} + \hbar g(\hat{a}^\dagger \hat{\sigma}_-^{(i)} + \hat{a}\hat{\sigma}_+^{(i)}) \tag{1.9}$$

By repeating the perturbative process for the elimination of the cavity field, we realize now an all-to-all connected kinetic Hamiltonian:

$$H_{eff} = \sum_{i,j} [\delta_{i,j}\Delta_a + \frac{g_0^2}{\Delta_c}]\sigma_+^{(i)}\sigma_-^{(j)}, \tag{1.10}$$

where $\delta_{i,j} = 1$ if $i = j$ and $\delta_{i,j} = 0$. This kinetic term is nonetheless a single-particle Hamiltonian, as it can be described at a mean-field level by introducing a single classical parameter of collective operators $\hat{S}_\alpha = \sum_i \sigma_\alpha^{(i)}$.

1.3 Waveguide and many-body QED

Let us now consider two examples where cavity QED can be significantly enriched.

First, we can try to avoid the description at the mean-field level by somehow breaking the permutation symmetry of Eq. 1.10. In practice, one can try to achieve this by starting to introduce multiple cavity modes, transverse or longitudinal. The point here is that each atom couple with different amplitude and phase to different modes of the cavity. As such, as the cavity field is removed, the renormalized atom-atom interaction becomes

translationally-*variant*. This is the generalized regime of waveguide QED or multimode cavity QED.

The general philosophy here is that by modifying the electormagnetic vacuum surrounding the atom, it is possible to construct optical devices that renormalize the atom array with desired "single-particle" properties. Thus, waveguide QED can generate tunable range magnetism. In chapter 3, we exploit this property to stabilize a universal quantum matter within the waveguide QED toolbox.

In the second example in chapter 4, we can now turn to the question of transforming the "dielectric" substrate from a single-particle one to a many-body media. The quest here is to realize lattice spin models characterized by local symmetry.

As an example, the cavity QED Hamiltonian can be constructed to add a local constraint in the form of $H_{contraint} = \Lambda \sum_{\boxtimes} (\sum_{i \in \boxtimes} \hat{\sigma_z}^{(i)} - Q)^2$, where $\boxtimes$ are ice cells of sites in a checkerboard pattern (See Fig 4.2). This term can be readily implemented using spin-spin interactions such as the van der Waals interaction between Rydberg Atoms [27]. A more detailed process, along with the physical model will be discussed further in chapter 4.

$$H_{eff} = \sum_{i,j} [\delta_{i,j} \Delta_a + \frac{g_0^2}{\Delta_c}] \sigma_+^{(i)} \sigma_-^{(j)} + \Lambda \sum_{\boxtimes} (\sum_{i \in \boxtimes} \hat{\sigma_z}^{(i)} - Q)^2 \tag{1.11}$$

1.4 Summary of the chapters

This thesis will focus on developing numerical methods, particularly through the use of tensor networks for equilibrium and out-of-equilibrium systems, so methods for studying the properties of a system's steady state, or its excitations. The second chapter will consist of an overview of standard numerical methods involving tensor networks. The chapter will start with an overview of tensor networks, their diagrams (which will be used heavily) and their efficiencies. After which an explanation of the construction of matrix product states, matrix product operators, and the area law will be given. Two of those should give a basic understanding of the framework in which all the following computations will be done.

The chapter will then go into detail describing very standard algorithms used within tensor networks, such as the iterative method, the Density Matrix Renormalization Group (DMRG) [28]. DMRG is a very versatile and effective method for finding the ground state of a Hamiltonian and within it the construction of local subspace Hamiltonians. The infinite system variant of the DMRG algorithm called IDMRG will also be explained, which utilizes the translational invariance of the infinite system [29]. I will also discuss the Time-Dependent Variational Principle (TDVP) [30]. TDVP a method for performing

time evolution of a state, or more precisely, the action of an operator's matrix exponential. This distinction is relevant because this method will also be used to perform imaginary and complex time evolution.

Chapter 3 consists of a proposal for a waveguide quantum electrodynamics (QED) toolbox for universal quantum simulation. Essentially, entanglement is what limits the ability of tensor networks, so it's not surprising that it is also what gives quantum devices their power. It is the property of entanglement that allows a quantum computer to get exponential speed up in solving some problems [3]. A quantum simulator is a controllable quantum device that can be used to simulate other quantum systems of interest [6]. The toolbox in question allows general construction and thus simulation of SU(2) 2-body Hamiltonians.

This means Hamiltonians of the form $H = \sum_{i,j} \hat{h}_{i,j}$, where $h_{i,j}$ is an operator that acts only on sites i and j. The toolbox utilizes the coupling of spin-matter to atomic motion generated by "spin-independent" forces of the synthetic vacuum of the PCWs (Photonic Crystal Waveguide) to mediate the underlying long-range interactions. More specifically, we have spin states $ketg$ and $kets$, as well as collective vibrational motion, the Bogliobov modes. The Bogliobov modes, along with site-dependent Zeeman shifts and several site-independent programmable Raman fields, are combined to couple the spin to the Bogliobov modes. This allows one to remove the Bogliobov modes and generate an arbitrary two-site spin-spin interaction Hamiltonian. The constructed universal SU(2) 2-body spin Hamiltonian can then be extended to arbitary SU(N).

Here, the SU(2) spins are formed into logical blocks of N physical spins, with each block being mapped to a single SU(N) spin. This is accomplished by an energy constraint, so that, in the low energy subspace, the system forms an effective gauge constraint. In particular, each block has a major energy cost for any number of spins being excited except exactly single collective excitation. This works similarly to the principle of Rydberg blockade [1, 27], where additional excitation becomes energetically unfavorable.

The functionality of the toolbox is verified through the use of tensor network simulations. We compare computations done directly with a SU(N) Wess-Zumino-Witten (WZW) model to the emergent WZW model. This emergent WZW model arises from an isometric map of the low energy subspace of the SU(2) system of the toolbox. In particular, these two will be computed through a combination of MPS imaginary time evolution and DMRG. Furthermore, the process to convert these multi-site blockette SU(2) gauge constrained states to a SU(N) state using a tensor network isometric mapping will be detailed. Finally, some difficult numerical use cases for the toolbox relating to the strong coupling WZW model for SU(N) will be discussed.

The fourth chapter will consist of an investigation into model comprised of the interplay

between the QED fluctuation and local U(1) gauge constraints provided by Rydberg interactions. The phase diagram showed numerous exotic phases, ranging from superradiant phase, to a family of valence-bond crystals (stripe and plaquette), and to topological and conformal phases. In particular, we found that it is possible to stabilize a Z2 topological spin liquid in the many-body QED platform.

Interestingly, this phase corresponds to the Higgs phase of the U(1) gauge theory, which breaks down the local conservation to Z2 gauge symmetry by way of the long-range cavity-mediated interactions. Furthermore, we find signatures of a deconfined spin liquid described by a QED3 CFT. In this work, the numerics were used to support the existence of these phases. This ranges from obtaining operational metrics for topological and CFT entanglement entropy, decay of correlation functions, and the scaling behavior of Wilsonian loops in both the deconfined and confined phases. Furthermore, we have constructed the modular matrices, encoding the full braiding statistics of the anyons in the Z2 spin liquid phase.

The thesis will then conclude with the chapter 5. I will provide a prospective to future work from the concepts and tools developed in this thesis.

Chapter 2

Numerical Methods

2.1 Introduction to tensor network representation

A tensor $T_{i_1,i_2,...}$ is just an array of values where each address in the array is specified uniquely by a series of index values $i_1, i_2, ...$ The number of elements within a tensor is determined by the dimensionality of each index $dim(T) = dim(i_1) * dim(i_2)....$ The number of indices of a tensor is called its "rank", and it can have any number including 0. A rank 0 tensor is a scalar, rank 1 a vector, rank 2 a matrix and 3 can be thought of as a 3-dimensional array of values. We can diagrammatically represent these tensors with tensor network diagrams [31] that consist of boxes and lines. Where each box is a tensor with the number of lines coming off the box determining the rank of the tensor. So a box with 1 line is a vector, two lines are a matrix, and so on. A tensor can have its indexes connected. These tensors use a built-in index summation convention, where repeated indexes are summed over. This summing is called "contracting the tensor". Two tensors connected by a line is used to represent two tensors sharing an index. For instance, the below diagram represents $\sum_i A_{i,j} B^l_{i,k}$:

The previous sum can generate a new tensor with a rank equal to that of the number of "free" indexes, so, $M^l_{j,k} = \sum_i A_{i,j} B^l_{i,k}$. A tensor series of connected tensors forms a tensor network. A network of connected tensors can always be contracted by a single tensor. This single tensor will have indices the same as the free indices of the network. This thesis henceforth will make use of summation notation, where summations over shared indices are assumed, so $M^l_{j,k} = A_{i,j} B^l_{i,k}$.

2.2 Scaling of contractions

The efficiency of a contraction of several indices is dependent on the order in which it is performed. The difference between contracting indices in one order vs. another is often the difference between polynomial and exponential scaling. A general contraction between two tensors has an efficiency dependent on the number of elements that you must sum to do the contraction. For example, the contraction of the tensor in Fig.2.1 between the tensors $A_{i,j}$ and $B^l_{i,k}$ over i, would require summing a total of $dim(j) * dim(i) * dim(k) * dim(l)$ elements.

To illustrate the importance of contracting in a particular order, Fig. 2.2 and Fig. 2.3 show two different methods of contracting a grid-patterned $2 \times N$ tensor network. Both, when fully contracted, should give us a c-number. That particular tensor network is the same one used, as we will see later, for the inner product of two states. The first contraction scheme in Fig. 2.2 has a computational complexity of $O(NpD^2)$ [31], Fig. 2.3 scheme has $O(p^N)$ where p is the dimensionality of the site indexes, and D is the dimensionality of the link indexes. Merely by choosing to contract your sites in a particular order, you achieve an exponential speedup in the computational time required, thus illustrating its importance.

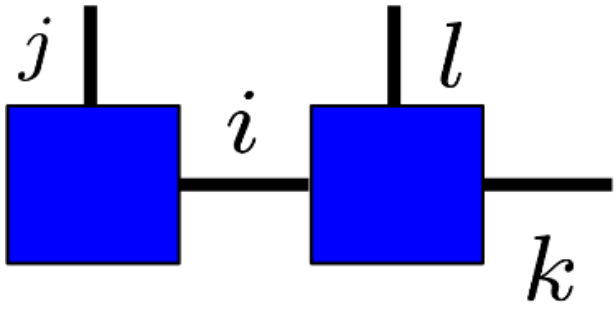

(a)

Figure 2.1: Diagram of $\sum_i A_{i,j} B^l_{i,k}$

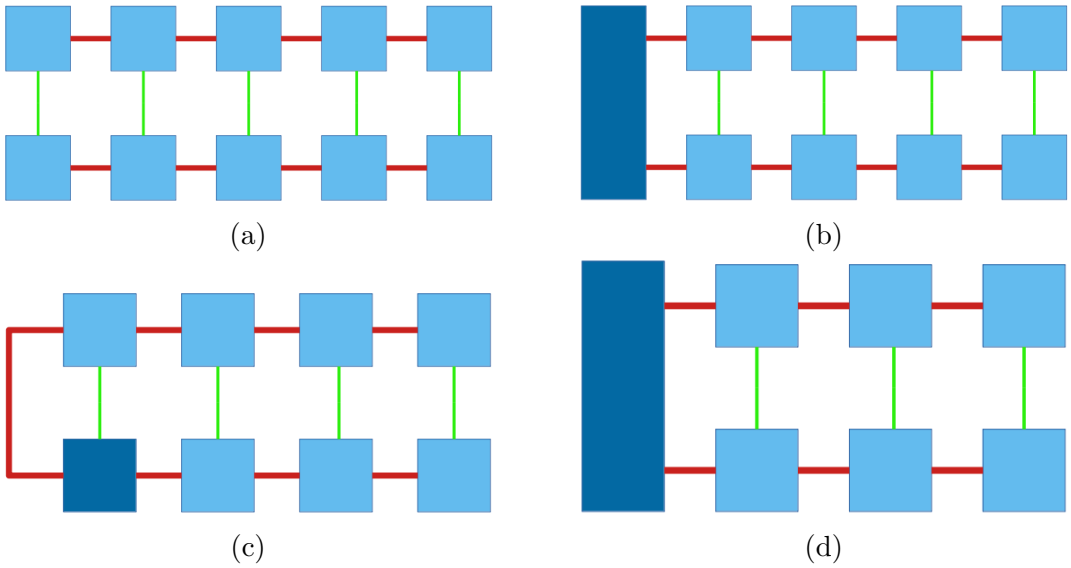

Figure 2.2: Ideal scheme for contracting a 2 by N grid tensor network. This is equivalent to the inner product of two MPS where the red lines are called the links index and have a dimensionality of D, while the green is site indexes and have a dimensionality of p. Following steps (a) to (d) the computational complexity can be seen to be $O(NpD^3)$ which is determined from the hardest step (going from c to d). Steps (b) to (d) repeat until all the sites have been contracted.

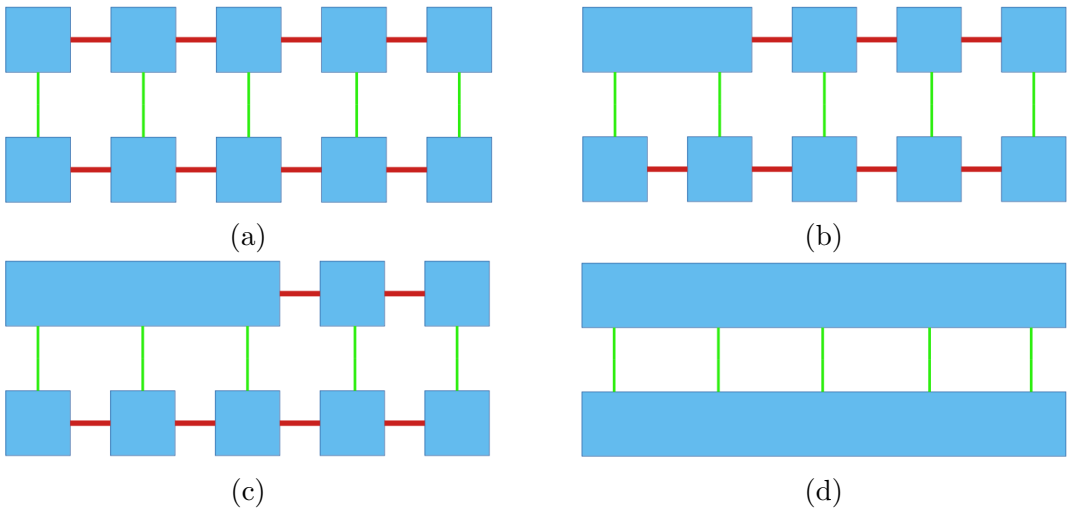

Figure 2.3: An alternative scheme for contracting a 2 by N grid tensor network. (a) to (d) illustrate the process of contracting length-wise on each row, finally contracting the whole thing to get a c-Number. This network is equivalent to the inner product of two MPS where the red lines are called the links index and have a dimensionality of D, while the green is site indexes and have a dimensionality of p. Contracting all the sites length-wise on each line gives a computational complexity of $O(p^N)$ scaling exponentially with the length of the network (seen in (d)).

2.3 Matrix product states

The matrix product state (MPS) is an example of a 1D tensor network state. MPS represents a state under the case of relatively low entanglement entropy in an extremely compressed manner. This is particularly applicable to the case of 1D Hamiltonian such as the one we used. The standard definition of the matrix product for an n qudit state is [14]:

$$|\psi\rangle = \sum_{s_1,...s_N} \mathrm{Tr}\left(A^{(1)}_{s_1} A^{(2)}_{s_2} ... A^{(n)}_{s_n}\right) |s_1, ..., s_n\rangle \tag{2.1}$$

where $A^{(k)}_i$ is a square matrix, of dimensions χ by χ, s_i goes from {1, 2, ..., d} and goes d is the number of dimensions of the local site (i.e. 2 for a qubit, 3 for qutrit, etc) [31]. What is critical about the matrix product state is how efficiently it can represent information. For a generic state, the matrix product representation only needs a total of $nd\chi^2$ values [31]. If we assume a constant χ this would have linear scaling, as opposed to a standard basis representation which requires a total of d^n values.

The matrix product state is thus limited in its utility by the scaling of the χ^2 parameter. For a general quantum system, its scaling is exponential, so in practice saving you nothing. However in the case of a local gapped Hamiltonian consisting of only nearest neighbour interactions, $\hat{H} = \sum_{i,j} \hat{h}_{i,j}$, the entanglement entropy for the ground state scales based on the number of local bonds cut/the area of the cut [32]. So for say a line of atoms, χ^2 would scale like $O(1)$. This is because, as will be discussed, χ^2 is the result of Schmidt decompositions [32], which is directly related to entanglement entropy.

Let us see how to construct a matrix product state. To begin, say you have a state within the Hilbert space $H_a \otimes H_b$, where H_b has dimension D and H_a has dimension $d < D$. The state can be written as:

$$|\psi\rangle = \sum_{k=1}^{\chi} \sqrt{p_k} \, |A_k\rangle \, |B_k\rangle \tag{2.2}$$

where χ is the Schmidt rank, which is at most $\chi = d$, and $\sqrt{p_k}$ is the singular value of the Schmidt decomposition. The Schmidt decomposition is done by performing a singular value decomposition, on the boundary where one wishes to split the Hilbert space [33]. To construct the matrix product state, one performs a repeated Schmidt decomposition $n - 1$ times [33]. The exact process can be seen below in the following tensor diagrams. However, the below diagrams will do so using an equivalent but numerically more efficient definition for the MPS where $A^{(k)}_{s_k}$ need not be square matrices but are instead χ_i by χ_{i+1}. The trace is often also integrated directly into the matrices by having $A^{(1)}_{s_1}$ and $A^{(N)}_{s_N}$ be 1 by χ_2, and χ_N by 1 respectively, such that they achieve a quadratic form equivalent to

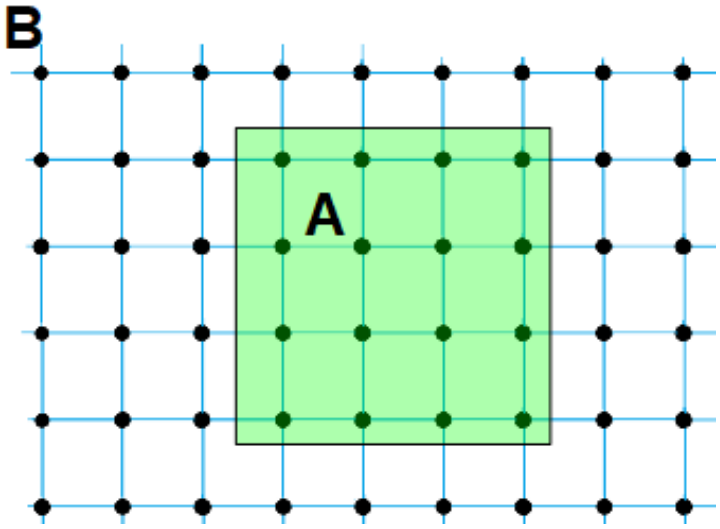

(a)

Figure 2.4: Diagram of Area Law. The area states that the entanglement entropy between systems A and B scales based on the number of bonds broken by the separation. In this case, it scales based on the perimeter of A.

it. It should be easy to see that by just taking χ to be the largest of χ_i that our above scaling arguments still hold. Writing $|\psi\rangle$ in this equivalent formulation of the MPS with the matrix $A^{(k)}_{s_k}$ being represented with tensors $A^{(k)}_{s_k,b_k,b_{k+1}}$ gives us:

$$|\psi\rangle = \sum_{s_1,...,s_N} A^{(1)}_{s_1,b_2} A^{(2)}_{s_2,b_2,b_3} ... A^{(N-1)}_{s_{N-1},b_{N-1},b_N} A^{(N)}_{s_N,b_N} |s_1, ..., s_N\rangle \tag{2.3}$$

To see why these two forms are equivalent, notice that each terms of the trace $\vec{e}_i^T A^{(1)}_{s_1} ... A^{(N)}_{s_N} \vec{e}_i$ can be contracted such that $A'^{(1,i)}_{s_1} = \vec{e}_i^T A^{(1)}_{s_1}$ and $A'^{(N,i)}_{s_N} = A^{(1)}_{s_N} \vec{e}_i$. This state is then already in the more efficient form. So to compute the full MPS, all we are doing is just summing MPSs (which can be done efficiently [28, 34]). Generally, you do not want to do this and instead just start with the state in this more efficient way.

The Matrix Product Operator (MPO), on the other hand is the operator equivalent to the MPS state; it, much like the MPS, is computed using repeated singular value decompositions. The process is essentially identical to that in Fig. 2.5 after replacing the state with a operator.

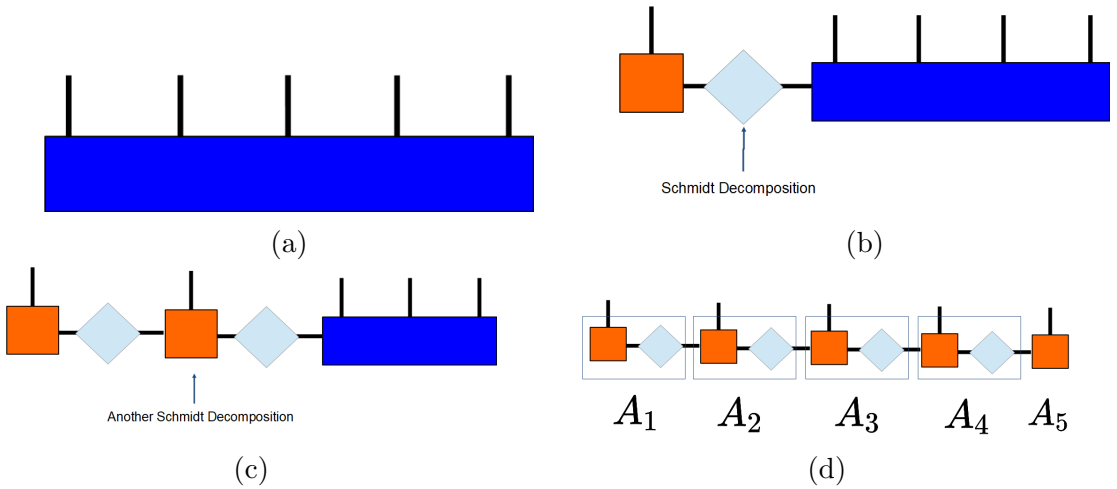

Figure 2.5: Diagrams for Construction of Matrix Product State, (a) start from a generic state written $|\psi\rangle = \sum_{i,\ldots,k} \alpha_{i,\ldots,k} |i\rangle \ldots |k\rangle$. (b) At the first site, perform a Schmidt decomposition (using a singular value decomposition) (c) perform a Schmidt decomposition on the remaining state splitting at the second atom. (d) Repeat for each site, then use the left tensor to contract the singular values. This will form the matrices that make up the MPS.

2.4 Notes on orthogonality sites and local gauging

Often, it is convenient to contract the singular values of a MPS such as to utilize the properties of the singular value decomposition. By doing so, you can maximize the orthogonality, moving the singular values to a specific site. Given some matrix M, there exists a $M = UDV^\dagger$, where U is said to be left unitary and V is right unitary. To "orthogonalize" a state, contract the first two sites and perform a singular value decomposition of the tensor to $UDV^\dagger$, and replace site 1 of your $|\psi\rangle$ with U_1 and site 2 with $DV_2^\dagger$. After that, repeat for site 2 and replace site 3 with $DV_3^\dagger$, and so on until you reach the last site N. We then can say that the "orthogonality core" is on the N-th site or the state is "gauged" to the N-th site. It is easy to see that one can contract sites $N-1$ and N again replacing site $N-1$ with $U_{N-1}D$, site N with V_N to move the orthogonality core to $N-1$, and so on [34].

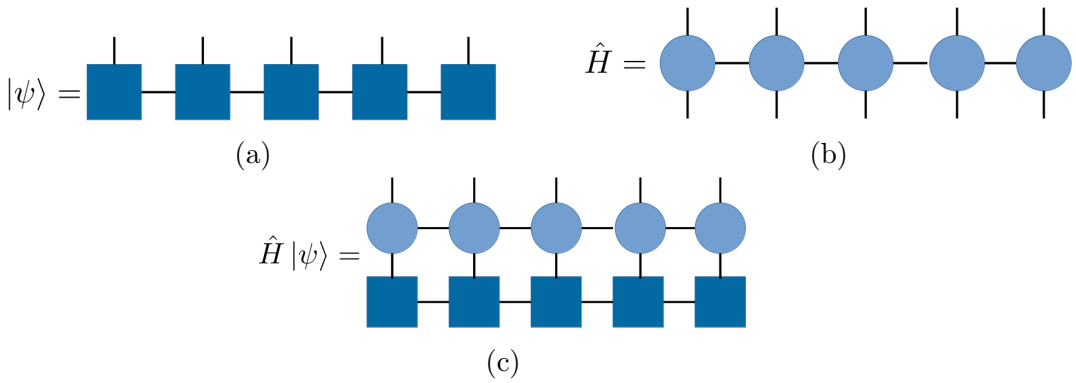

Figure 2.6: Example Tensor Diagrams for MPS and MPO. (a) A standard finite MPS tensor network. Each tensor represents the matrix for a respective site, the loose hanging index is the computational basis or site basis and is how one interacts with the state. The indexes connecting the tensors are called link indexes. The bond dimension is the maximum link dimension on a MPS and is normally the limiting factor in using an MPS for computation. For a general state, the bond dimension scales exponentially with the size of the Hilbert space, luckily though for some systems this is not so. (b) An example of a finite MPO tensor network. The parts of the MPO network are named similarly to the MPS, except that an operator can be applied from the left or right, so it's important to match the correct site indexes when applying an MPO to a MPS (c) Example of tensor network for the application of MPO operator to MPS $\hat{H}\,|\psi\rangle$

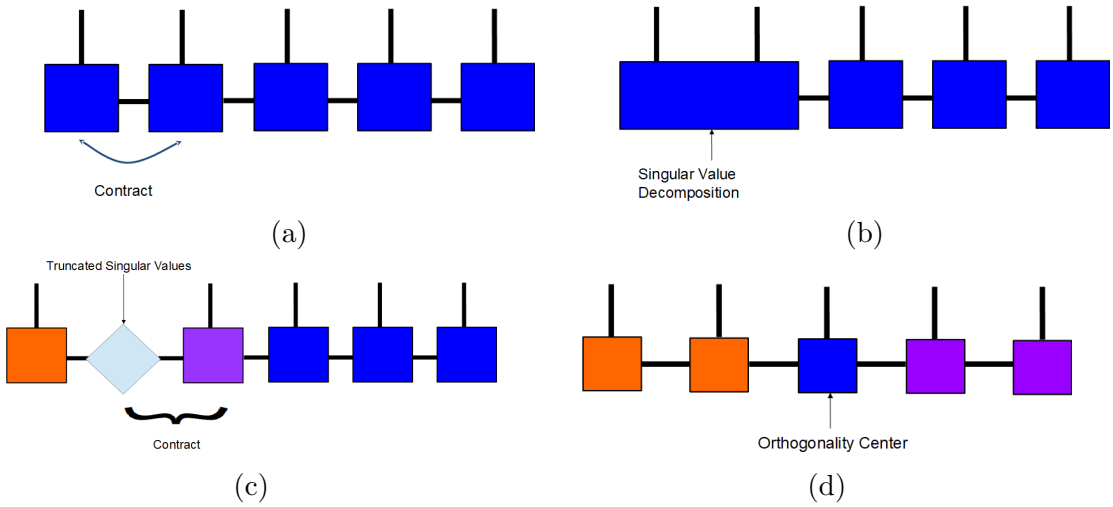

Figure 2.7: Orthogonality diagrams. The process for constructing an orthogonalized MPS is gauged to the centre, where orange is used to represent left orthogonal matrices and purple for right orthogonal. The process consists of contracting (a) the first two sites, (b) performing a singular value decomposition and contracting the singular matrix with the right site, and (d) repeating from both the left and right such that the orthogonality is moved to the desired position.

The utility of gauging the MPS can be seen when computing the inner product of a

local operator. Since $A^\dagger A = 1$, you can trivially contract those connections away from your tensor network and thus only have to compute the contraction for the local sites. This can be seen below:

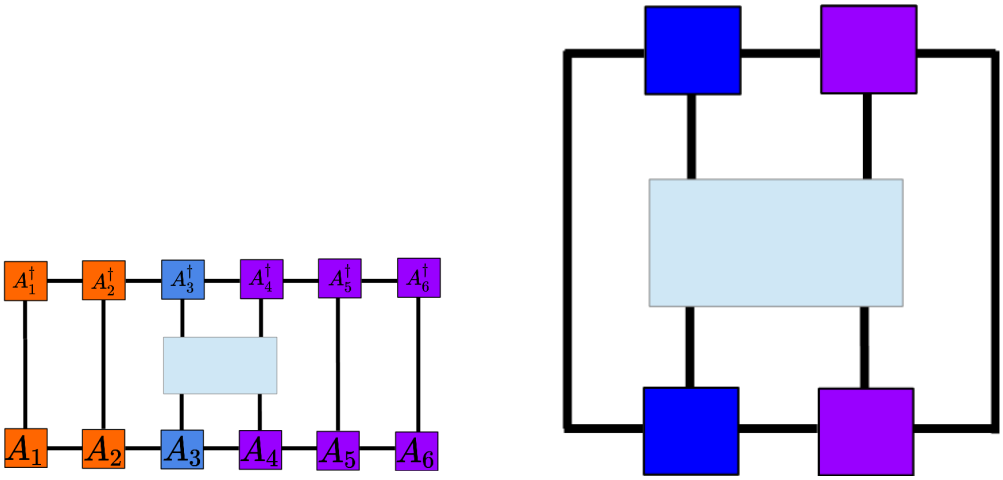

(a) (b)

Figure 2.8: Diagrams for the tensor inner product. Diagram of inner product $\langle\psi| M |\psi\rangle$ where M is a local operator. Left orthogonal and right orthogonal operators in (a) when contracted with their corresponding conjugate pair simplify to 1, and thus can be contracted to an empty link in (b). This allows one to very efficiently calculate expectation values of local operators with an MPS.

2.5 Density-matrix renormalization group and their infinite-size variant

Density Matrix Renormalization Group (DMRG) and its infinite variant, infinite-size (uniform) DMRG, are variational methods to obtain the ground state of a low-dimensional Hamiltonian. To start, let us look at the simpler finite-size and translationally-variant version. This method requires you to first have your Hamiltonian in the form of a matrix-product operator (MPO) and an initial guess state (ansatz) in the form of a MPS, such as a local random MPS state.

By definition, variational methods consist of varying your state $|\psi\rangle$ such to minimize $\langle\psi| H |\psi\rangle$ [35]. DMRG works in the same manner except that, instead of varying the entire state as one would in naive gradient descent, one varies a two-site tensor by modifying the local gauge projection. The two site tensor $A_{i,i+1} = A_i A_{i+1}$ is comprised of a contraction between sites i and $i+1$ of your MPS $|\psi\rangle = A_1 A_2 ... A_N$. This should be done while ensuring that the orthogonality core was initially on the ith site. In short, the DMRG algorithm

works by minimizing the energy functional on a local subspace Hamiltonian (that is more manageable), while keeping the rest of the tensors constant. It does this, by iterating over all the sites, "sweeping" back and forth until convergence. To begin, one starts with constructing the tensor(s) that together will form the local Hamiltonian.

The local subspace Hamiltonian $H_{eff}^{i,i+1}$ is a tensor that acts identically to the full Hamiltonian $H = H_1...H_N$ but only outputs the result for a local subspace. Its tensor network is similar to the inner product $\langle\psi| H |\psi\rangle$, except that the state's tensors are missing for the ith and $(i+1)$th sites (where i and $i+1$ are the two sites you are iterating over currently). From the left contract the inner product one site at a time to generate left boundary tensors $L_1 = A_1 H_1 A_1^\dagger$ to $L_{i-1} = L_{i-2} A_{i-1} H_{i-1} A_{i-1}^\dagger$, and similarly from the right to generate $R_N = A_N H_N A_N^\dagger$ to $R_{i+1} = R_{i+2} A_{i+1} H_{i+1} A_{i+1}^\dagger$. The local Hamiltonian operator is $H_{eff}^{i,i+1} = L_{i-1} H_i H_{i+1} R_{i+2}$ where H_i and H_{i+1} are from the Hamiltonian MPO $H = H_1 H_2 ... H_N$. The local operator made from the combination can then be applied to $A_{i,i+1}$ to give you the local action of the Hamiltonian. Depending on your local solver you may never need to compute H_{eff} and instead feed the result of its action directly into your solver [34].

This entire process can be seen Fig. 2.9.

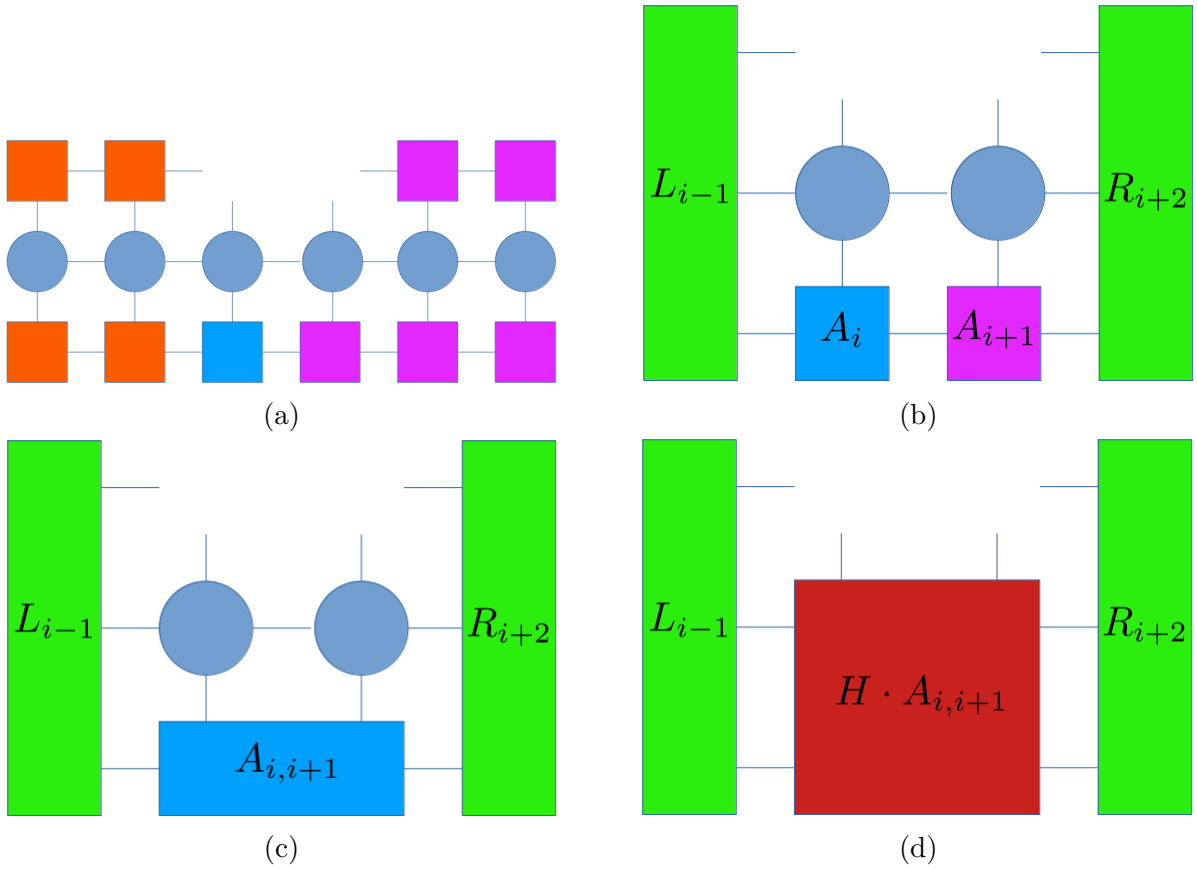

Figure 2.9: Steps of the finite DMRG (a) The full action of the local hamiltonian operator. (b-c) The action of the local hamiltonian operator after contracting the edge tensors and the sites. (d) the action of the local hamiltonian operator on sites i and i+1. This will be fed into a iterative solver completing a step of the DMRG. This process repeats for all the sites from the left, then right completing a sweep of which there may be many required to achieve convergence.

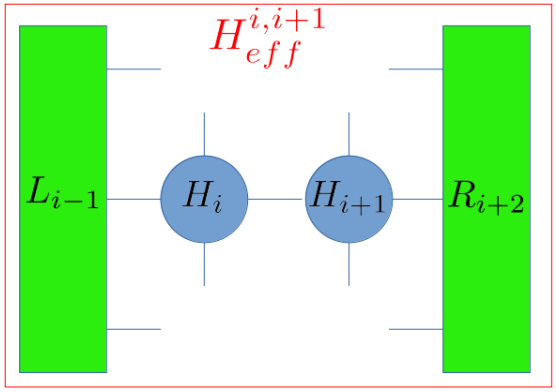

(a)

Figure 2.10: Example of tensor network for H_{eff}, this should ideally never actually be constructed and instead action should be used within the eigensolver instead. This network is equivalent to $H_{eff}^{i,i+1} = L_{i-1}H_iH_{i+1}R_{i+2}$.

After generating a method of efficiently computing $H \cdot A_{i,i+1}$ you can feed this into an iterative eigensolver to partially minimize the energy and give you an updated $A'_{i,i+1}$. There are multiple solvers one can use, such as the Davidson [28], Lanczos [36] and in some unique cases, Arnoldi [37, 38], however, the norm is to use the Davidson method. Generally, you don't want to fully converge for this local $A'_{i,i+1}$ as this is only the optimal for that site if none of the other sites in the MPS changes, which they likely will as modify the other sites.

To retrieve the MPS site tensor merely perform a singular value decomposition on $A_{i,i+1}$ to get U_iDV_{i+1}, and replace the state $|\psi\rangle$'s MPS for site i with U_i and site i+1 with the contraction DV_{i+1} doing this will move the orthogonality core one forward. Having done so you've completed the Davidson (or your chosen algorithms) iteration for the ith site. To move to the i+1 site contract L_{i-1} with H_i, M_i and M_i^* to generate L_i. We've already computed R_{i+3} H_{i+1},H_{i+2} thus giving us everything we need for the local Hamiltonian for $i+1$ starting site, allowing us to use our eigensolver for $i+1$. The DMRG then consists of applying Davidson iterations for two site pairs from left to right (1 and 2 then 2 and 3, ...) then right to left (N and $N-1$ then $N-2$ and $N-3$, ...), over and over again until you're satisfied with the convergence. Each left to right, then right to the left set of iterations is called a sweep, and generally, it takes several sweeps to converge, however, the more critical limiting factor for difficult models is in the allowed bond dimension when you truncate in the SVD.

The best models for DMRG are those that do not require a high bond dimension to get a small truncation error. It should however be mentioned that DMRG is biased towards certain states, particularly those of lower entanglement which in some cases can cause

problems [28].

The infinite DMRG (IDMRG), works similarly to the DMRG but takes advantage of the translational invariance in the infinite system [29]. The process begins by performing some small number of DMRG sweeps on a state consisting of two unit cells using a translationally invariant Hamiltonian to give us our starting state. These unit cells can have any number of sites ≥ 2 each. To illustrate the IDMRG process let's look at a 4-site state consisting of 2 sites for each unit cell. The state is then gauged towards the centre with the singular value matrix for the 1st IDMRG sweep Λ_1 being uncontracted in the centre. At this point the state is doubled, so that the 2 unit cells (4 sites) become 4 (8 sites), which are then contracted to make the boundary tensors like before. To do this contract the inner product of the left half of the first unit cell (excluding Λ_1) with the left Hamiltonian cap to make H_L, similarly for the right half to make H_R. At this point, one subtracts the energy from the previous (in this step finite) DMGR from H_L to only have the energy of the 4 site state be included. With the new 2-unit cell state and the edge environment tensors $L_0 = H_L$ and $R_{N+1} = H_R$, perform the DMRG sweep.

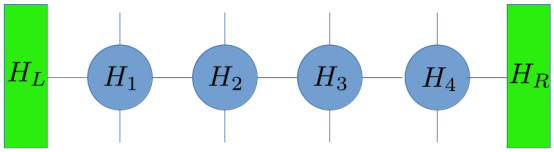

(a)

Figure 2.11: The translationally invariant hamiltonian MPO, this MPO is constructed in a way to allow one arbitrarily extension by stitching 1st site to the Nth site, and merely having caps on either side after achieving the desired size.

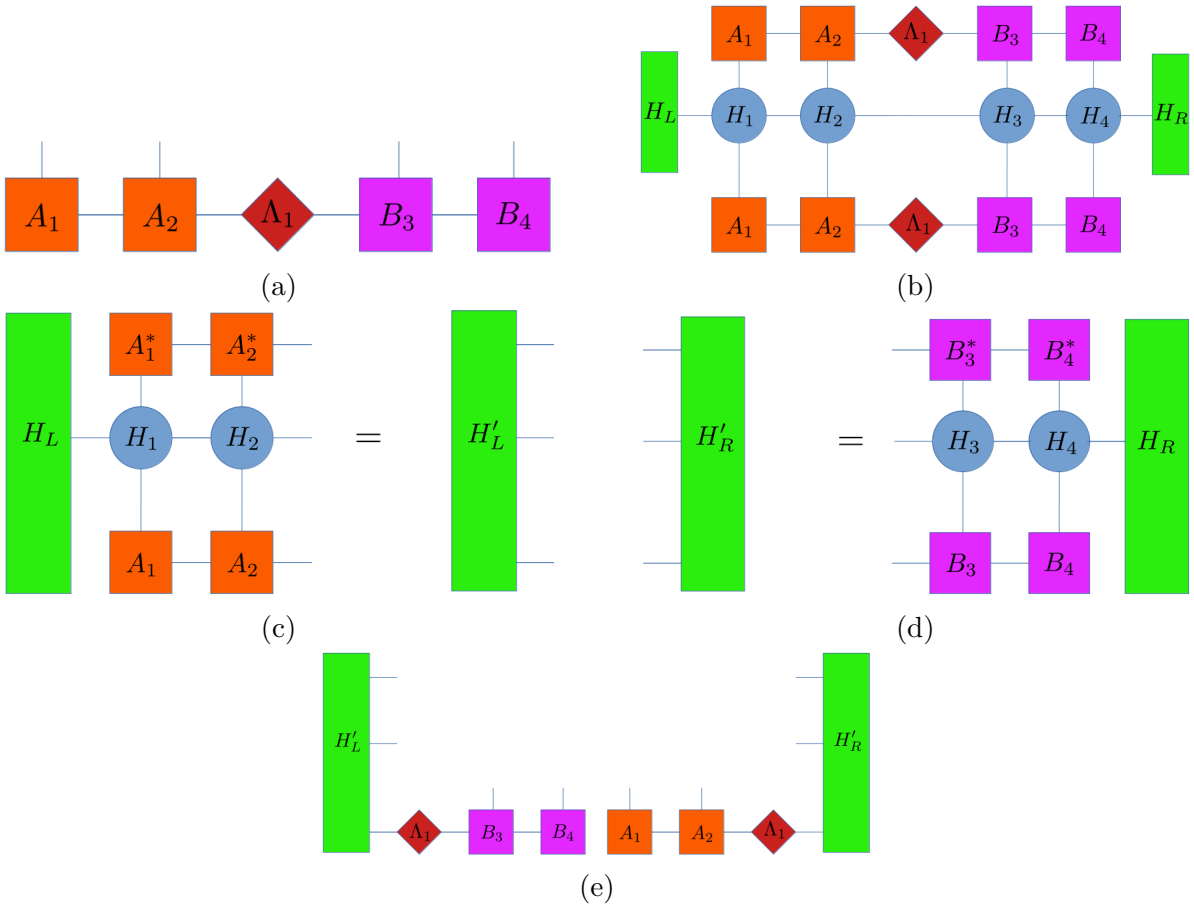

Figure 2.12: Illustration of the steps of the IDMRG algorithm. (a) The initial finite state seeded into the IDMRG. (b) $\langle\psi|\, H\, |\psi\rangle$ for the initial state where H_L and H_R are merely trivial edge tensors caps initially to terminate the infinite hamiltonian giving a finite version. If the Hamiltonians MPO is constructed in a upper trianglular format it will be the first and last basis vectors for the matricies of sites 1 and N. (c) The updated H_L after completing the first sweep. (d) The updated H_R after completing the first sweep. (e) The next IDMRG state with the respective environment tensors that will be contracted with the local hamiltonian and have the Davidson iterations applied.

After this, the process repeats except when you insert your new unit cell, instead of having nothing between them in the initialization multiplied by the inverse of the previous sweeps singular values Λ_{N-1}^{-1}. This wasn't needed before as there was a free hanging index. You can also use this to assess whether convergence has been achieved as you should find that $\langle\Lambda_{N-1}\rangle\,\Lambda_N = 1$ for the converged translationally invariant state [29].

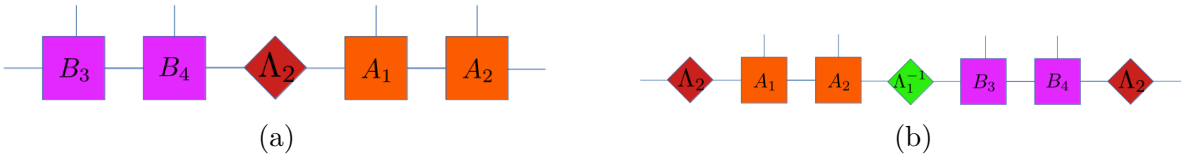

(a) (b)

Figure 2.13: (a) IDMRG's $|\psi\rangle$ after the first sweep (b)(a) IDMRG's $|\psi\rangle$ after the second sweep, noticing the insertion of Λ_{N-1}^{-1} inbetween the two unit cells. This same format is repeated for all subsequent sweeps, though possibly with $\Lambda_N B_3 B_4 \Lambda_{N-1}^{-1} A_1 A_2 \lambda_N$ instead of $\Lambda_N A_1 A_2 \Lambda_{N-1}^{-1} B_3 B_4 \lambda_N$ depending on whether the sweep number is odd or even.

2.6 Time-dependent variational principle

The time-dependent variational principle (TDVP) [39] is a method of evolving a finite MPS in time. It works by calculating the action of the exponential of some MPO e^{tH} on a MPS $|\psi\rangle$. As such it can solve both evolutions in real and imaginary time. There are multiple variants but the version that will be described here is the simplest to understand the 2-site TDVP (2TDVP). The 2TDVP method is very similar to the finite DMRG; in it, you solve for a local subspace of 2 sites at a time (i and $i+1$) sweeping back and forth. The Davidson iterations are replaced with Krylov iterations which solve for $e^{\frac{iH\delta t}{2}}$ locally. The only real difference however is that each iteration must generate a subspace for a single site $i+1$ in which a corrective backwards time step of $e^{\frac{-iH\delta t}{2}}$ is applied. This is done to prevent inner sites from being stepped twice.

I will now outline the entire algorithm in detail. First initialize $i = 1$, your initial state $|\psi\rangle = A_1 ... A_N$ and the Hamiltonian MPO $H = H_1 ... H_N$. To evolve $|\psi(t)\rangle = \exp(iHt)\,|\psi(t)\rangle$ to $|\psi(t+\delta t)\rangle$ perform a right half sweep, followed by a left half sweep. Combined these are called a sweep. The 2TDVP is sweeping over and over until a desired final time is reached. The right half sweep is performed as follows:

1. Set the orthogonality core of $|\psi\rangle$ and H to i.
2. Calculate the boundary tensors $L_{i-1} = \prod_{j=1}^{i-1} A_j H_j A_j^\dagger$ and $R_{i+2} = \prod_{j=i+2}^{N} A_j H_j A_j^\dagger$ and the site contraction $A_{i,i+1} = A_i A_{i+1}$.
3. Compute with $\exp(\frac{iH_{i,i+1}\delta t}{2}) A_{i,i+1}$ with the Krylov subspace method and set $A_{i,i+1}$ to the result.
4. Perform Singular value decomposition $A_{i,i+1} = U_i D V_{i+1}$, set $A_i = U_i$ and $A_{i+1} = DV_{i+1}$ (this moves the orthogonality core to $i+1$.

5. Calculate and update boundary tensor L_i.

6. Compute with $\exp(\frac{-iH_{i+1}\delta t}{2})A_{i+1}$ with the Krylov subspace method and set A_{i+1} to the result.

7. Repeat the above steps iterating i from 1 to N-1, this is a right half sweep.

The left half sweep is similarly performed as follows:

1. Set the orthogonality core of $|\psi\rangle$ and H to i.

2. Calculate the boundary tensors $L_{i-1} = \prod_{j=1}^{i-1} A_j H_j A_j^\dagger$ and $R_{i+2} = \prod_{j=i+2}^{N} A_j H_j A_j^\dagger$ and the site contraction $A_{i,i+1} = A_i A_{i+1}$.

3. Compute with $\exp(\frac{iH_{i,i+1}\delta t}{2})A_{i,i+1}$ with the Krylov subspace method and set $A_{i,i+1}$ to the result.

4. Perform Singular value decomposition $A_{i,i+1} = U_i D V_{i+1}$, set $A_i = U_i D$ and $A_{i+1} = V_{i+1}$ (this moves the orthogonality core to i.

5. Calculate and update boundary tensor L_i.

6. Compute with $\exp(\frac{-iH_i\delta t}{2})A_i$ with the Krylov subspace method and set A_i to the result.

7. Repeat the above steps iterating i from 1 to N-1, this is a right half sweep.

It is also often useful to do what is called a subspace expansion [30] to your state. In many cases, it will allow the TDVP to work better, particularly for very low link dimension states. This however will not be discussed here because more important for the 1TDVP method.

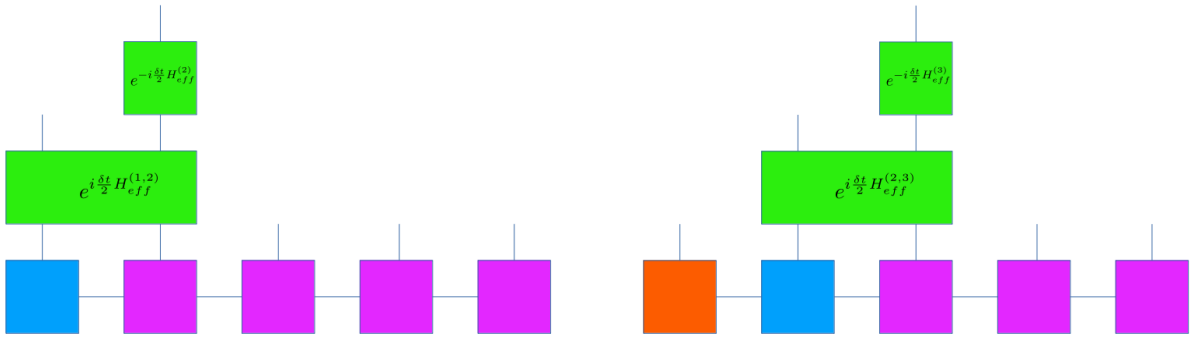

(a) (b)

Figure 2.14: First two substeps of the 2TDVP, it should be noted that this diagram is slightly misleading since only the action of the exponentials is computed not an actual MPO

2.7 Driven-dissipative quantum dynamics

2.7.1 Master equation and stochastic Schrodinger equation

For open systems, the Schrodinger equation with a system Hamiltonian is often not sufficient to explain the dynamics, while it is also often too difficult to model the environment. Luckily mostly isolated systems generally have the environment operate in a manner as to only weakly entanglement with the systems state. This allows us to model the random process as a Markovian chain. A Markov chain is essentially a random process where the likelihood of some event affecting the system (such as dissipation) is dependent only on the current state of the system [40]. This is particularly important when discussing dissipation into the environment which has to be modelled using the master equation. Since we are dealing with a probabilistic state or mixed state we must model the system using a density matrix. The most general form of the quantum master equation is as follows [41]:

$$\dot{\rho} = \mathcal{L}(\rho) \tag{2.4}$$

$$\mathcal{L}(\rho) = \frac{1}{i\hbar}[H, \rho] - \sum_l \frac{\gamma_l}{2}(\hat{K_l}^\dagger \hat{c_k}\rho + \rho \hat{K_l}^\dagger \hat{K_l} - 2\hat{K_l}\rho\hat{K_l}^\dagger) \tag{2.5}$$

where $\hat{K_l}$ are the quantum jump operators, γ_l are the dissipation rates and we call $\mathcal{L}$ the Lindbladian super-operator. A simple example of this would be a single 2-level atom that dissipates into the environment. In this case, the jump operator $\hat{K} = |g\rangle\langle e|$ would be

releasing the photon and transitioning to the ground, and γ_l would be the decay rate. Causing decay is the normal result of an external environment interacting with some specified system. The master equation allows one to nearly fully model the interaction with very little information [41].

2.7.2 Quantum trajectory and Monte Carlo wavefunction method

One problem with the master equation is that it relies on the density matrix instead of the state. In tensor network terms, this means evolving an MPO instead of a MPS which can be incredibly cumbersome and prevents most of our techniques from being used. MPOs scale far worse than MPS states. Fortunately, there is an alternative method that allows one to directly use a state MPS instead of the density matrix MPO. The quantum trajectory method works by performing many different probabilistic paths the state's evolution can take and then combining them together to form a density matrix at the end. [41] Though often it is sufficient to just average over the observables never needing to generate the density matrix. To do this set our state $|\psi\rangle = |\psi(t_0)\rangle$ to the initial state, we will need this initial state later. We then evolve $|\psi\rangle$ with the non-Hermitian Hamiltonian as follows for a single-time step:

$$\hat{H}_{eff} = \hat{H} + \sum_l \frac{i\gamma_l}{2} \hat{K}_l^\dagger \hat{K}_l \tag{2.6}$$

After that we need to consider the possibility of a quantum jump, to do this first we need to compute the probability of each jump as follows:

$$p_l = \gamma_l \delta t | \langle\psi| \hat{K}_l \hat{K}_l |\psi\rangle | \tag{2.7}$$

To see whether a jump has occurred during δt generate a random number r between 0 and 1, and if $r \leq p_l$ then a jump has occurred. If a jump occurs update $|\psi\rangle$ by applying the jump operator $|\psi'\rangle = \hat{K}_l |\psi\rangle$, otherwise do not update $|\psi\rangle$. This will give you $|\psi(t+\delta t)\rangle$. The non-Hermitian decay part of H_{eff} might seem surprising because the decay affects the state even when a jump does not occur, however, this is expected because not detecting a photon is a measurement in itself. Repeat the H_{eff} evolution and jump time steps until reaching the desired end time. This will give you a single quantum trajectory, or one possible path that the state could've taken in its evolution. To properly model the dissipation many paths must be computed with the same process, making sure to always start with the same $|\psi(t_0)\rangle$. If one performs n trajectories then the density matrix can be written as $\rho(t) = \sum_i \frac{1}{n} |\psi_i(t)\rangle \langle\psi_i(t)|$. [41] Alternatively one can compute the observables

they wish along the path to get and average over them instead, this is often the more efficient method.

2.7.3 Vectorized density matrix

The problem with the trajectory method is that it's not obvious how many trajectories are required to properly model the system. Often times it can become intractable to perform the computation such a large number of times. This is especially true if you're only interested in the steady state as it could also require a very large t_f for your system to settle down. There does exist another method [38] that allows one to evolve ρ as if it were a MPS that allows us to use these advantages. To start map ρ to a vector $|\rho\rangle\rangle$, in general ρ can be written as $\rho = \sum_{\sigma,\sigma'} c_{\sigma,\sigma'} |\sigma\rangle \langle\sigma'|$ where $|\sigma\rangle = |\sigma_1, \sigma_2, ..., \sigma_{N-1}\sigma_N\rangle$ is the multi-site basis state, and $c_{\sigma,\sigma'}$ are c-number coefficients. The mapped vectorized density matrix $|\rho\rangle\rangle$ is then:

$$|\rho\rangle\rangle = \sum_{\sigma,\sigma'} c_{\sigma,\sigma'} \, ||\sigma\rangle \langle\sigma'|\rangle\rangle \tag{2.8}$$

where we define the vectorized operator $||\sigma\rangle \langle\sigma|\rangle$ from the tensor product as follows:

$$|\rho\rangle\rangle = \sum_{\sigma,\sigma'} c_{\sigma,\sigma'} \bigotimes_{i=1}^{N} |\sigma_i\rangle\rangle \otimes \bigotimes_{i=1}^{N} |\sigma_i'\rangle\rangle \tag{2.9}$$

To evolve this $|\rho\rangle\rangle$ we map the lindbladian super operator from the master equation to a normal MPO operator acting on the vectorized density, as in $\dot{\rho} = \mathcal{L} \, |\rho\rangle\rangle$. Taking advantage that in our basis that $|X\rho Y\rangle\rangle = Y^T \otimes X \, |\rho\rangle\rangle$, we can that the master equation super operator becomes:

$$\mathcal{L}(\rho) \to \mathcal{L} \, |\rho\rangle\rangle \tag{2.10}$$

$$\mathcal{L} = -i(I \otimes H - H^T \otimes I) + \sum_l \frac{1}{2} \left[2\hat{K}_l^* \otimes \hat{K}_l - I \otimes K_l^\dagger K_l - K_l^T K_l \otimes I \right] \tag{2.11}$$

where K_l^* is the complex conjugate and $K_l^\dagger$ is the hermitian conjugate and K_l^T is the transpose. In this case, the dissipation rate is included in the jump operator itself so we redefine $K_l = \sqrt{\gamma_l} K_l$. In converting ρ of N sites to a vectorized density we create a MPS with 2N sites. This is generally still favourable over evolving the density matrix MPO as we can use all our efficient algorithms for the MPS.

Another caveat is whether one expects the steady state to be heavily mixed or close to a pure state. If it is close to a pure state then the sites should be ordered above

as $A^{\sigma_1}A^{\sigma_2}...A^{\sigma_N}A^{\sigma'_1}...A^{\sigma_{N'}}$ or what I'll call the "long" pattern. This is because $\rho = |\psi\rangle\langle\psi|$ is just a simple tensor product with no correlation, however, in the case of heavily mixed states such as the identity it is better to order the sites such that your MPS goes $A^{\sigma_1}A^{\sigma'_1}A^{\sigma_2}A^{\sigma'_2}...A^{\sigma_N}A^{\sigma'_N}$ or what I'll call the "short" pattern. This is because $|\sigma_i\rangle\langle\sigma'_i|$ can be highly correlated and with an MPS you want to minimize the amount of long-range entanglement to maximize the efficiency. This brings some complications in performing the tensor product, however, they can be solved relatively easily as shown in Fig. 2.15.

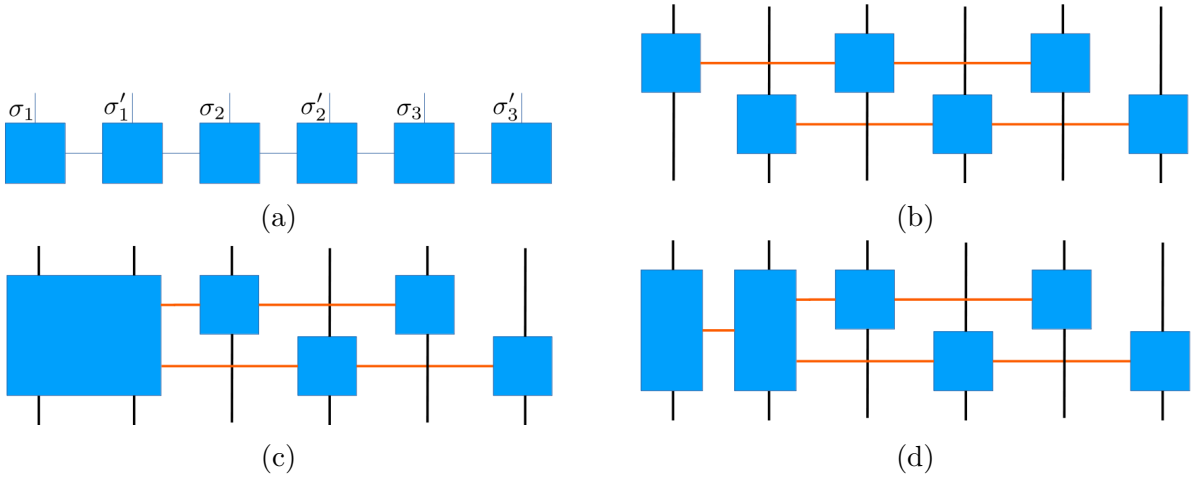

Figure 2.15: (a) The index structure of the heavily mixed scheme for the vectorized density matrix of a 3-site system. (b) The tensor network $A \otimes B$ of operators A and B, with the modified site order configuration (c) Contraction of A_1 and B_1, the first step in converting these two MPOs into a single MPO (d) Schmidt decomposition of the contraction. Repeating (c)-(d) are for all the sites returns us to the standard MPO structure. Assume in all diagrams that lines of different colours overlapping do not represent matching indexes.

One interesting property is that the steady-state satisfies $\mathcal{L}|\rho\rangle\rangle = 0$, so by finding the eigenvector of $\mathcal{L}$ with eigenvalue 0 you can directly solve for the steady state of your system. This can be calculated using an MPS in an Arnoldi DMRG scheme previously mentioned, as, unlike the Davidson method the Arnoldi can be programmed to solve for the eigenvectors with specific eigenvalues. Alternatively and from my experience far more reliable one can use the standard tried and true Davidson DMRG method to find the ground state of $\mathcal{L}^\dagger\mathcal{L}$ to get the steady state. One problem though with both of these methods is that they don't conserve the trace, even if they conserve the norm $\langle\langle\rho|\,\rho\rangle\rangle = 1$. This even occurs if you perform a TDVP evolution instead of using a DMRG. Generally, this can be handled though as you can merely take this into consideration when computing

your observables as follows [38]:

$$\langle \hat{O} \rangle = Tr(\hat{\rho}\hat{O})/Tr(\rho) = \langle\langle I| \, I \otimes \hat{O} \, |\rho\rangle\rangle \, / \, \langle\langle I|\rho\rangle\rangle \tag{2.12}$$

This equation, unfortunately, causes problems for the "long" site pattern because $\langle\langle I|$ requires $O(2^N)$ resources to represent due it being equivalent to several long-range correlations between sites i and $i' = N + i$. As a result, we've found it is generally better to never compute $\langle\langle I|$ directly. Instead compute its action as a series of MPOs that project out the non-identity overlap, and a MPS that leads to an equivalence relation.

2.8 Alternative interpretation of matrix product states

An alternative formulation of the matrix product state that gives a more physical interpretation is that of the auxiliary spin representation [32]. The auxiliary spin representation works by having each of the physical spin sites comprised of two auxiliary spins. Each auxiliary spin is entangled with one other auxiliary spin within the nearest neighbor's physical spin. A diagram of this configuration can be seen in Fig. 2.16. The state formed by these auxiliary spins is:

$$|w_D\rangle = \sum_{k=0}^{D} |k,k\rangle \tag{2.13}$$

Where D is the bond dimension of the link and the dimensionality of the auxiliary spin. For the edge auxiliary spins the state takes the form of $|w_D^{(edge)}\rangle = \sum_{k=0}^{D} |k\rangle$. It should be noted that this is assuming a non-periodic MPS, in periodic MPS like the infinite case there is no need for an edge state. The state of the MPS is actually stored not in the auxiliary spins but in the isometric mappings $\mathcal{P}_s$ that maps from the 2 auxiliary spin basis of a site s to its respective physical spin basis. Applying these mappings as a tensor product to all the physical spin sites provides the ability to construct a general state as follows:

$$|\psi\rangle = \mathcal{P}_1 \otimes \mathcal{P}_2 \otimes ... \otimes \mathcal{P}_N \, |w_D\rangle^{\otimes N} \tag{2.14}$$

where the isometric mapping can be written in a way very reminiscent of our other representation of the matrix product state as follows:

$$\mathcal{P}_s = \sum_{i,\alpha,\beta} A^{i,(s)}_{\alpha,\beta} \, |i\rangle \, \langle \alpha, \beta| \tag{2.15}$$

When we expand out $|\psi\rangle$ subbing in the equation for $\mathcal{P}_s$ the states take a form identical to the original formula that was given for the matrix product state whereas the suggestive notation implies $A^{i,(s)}_{\alpha,\beta}$ is just the MPS state's matrix for site s. What's fascinating about this representation is that despite having only local entanglement by merely applying what is effectively local isometric "projectors", we can represent a general even potentially very long-range entanglement state.

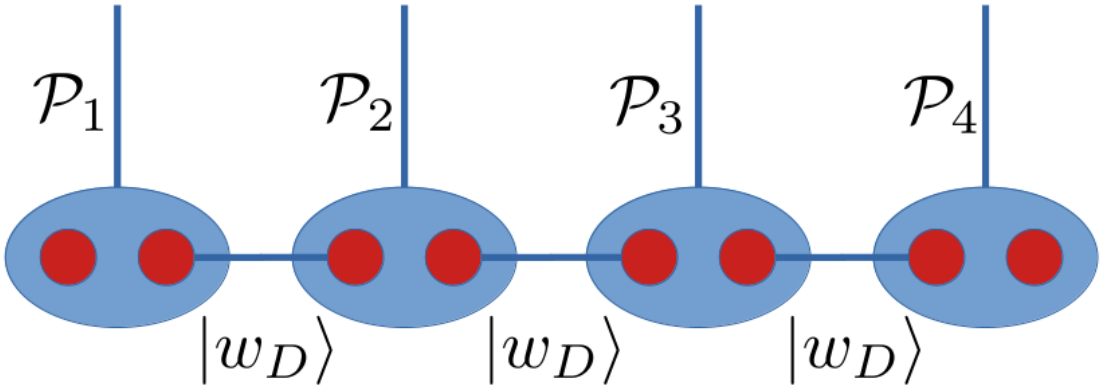

(a)

Figure 2.16: (a) Auxiliary particle matrix product state representation. Physical spin sites and auxiliary spins are represented by blue circles and red ovals respectively. The physical spins are constructed by applying the isometric map $\mathcal{P}_s$ to the two auxiliary spins within and comprising the site. Auxiliary spins are entangled by at most 1 other auxiliary spin in the nearest neighbour physical site forming the state $|w_D\rangle$, where D is the bond dimension of the link.

Chapter 3

Waveguide QED platform for synthetic quantum matter

3.1 Summary

This chapter will consist of a proposal for a waveguide cavity quantum electrodynamic (QED) toolbox for quantum simulation. It was originally presented within [1] for which I am a co-author. My contribution on the project consisted of performing the numerical work, writing technical portion of the manuscript, and coming up with the isometric mapping that was used to bring the SU(2) states to SU(N).

Tensor networks are only able to go so far when it comes to handling quantum states. There are some states that simply can not be realistically represented with tensor networks. This is especially true of highly entangled states or those in gapless systems [7, 31], which do form in nature. This leaves a large set of physical problems unsimulatable with them. Luckily, Feymann had a way around this, the quantum simulator[17]. A quantum simulator is a controlled quantum device that can be used to simulate other quantum systems of interest [6]. In short, it's simulating quantum physics using quantum physics. A simulator is not the same as a quantum computer, even though quantum computers are capable of doing quantum simulation.

In current devices, quantum simulation is done by directly modelling a Hamiltonian in an analog device as opposed to the gate-based binary approach a true quantum computer would do [17]. Analog simulators are within the capability of near-term devices, while digital quantum simulators are expected to remain elusive for the foreseeable future [6]. Quantum simulators are expected to advance a wide range of fields, from chemical dynamics to particle physics to cosmology [42].

There have been many proposals for quantum simulator platforms, including those based on trapped ions, superconducting circuits, neutral atom arrays [42] and photons [43]. All these digital quantum simulation methods have managed to be achieve 50 qubit simulators [19, 44–46]. The ability for 1000s of qubit quantum simulators seems to be realistically within reach, and this is already beyond the ability of direct exact diagonalization methods[42]. Analog quantum simulators, archetypically, are limited to physics similar to the quantum platform they are run on. However, that is not necessarily true, an alternative scheme is the new paradigm of universal analog quantum simulation, which we explore in this chapter. In this chapter, a proposal for a neutral atom array model that makes use of a waveguide and cavity QED to perform universal analog quantum simulation is presented.

The platform directly allows general construction and thus simulation of SU(2) 2-body Hamiltonians. 2-body Hamiltonians are those of the form $H = \sum_{i,j} \hat{h}_{i,j}$, where $h_{i,j}$ is an operator that acts only on sites i and j. Hamiltonians of this form have been shown capable of performing universal quantum computation [47–49]. The use case is far outside of our current capabilities, but what we propose instead is using the platform to perform analog synthetic quantum matter simulation.

A standard use case consists of: Preparing some initial state, doing the respective time evolution, and then measuring whatever observables are relevant [6]. Alternatively, one can adiabatically evolve the Hamiltonian to transfer a trivial ground state (e.g., paramagnet state) to the ground state of some computationally relevant Hamiltonian [47]. The toolbox utilizes coupling of spin-matter to atomic motion generated by "spin-independent" forces of the synthetic vacuum of the PCWs (Photonic Crystal Waveguide) to mediate the underlying long-range spin-spin interactions.

In more detail, we have spin matter with spin states $|g\rangle$ $|s\rangle$ and a collective vibrational motion called the phononic Bogliobov modes. The Bogliobov modes, along with site-dependent Zeeman shifts and several site-independent programmable Raman fields, are combined to couple the spin to the bogliobov modes in such a way that one can eliminate the bogliobov modes and create an arbitrary two-site spin interaction Hamiltonian. At first glance, the platform appears to support only direct SU(2) simulation. However, this can be expanded to all SU(N) models by leveraging its universality.

To achieve this, we group the sites into blocks of N sites. In each block, it is energetically favorable for exactly 1 site to be excited within them at a time. This works similarly to Rydberg blockade, where an energy constraint enforces only 1 atom within a region to be excited [1, 27]. By having a sufficiently large energy cost for any other number of excitations, we can restrict the system to a low-energy subspace separated by a large energy gap. The energy constraint works to form an effective gauge constraint, enabling us

to construct general SU(N) 2-spin local Hamiltonians. The functionality of the toolbox will be verified through the use of tensor network simulations comparing computations directly with a Wess-Zumino-Witten (WZW) model and the emergent WZW model arising from an isometric map of the low energy subspace of the SU(2) system. In particular, these two will be computed through a combination of MPS imaginary time evolution and DMRG. Furthermore, the process to convert these multi-site SU(2) gauge constrained states to SU(N) states using a tensor network isometric mapping will be detailed. Finally, some difficult numerical example use cases will be discussed for the toolbox arising from the strong coupling WZW model.

The novelty of this toolbox is as follows:

- This is the first experimental proposal for realizing general universal 2-body Hamiltonians with a fully analog quantum simulator.
- We provide the first method of designing an effective gauge constraint that encodes sets of N SU(2) atoms to SU(N) spins. We then use this to achieve arbitrary pairwise interactions between the SU(N) spins.
- We provide the ability a method to manipulate anyons and perform open quantum system simulation with a waveguide QED architecture.

3.2 Introduction

An exciting frontier in quantum information science is the realization and control of complex quantum many-body systems. Hybrid nanophotonic system with cold atoms has emerged as the paradigmatic platform for realizing long-range spin models from the bottom up, exploiting their modal geometry and group dispersion for tailored interactions. An important challenge is the physical limitation imposed by the photonic bath, constraining the types of local Hamiltonians that decompose the available physical models and restricting the spatial dimensions to that of the dielectric media. However, at the nanoscopic scale, atom-field interaction inherently accompanies significant driven-dissipative quantum forces that may be tamed as a new form of a mediator for controlling the atomic internal states. In this chapter, we formulate a quantum optics toolbox for constructing a universal quantum matter with individual atoms in the vicinity of 1D photonic crystal waveguides. The enabling platform synthesizes analog quantum materials of universal 2-local Hamiltonian graphs mediated by phononic superfluids of the trapped atoms. We generalize our microscopic theory of analog universal quantum simulator to the development of dynamical gauge fields. In the spirit of gauge theories, we investigate emergent lattice models of

arbitrary graphs, for which strongly-coupled SU(n)-excitations are driven by an underlying multi-body interaction. As a minimal model in the infrared, we explore the realization of an archetypical strong coupling quantum field theory, SU(n) Wess-Zumino-Witten model, and discuss a diagnostic tool to map the conformal data of the field theory to the static and dynamical correlators of the fluctuating photons in the guided mode.

One of the central problems in quantum information science and condensed matter physics is to create and control strongly interacting quantum systems, and to measure the equilibrium and non-equilibrium properties of the many-body system [17, 50, 51]. Recent experiments with ultracold atoms have extended the ranges of unconventional phenomena that may be accessed. A common thread to these efforts is the quest to design the Hamiltonian by harnessing the natural interactions available between cold atoms [52]. Much of the focus has largely been on analog and Floquet quantum systems. However, these approaches are limited in their applicability to complex target Hamiltonians whose description departs significantly from the microscopic model of the simulator.

A parallel development has been the exploration of computational complexity of local Hamiltonians, whose ground state properties cannot be efficiently obtained even by a digital quantum computer. An example of such a Quantum-Merlin-Arthur (QMA) problem is to find the ground state of 2-local Hamiltonians $\hat{H}_{\rm QMA} = \sum_{ij} \hat{h}_{ij}$, where the local decomposition $\hat{h}_{ij}$ consists of at most 2-body SU(2) operators. More generally, arbitrarily complex quantum matter $\hat{H}_{\rm target}$ can be emulated with a seemingly simpler but QMA-complete lattice model $\hat{H}_{\rm QMA}$ [53], in that all physical properties and local structures of $\hat{H}_{\rm target}$ can be efficiently mapped onto the universal model $\hat{H}_{\rm QMA}$. Likewise, a quantum simulator that realizes analogue Hamiltonians $\hat{H}_{\rm QMA}$ can be adapted for universal quantum computation in the spirits of cellular automata and Hamiltonian computation [47–49].

With recent developments in atom-photon interfaces with photonic crystals [54–64], there has been significant interest towards assembling quantum many-body systems by garnering the control over individual quantum systems [17, 50–52]. With the atomic transition frequency residing within the photonic band gap (PBG), the underlying lattice of atoms cannot dissipate propagating waves into the guided modes (GMs) of the photonic structure. However, the mere presence of the atoms at sites i, j in a waveguide seeds dynamic defect modes that support stable atom-field bound states in the form of evanescent waves [54, 55, 65–67], mediating exchange interaction $J_{|i-j|}\vec{\hat{\sigma}}^{(i)} \cdot \vec{\hat{\sigma}}^{(j)}$ between the trapped atoms [68, 69]. With auxiliary Raman sidebands and digital time-steps [17], the phase-amplitude function $J_{|i-j|}$ can be engineered for atoms coupled to 1D and 2D photonic crystal waveguides (PCW), and realize translationally-invariant pairwise models for quantum magnetism, constrained by the dimension of the dielectric [70]. Conversely, photons propagating through the guided mode exhibit novel quantum transport and many-body

phenomena [71–75].

At the nanoscale, atom-field interaction is modified by the electromagnetic vacuum of the "dielectric," consisting of both the passive photonic structure and the active emitters. Such a quantum dielectric is inherently renormalized by the strong coherent and dissipative radiative forces between the atoms. Indeed, complex spin-mechanical textures arise through localized spin-dependent photon-mediated forces [76]. More generally, nanoscopic quantum forces modify the mechanical "vacuum" of the atomic motion, where Bogoliubov phonons are distributed across the atomic sample as a collective bath that in turn couples to the spin system. Dissipative nature of these forces in PCW may be exploited to stabilize and self-organize new forms of mechanical phases of quantum matter, and complex observables may be constructed for the detection of highly entangled quantum systems.

Here, we harness the coherent coupling between atomic motion and internal states in 1D PCW for the realization of an analogue universal quantum matter. We develop a low-energy theory for the quantum motion of the trapped atoms in the bandgap regime of waveguide quantum electrodynamics (QED). By coupling Bogoliubov phonons to the spin matter, we realize a fully programmable lattice spin system $\hat{\rho}_s$ for neutral atoms. In our approach, arbitrary binary interaction $\hat{h}_{ij} \simeq \sum_{\alpha,\beta} J_{\alpha\beta}^{(i,j)} \hat{\sigma}_\alpha^{(i)} \hat{\sigma}_\beta^{(j)}$ is realized for any combination of SU(2)-spin operators $\hat{\sigma}_\alpha^{(i)}, \hat{\sigma}_\beta^{(j)}$ with $\alpha, \beta \in \{0, x, y, z\}$ between sites i and j. Our spin-network $\hat{\rho}_s$ are described by Hamiltonian graphs with connectivity i, j that can no longer be represented by spatial lattices and dimensions, and realizes the universal 2-local quantum matter $\hat{H}_{\mathrm{QMA}} = \sum_{i,j} \hat{h}_{ij}$ in a fully analog manner. Our waveguide QED simulator, stabilizing $\hat{H}_{\mathrm{QMA}}$, is universal, in that any k-local Hamiltonian $\hat{H}_{\mathrm{target}}$ of arbitrary connectivity can be embedded into the low-energy sector of $\hat{H}_{\mathrm{QMA}}$ [53]. This notion of universality is strong in that any physical phenomena of $\hat{H}_{\mathrm{target}}$ must correspond to an "emergent" behavior of the analogue simulator $\hat{H}_{\mathrm{QMA}}$ in the long-distance limit.

Moreover, we formulate a hardware-efficient protocol to design dynamical gauge structures of many-body system and realize a plethora of SU(n) models with our waveguide QED simulator. Motivated by gauge fixing in quantum spin glasses and color codes, we describe a general construction for which the low energy physics of $\hat{\rho}_s$ encompasses the full scope of binary lattice models for SU(n)-spin excitations with local constraints that protect the many-body wave function $\hat{\rho}_s$ from errors. Here, atomic arrays constrained by their local symmetries are encoded into logical SU(n)-blocks, and dynamical U(1)-gauge fields mediate programmable long-range interactions between the logical blocks.

Utilizing these capabilities, we demonstrate the versatility of our universal analog simulator by constructing chiral spin liquids [21] and holographic strange metals [77, 78]. As a primordial example to the tower of phases, we explore the physics of SU(3) Wess-Zumino-

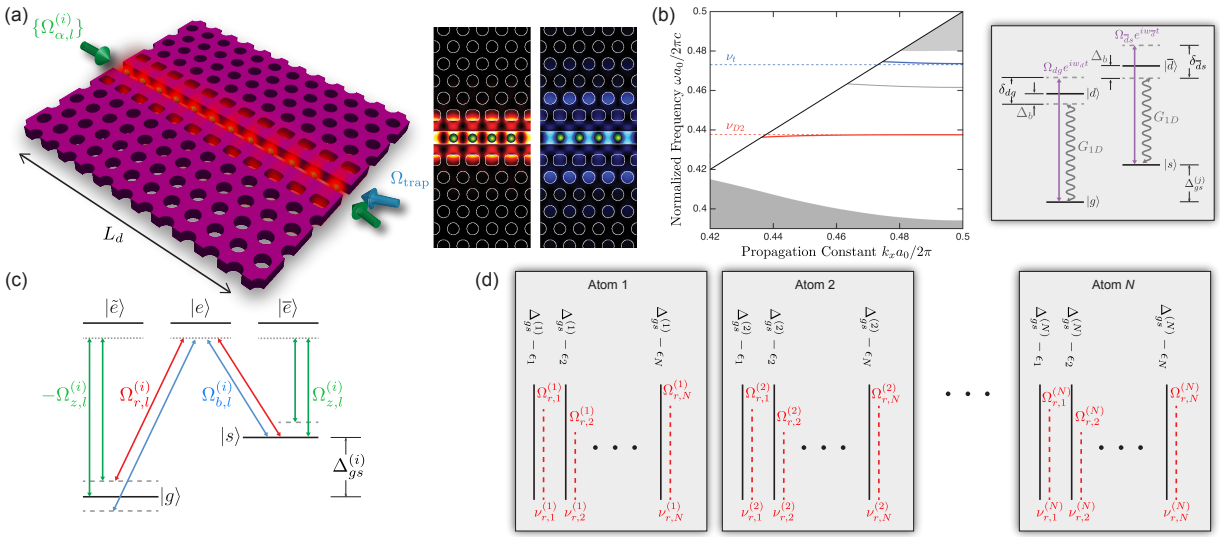

Figure 3.1: Complex quantum many-body physics with waveguide QED systems. (a) Exemplary waveguide QED spin network. Slotted squircle photonic crystal waveguide (SPCW) enables a versatile platform for highly tunable defect guided modes, with the supermodes shown in the inset. As a candidate PCW, structural parameters are provided in the Table 3.1 and discussed in 3.9. Green spheres represent the trapped atoms. Inset. Contour map of the intensity profile for TE supermodes for exciting (trapping) Cs atoms at wavelengths $\lambda_p = 852$ nm ($\lambda_t = 794$ nm). (b) Normalized band diagram for the supermodes of SPCW. Inset. Two lasers $\Omega_{dg}, \Omega_{\bar{d}s}$ with detunings $\delta_{dg}, \delta_{\bar{d}s}$ create strong photonic Lamb shifts $\sim e^{-|i-j|a_0/L_c}$ between two atoms localized within a photonic bandgap [65]. The bandgap is detuned by Δ_b with respect to the transition frequency. (c) Raman couplings synthesize programmable interactions between two atoms at sites $i, j \in \{1 \cdots N\}$ for any combination of SU(2) spin operators. Site-resolved addressing with spatially global fields $\Omega^{(i)}_{\alpha,l}$ (in the frequency domain) is achieved through inhomogeneous Zeeman shifts $\Delta^{(i)}_{gs}$ through intermediated excited states $|\tilde{e}\rangle, |e\rangle, |\bar{e}\rangle$ with $\alpha \in \{r, b, z\}$. (d) Raman engineering. Programmable Raman fields $\Omega^{(i)}_{\alpha,l}$ selectively couples internal states $|g\rangle, |s\rangle$ of atom i to the Bogoliubov phononic mode $l \in \{1, \cdots, N\}$ with two-photon detuning $\nu^{(i)}_l$. Each single sideband mode with frequency $\nu^{(i)}_l$ (red dash line) is nearly resonant to $\Delta^{(i)}_{gs} - \epsilon_l$ (black solid line), where ϵ_l is the phonon spectrum. Only the red sideband couplings are depicted for simplicity.

Witten conformal field theory (CFT), a holographic dual to a Chern-Simons gravity [79], by encoding the target CFT onto the low-energy sector of our waveguide QED simulator. We investigate the critical scaling of CFT entanglement and the dynamics of semionic quasiparticle excitations, as reflected by the fluctuating photons of the PCW. Our networked approach provides powerful tools for controlling analog quantum systems with complexities far beyond of regular spin lattices heretofore explored.

The structure of this chapter is organized as follows. In Section 3.3, we investigate the interplay among waveguide photons, atomic external motion and internal energy levels, and establish the low-energy theory for an analogue quantum simulator of universal Hamiltonians [53]. In Section 3.4, we discuss the realization of a chiral spin liquid on Kagome lattice and the detailed design of Raman sidebands. In Section 3.5, we introduce the realization of SU(N) spin models by gauging N two-level atoms to a constrained subspace. With this logical encoding, we construct a general SU(n) Hamiltonian for the waveguide QED platform. In Section 3.6, we analyze the emergence of a minimal SU(3) Wess-Zumino-Witten model with matrix product states and discuss operational metrics for its diagnosis. In Section 3.7, we discuss the experimental feasibility and summarize the advances made in this work.

3.3 Platform

3.3.1 Lamb shifts in PCW: Phononic Hubbard model

Our approach is based upon the unique capability of PCWs to induce strong photon-mediated forces between proximal neutral atoms and to create many-body states of internal spin and external motion. By engineering the QED vacuum of the PCW, we synthesize coherent mechanical coupling between the trapped atoms, and renormalize the atomic array into a mechanical quantum network. Long-range interaction of the universal Hamiltonian $\hat{H}_{\rm QMA} = \sum_{i,j} \hat{h}_{i,j}$ is mediated through the phononic quantum channels with full control over the decompositions $\hat{h}_{i,j}$ and their connectivity i, j.

As shown in Fig. 3.1, our basic building block is an 1D lattice of neutral atoms at positions x_i strongly coupled to a dispersive PCW with mode function $u_{k_0}(x)$ represented by the red line of Fig. 3.1(b). The band edge at frequency w_b is red-detuned by $\Delta_b = \omega - \omega_b > 0$, so that the atomic transition frequency ω lies within the band gap. Each atom is tightly localized at the antinodes of $u_{k_0}(x)$ with trap frequency ω_t and lattice constant a_0 by a nanoscopic optical potential $V_{\rm T} = V_0 \sin^2 k_0 x$ with a trapping field at a higher-order GM (blue line). In 3.9, we analyze a versatile candidate structure (Silicon Nitride Squircle

PCW) with highly tunable GMs in terms of TE photonic band gap, effective photon mass m_e and mode area A_{eff} near the band edge $k_x = k_0$ (See Fig. 3.1(b) for the band diagram). $|g\rangle$ and $|s\rangle$ are the two hyperfine ground states that define the computational basis $\mathcal{C}$ of the waveguide QED simulator, and the ground states respectively couple to excited states $|d\rangle$ and $|\bar{d}\rangle$, which will be eliminated to induce a pure mechanical coupling between the atoms.

The atom-PCW Hamiltonian reads $\hat{H}_{\text{PCW}} = \int d\boldsymbol{x} \int_0^\infty d\omega \hat{\boldsymbol{f}}^\dagger(\boldsymbol{x},\omega)\hat{\boldsymbol{f}}(\boldsymbol{x},\omega) + \sum_i(\omega_d \sigma_{dd}^{(i)} + \omega_{\bar{d}}\sigma_{\bar{d}\bar{d}}^{(i)} + \Delta_{gs}\sigma_{ss}^{(i)}) + \sum_{i=1}^{N_a}\sum_{\mu=dg,\bar{d}s}[\int_0^\infty d\omega \boldsymbol{E}(\boldsymbol{x}_i,\omega)\cdot\boldsymbol{d}_\mu\hat{\sigma}_\mu^{(i)} + \Omega_\mu\sigma_\mu^{(i)}e^{-i\nu_\mu t}]$, where $\boldsymbol{d}_{dg(\bar{d}s)}$ is the transition dipole momentum from $|g(s)\rangle$ to $|d(\bar{d})\rangle$ and $\Omega_{dg(\bar{d}s)}$ is the Rabi frequency of the pumping fields with frequency $\nu_{dg(\bar{d}s)}$ that couples $|g(s)\rangle$ and $|d(\bar{d})\rangle$. We assume $\boldsymbol{d}_{dg} = \boldsymbol{d}_{\bar{d}s} = \boldsymbol{d}$. The electric field in the PCW can be represented by classical Green's function $\boldsymbol{G}(\boldsymbol{x},\boldsymbol{x}',\omega)$ as $\hat{\boldsymbol{E}}(\boldsymbol{x},\omega) = i\mu_0\omega^2\sqrt{\frac{\epsilon_0}{\pi}}\int d\boldsymbol{x}'\sqrt{\text{Im}\{\epsilon(\boldsymbol{x}',\omega)\}}\boldsymbol{G}(\boldsymbol{x},\boldsymbol{x}',\omega)\hat{\boldsymbol{f}}(\boldsymbol{x},\omega)$, where $\hat{\boldsymbol{f}}(\boldsymbol{x},\omega)$ represents the quantized excitation of the dielectric with permittivity $\epsilon(\boldsymbol{x}',\omega)$ [80].

In the limit $f_{dg(\bar{d}s)} = \Omega_{dg(\bar{d}s)}/\delta_{dg(\bar{d}s)} = f \ll 1$ where $\delta_{dg(\bar{d}s)} = \nu_{dg(\bar{d}s)} - \omega_{d(\bar{d})}$, we adiabatically eliminate the excited states $|d\rangle$ and $|\bar{d}\rangle$ from the system and integrate out the photonic modes [81–84]. We thereby obtain the low-energy Liouvillian dynamics $\dot{\hat{\rho}} = -i[\hat{H}_M^{\text{int}},\hat{\rho}] + \mathcal{L}_0[\hat{\rho}] + \mathcal{L}_M[\hat{\rho}]$ with a purely mechanical Hamiltonian

$$\hat{H}_M^{\text{int}} = f^2\Delta_{\text{Lamb}}(\hat{\boldsymbol{x}}_i,\hat{\boldsymbol{x}}_j)\hat{\sigma}_0^{(i)}\hat{\sigma}_0^{(j)} \tag{3.1}$$

and the respective Lindblad superoperators $\mathcal{L}_0[\hat{\rho}] = \sum_{i,j}\frac{\Gamma_{ij}f^2}{2}(2\hat{\sigma}_0^{(i)}\hat{\rho}\hat{\sigma}_0^{(j)} - \hat{\sigma}_0^{(i)}\hat{\sigma}_0^{(j)}\hat{\rho} - \hat{\rho}\hat{\sigma}_0^{(i)}\hat{\sigma}_0^{(j)})$ and $\mathcal{L}_M[\hat{\rho}] = \sum_{i,j}\frac{\Gamma_{ij}f^2}{2}(2e^{ik\hat{\boldsymbol{x}}_i}\hat{\rho}e^{-ik\hat{\boldsymbol{x}}_j} - e^{ik(\hat{\boldsymbol{x}}_i-\hat{\boldsymbol{x}}_j)}\hat{\rho} - \hat{\rho}e^{ik(\hat{\boldsymbol{x}}_j-\hat{\boldsymbol{x}}_i)})$ acting on the internal and external degrees of freedom (DOF), where $\hat{\sigma}_0 = |g\rangle\langle g| + |s\rangle\langle s|$ is the identity spin operator in $\mathcal{C}$. Photonic Lamb shift and correlated dissipation, modified by the PCW, are given by

$$\Delta_{\text{Lamb}}(\hat{\boldsymbol{x}}_i,\hat{\boldsymbol{x}}_j) = 2\mu_0\omega_b^2\boldsymbol{d}^*\cdot\text{Re}[\boldsymbol{G}_s(\hat{\boldsymbol{x}}_i,\hat{\boldsymbol{x}}_j,\omega_b)]\cdot\boldsymbol{d} \tag{3.2}$$

$$\Gamma_{ij}(\hat{\boldsymbol{x}}_i,\hat{\boldsymbol{x}}_j) = \mu_0\omega_b^2\boldsymbol{d}^*\cdot\text{Im}[\boldsymbol{G}(\hat{\boldsymbol{x}}_i,\hat{\boldsymbol{x}}_j,\omega_b)]\cdot\boldsymbol{d}, \tag{3.3}$$

where $\boldsymbol{G}_s = \boldsymbol{G} - \boldsymbol{G}_0$ is the scattering Green's function relative to the vacuum term $\boldsymbol{G}_0$ (See 3.9). Importantly, coherent dynamics of Eq. 3.1 is decoupled from the internal states within the computational space $\mathcal{C}$, and only induce non-local mechanical interaction between the trapped atoms. The state-independence of Eq. 3.1 is crucial, as the photon-mediated spin-exchange coupling cannot break the translational invariance intrinsic to the photonic crystal structure [65]. Instead, our quantum simulator emerges from the programmable interactions between the internal states and the Bogoliubov modes of Eq. 3.1. Indeed, seen from the atoms, the correlated radiative decay Γ_{ij} does not directly contribute to

the dynamics of computational subspace $\mathcal{C}$ but induces mechanical damping to the atomic quantum motion.

In our case, the GM near the band edge $k_x = k_0$ (corresponding frequency ω_b) exhibits an extremely flat band $w_k - w_b \simeq -\frac{1}{2m_e}(k_x - k_0)^2$ and the GM photons acquire large mass $1/m_e = -(\partial^2 w_k/\partial k_x^2)$ (See Fig. 3.1(b) for the first Brillouin zone). In the reactive regime of the PBG, the atoms predominantly couple to this band edge and the Green's function is approximated by

$$G_{1\mathrm{D}}(\hat{x}_i, \hat{x}_j) = J_{1D} u_{k_0}(x_i) u_{k_0}(x_j) e^{-|\hat{x}_i - \hat{x}_j|/L_c}, \tag{3.4}$$

where the localization length $L_c = \sqrt{1/2m_e\Delta_e} \sim a_0$ is controlled by the detuning $\Delta_e \simeq 2\Delta_b$ of the pumping field from band edge. $J_{1\mathrm{D}} = -\frac{c^2}{2\omega_b L_c A_{\mathrm{eff}}} \frac{1}{\Delta_e + i\kappa/2}$ is the coupling rate to the PCW with effective mode area $A_{\mathrm{eff}} \simeq \lambda^2$, mode function $u_{k_0}(x_i)$ at the band edge, and decay rate κ (κ_0) in the band gap (at the band edge). The correlated Lamb shift thereby provides the tunnelling interaction $\hat{H}_M = f^2 \Delta_{1\mathrm{D}} e^{-|\hat{x}_i - \hat{x}_j|/L_c}$ between local phonons pinned on the lattice sites x_i and x_j, with $\Delta_{1\mathrm{D}} = \frac{\omega_b d^2 \Delta_e}{\epsilon_0 L_c A_{\mathrm{eff}}(\Delta_e^2 + \kappa^2/4)}$. Importantly, the collective damping $\Gamma_{1\mathrm{D}} \sim \tilde{\Gamma}_{1\mathrm{D}} \exp(-L_d/L_c)$ is exponentially inhibited for a finite device length L_d, with $\tilde{\Gamma}_{1\mathrm{D}} = \frac{\omega_b d^2 \kappa_0}{2\epsilon_0 L_c A_{\mathrm{eff}}(\Delta_e^2 + \kappa_0^2/4)}$, and figure of merit $\mathcal{F} = \Delta_{1\mathrm{D}}/\Gamma_{1\mathrm{D}} \sim \exp(L_d/L_c) \gg 1$ is favorable for massive photons with flat bands and long device length $L_d \gg L_c$.

To make progress analytically, we consider the case of $L_c \sim a_0$ with massive photons (flat bands in the PCW), where the atom-atom interaction reduces to nearest-neighbouring terms. We thereby expand the mechanical Hamiltonian $\hat{H}_M$ around the equilibrium positions to the second order of the zero-point motion $x_0 = \sqrt{\hbar/2m\omega_t}$ and obtain the quadratic form

$$H_{\mathrm{M}} = \sum_i \frac{\hat{p}_i^2}{2m} + \frac{m\omega_t^2}{2}\hat{x}_i^2 - \frac{\hbar g_{\mathrm{m}}}{L_c^2}\hat{x}_i\hat{x}_{i+1} + \mathcal{O}(\hat{x}_i^4), \tag{3.5}$$

for the mechanical coupling constant $g_{\mathrm{m}} = f^2\Delta_{\mathrm{Lamb}}$ and the trap frequency ω_t. With a first-type sine transform $B_{jk} = \frac{1}{\sqrt{N}} \sin[i\frac{\pi}{N+1}jk]$, we diagonalize $H_{\mathrm{M}} = \sum_{l=1}^{N} \epsilon_l \hat{\beta}_l^\dagger \hat{\beta}_l$, whose quasiparticles are the Bogoliubov phonons $\{\hat{\beta}_l\}$ with spectrum $\epsilon_l = \sqrt{\omega_t^2 + \frac{2\hbar g_{\mathrm{m}} x_0^2}{L_c^2}\cos(\frac{\pi}{N+1}l)}$ with momentum-space mode indices l. For nanoscopic optical potentials with $k_x x_0 \ll 1$, Eq. 3.5 describes a 1D Bose-Hubbard model for atomic motion with on-site (long-range) interaction $\sim \hat{x}_i^4/x_0^4$ ($|\hat{x}_i - \hat{x}_j|^4/L_c^4$), where the Bogoliubov phonons are excited out of the superfluid vacuum. The radiative damping Γ_{1D} gives rise to motional decoherence $\mathcal{L}_M[\hat{\rho}_{\mathrm{MA}}] = \sum_l \frac{\gamma_m}{2}\left(2\hat{\tilde{x}}_l\hat{\rho}_{\mathrm{MA}}\hat{\tilde{x}}_l - \{\hat{\tilde{x}}_l^2, \hat{\rho}_{\mathrm{MA}}\}\right)$ with damping $\gamma_m = \frac{g_m x_0^2}{\Delta_e L_c^2}\kappa e^{-L_d/L_c}$ and quadrature $\hat{\tilde{x}}_l = \hat{\beta}_l + \hat{\beta}_l^\dagger$. We note that the requirement for $L_c \sim a_0$ is not intrinsic to the protocol, as long-range interaction $L_c > a_0$ only modifies the frequencies of the phononic bands. The momentum-space Bogoliubov modes constitute the frequency-selective channels of an

all-to-all connected mechanical quantum network and coherently mediate the interactions between the atomic nodes, transforming the atomic array into a universal quantum matter.

3.3.2 Networked universal quantum matter

To mediate the universal lattice model via the phononic channels, we gain independent control over the interaction coefficients between any atom pair i, j by way of Raman engineering in the sideband-resolved limit. This is ensured in the reactive regime of PCW, because the mechanical damping constant γ_m is exponentially suppressed by $\mathcal{F} \sim \exp(L_d/L_c) \gg 1$ relative to the phonon spread. As shown in Fig. 3.1(c), we distinguish the coupling of an individual atom i to a particular Bogoliubov mode l with site-dependent ground-state energy shift $\hat{H}_A = \sum_i \Delta_{gs}^{(i)} \hat{\sigma}_z^{(i)}$ with $\Delta_{gs}^{(i)} = \Delta_{gs} + g_F m_F B(x_i)$ in the form of a linear Zeeman gradient $B(x_i)$ [70]. The ground-state shift $\delta\Delta_{gs}$ between neighboring sites is larger than the width of the phonon spectrum $|\epsilon_N - \epsilon_1|$, so that the frequency difference $\Delta_{gs}^{(i)} - \epsilon_l$ is different for all pairs of (i, l) (See Fig. 3.1(d)).

Then, we introduce spatially global Raman interaction $\hat{H} = \hat{H}_M + \hat{H}_A + \sum_{i,j} \sum_{\alpha,l} \frac{\Omega_{\alpha,l}^{(j)}}{2} \hat{\sigma}_\alpha^{(i)} \sin(k_{\alpha,l}^{(j)} \hat{x}_i) e^{-i\nu_{\alpha,l}^{(j)} t} + h.c$ [85–88] with N^2 frequency sidebands to the atom chain through the GM, where $k_{\alpha,l}^{(i)} \simeq k$ and $\nu_{\alpha,l}^{(i)}$ denote the wavenumber and frequency for the Raman fields that couple the spin operator $\hat{\sigma}_\alpha^{(i)}$ of atom i with $\alpha \in \{\pm, z\}$ to the Bogoliubov mode l with $\alpha \in \{\pm, z\}$. By expanding $\sin(k\hat{x}_i) \simeq \sum_l \eta_0 B_{il} (\hat{\beta}_l^\dagger + \hat{\beta}_l)$ in the Lamb-Dicke limit with $\eta_0 = x_0/a_0$ and switching to the interaction picture, we find $\hat{H}_{\mathrm{MA}} = \sum_{\alpha,i,j,l} \Omega_{\alpha,l}^{(j)} \hat{\sigma}_\alpha^{(i)} e^{-i(\nu_{\alpha,l}^{(j)} - \zeta_\alpha \Delta_{gs}^{(i)})t} \eta_0 B_{il} \hat{\beta}_l^\dagger e^{i\epsilon_l t} + h.c$, with $\zeta_\alpha = \pm 1, 0$ for $\alpha = \pm, z$. As $\Delta_{\alpha,l}^{(i)} = \nu_{\alpha,l}^{(i)} - \zeta_\alpha \Delta_{gs}^{(i)} + \epsilon_l \ll |\epsilon_l - \epsilon_{l-1}| \ll \delta\Delta_{gs}$, we integrate over the rapidly oscillating terms and leave only the slowly-varying terms $\sim \exp[i(\nu_{\alpha,l}^{(i)} - \zeta_\alpha \omega_A^{(i)} + \omega_l)t]$ and obtain the spin-mechanical Hamiltonian $\hat{H}_{\mathrm{MA}} = \sum_{i,l} \sum_{\alpha \in \{x,y,z\}} \frac{\eta_0 \Omega_{\alpha,l}^{(i)}}{2} B_{il} \hat{\sigma}_\alpha^{(i)} \hat{\beta}_l e^{-i\Delta_l t} + h.c$, thereby coupling the spin operator $\hat{\sigma}_\alpha^{(i)}$ at site x_i to a particular Bogoliubov mode l. Here, the detuning $\Delta_{\alpha,l}^{(i)} = \Delta_M$ is chosen to be identical for all phononic mode l, atom i and spin operator type α, and the Rabi frequencies are transformed as $\Omega_{x,l}^{(i)} = (\Omega_{+,l}^{(i)} + \Omega_{-,l}^{(i)})/2$ and $\Omega_{y,l}^{(i)} = i(\Omega_{+,l}^{(i)} - \Omega_{-,l}^{(i)})/2$.

By projecting the master equation to the computational subspace $\mathcal{C}$ [89], we obtain the open-system dynamics $\dot{\hat{\rho}}_A = -i[\hat{H}_{\mathrm{QMA}}, \hat{\rho}_A] + \sum_\alpha \mathcal{L}[\hat{\rho}_A]$ for the spin system, governed by the universal Hamiltonian

$$\hat{H}_{\mathrm{QMA}} \simeq \sum_{i,j,\alpha,\beta} J_{\alpha,\beta}^{(i,j)} \hat{\sigma}_\alpha^{(i)} \hat{\sigma}_\beta^{(j)} + \sum_{i,\gamma} h_\gamma^{(i)} \hat{\sigma}_\gamma^{(i)}, \tag{3.6}$$

and the correlated dissipation

$$\mathcal{L}[\hat{\rho}_A] = \sum_{i,j,\alpha,\beta} \frac{\gamma_{\alpha,\beta}^{(i,j)}}{2} \left(2\hat{\sigma}_\beta^{(i)} \hat{\rho}_A \hat{\sigma}_\alpha^{(j)} - \{ \hat{\sigma}_\alpha^{(i)} \hat{\sigma}_\beta^{(j)}, \hat{\rho}_A \} \right) \tag{3.7}$$

for any combination of $\alpha, \beta, \gamma \in \{x, y, z\}$ and between any two spins at sites i, j. Importantly, the exchange interaction $J_{\alpha,\beta}^{(i,j)}$ and the bias field $h_\gamma^{(i)}$ can be arbitrarily designed by solving a set of nonlinear equations $J_{\alpha,\beta}^{(i,j)} = 2\mathrm{Re}[\sum_l \tilde{\Omega}_{\alpha,l}^{(i)} \tilde{\Omega}_{\beta,l}^{(j)*} / \Delta_M]$ and $h_\gamma^{(i)} = -2\epsilon_{\alpha\beta\gamma}\mathrm{Im}[\sum_l \tilde{\Omega}_{\alpha,l}^{(i)} \tilde{\Omega}_{\beta,l}^{(i)*} / \Delta_M]$ where $\tilde{\Omega}_{\alpha,l}^{(i)} = \eta_0 \Omega_{\alpha,l}^{(i)} B_{il}$ and Levi-Civita symbol $\epsilon_{\alpha\beta\gamma}$. Namely, we have $6N^2$ DOFs for the sidebands $\{\Omega_{\alpha,l}^{(i)}\}$ from the nonlinear equations, while only $3(3N^2 - N)/2$ independent parameters $\{J_{\alpha,\beta}^{(i,j)}, h_\gamma^{(i)}\}$ are required to represent the universal model $\hat{H}_{\mathrm{QMA}}$. Hence, for any set $\{J_{\alpha,\beta}^{(i,j)}, h_\gamma^{(i)}\}$, at least one solution $\{\Omega_{\alpha,l}^{(i)}, \Delta_M\}$ can be obtained to the target model within certain physical constraints (e.g., laser power). We envisage that the Raman sideband matrices $\{\Omega_{\alpha,l}^{(i)}\}$ are real-time tunable. The Hamiltonian $\hat{H}_{\mathrm{QMA}}(t)$ can be evolved to map out complex phase diagrams of many-body models and be globally quenched to study out-of-equilibrium dynamics. The frequency sidebands $\{\Omega_{\alpha,l}^{(i)}\}$ can be streamed by the time-domain response function $\Omega(t)$ using a single-mode phase-amplitude modulator. Dissipative rate is evaluated as $\gamma_{\alpha,\beta}^{(i,j)} = \frac{\gamma_m}{\Delta_M} J_{\alpha,\beta}^{(i,j)} + \gamma_A \delta_{i,j}$, where δ_{ij} denotes the Kronecker symbol. Coherence-to-dissipation ratio $C = J_{\alpha\beta}/\gamma_{\alpha\beta} = \mathcal{F}/N \sim \exp(L_d/L_c)/N \gg 1$ of our simulator improves exponentially in the reactive regime. In practice, C is constrained by γ_A due to the finite $\Omega_{\alpha,l}$ and Δ_M of the Raman fields.

3.4 Chiral spin liquids in Kagome lattice

Frustration in lattice spin systems, in which local energy constraints cannot all be satisfied, can lead to deconfined phases of quantum spin liquids (QSL). In a QSL, quantum fluctuations drive the collective state of the spins into highly entangled quantum matter, such as the resonating-valence bond state in Z_2-spin liquids, whose emergent topological properties can only be described in terms of long-range entanglement [21]. Unlike gapped Z_2-spin liquids, chiral spin liquids (CSL) spontaneously break the time-reversal and parity symmetry, while preserving other symmetries, and host fractional quasiparticle excitations with topological order [90]. Such a CSL is thought to be a parent state of the illusive anyonic superconductor.

As an example of Eq. 3.6, we discuss a method of creating topological CSL discovered by Kalmeyer and Laughlin, a bosonic analogue of the celebrated fractional quantum Hall effect [91–93], with our waveguide QED toolboxes. We consider an anisotropic antiferromagnetic

XXZ Hamiltonian

$$\hat{H}_{\rm CSL} = \sum_{\langle ij \rangle} \left(J_\perp \hat{\sigma}_\perp^{(i)} \hat{\sigma}_\perp^{(j)} + J_{ZZ} \hat{\sigma}_z^{(i)} \hat{\sigma}_z^{(j)} \right) + \lambda \hat{\chi}, \tag{3.8}$$

on a Kagome lattice with tunable spin-chirality $\hat{\chi}$. Despite the physical dimension of the atomic lattice in 1D PCWs, our toolboxes allow the spins to sit on a synthetic geometry provided by the connectivity of the translationally-variant spin-exchange couplings, as depicted by the 2D Kagome lattice in Fig. 3.2. With $\lambda = 0$, $\hat{H}_{\rm CSL}$ reduces to the Kagome XXZ antiferromagnet, which has been widely studied for its time-reversal symmetric Z_2 spin liquid [94, 95].

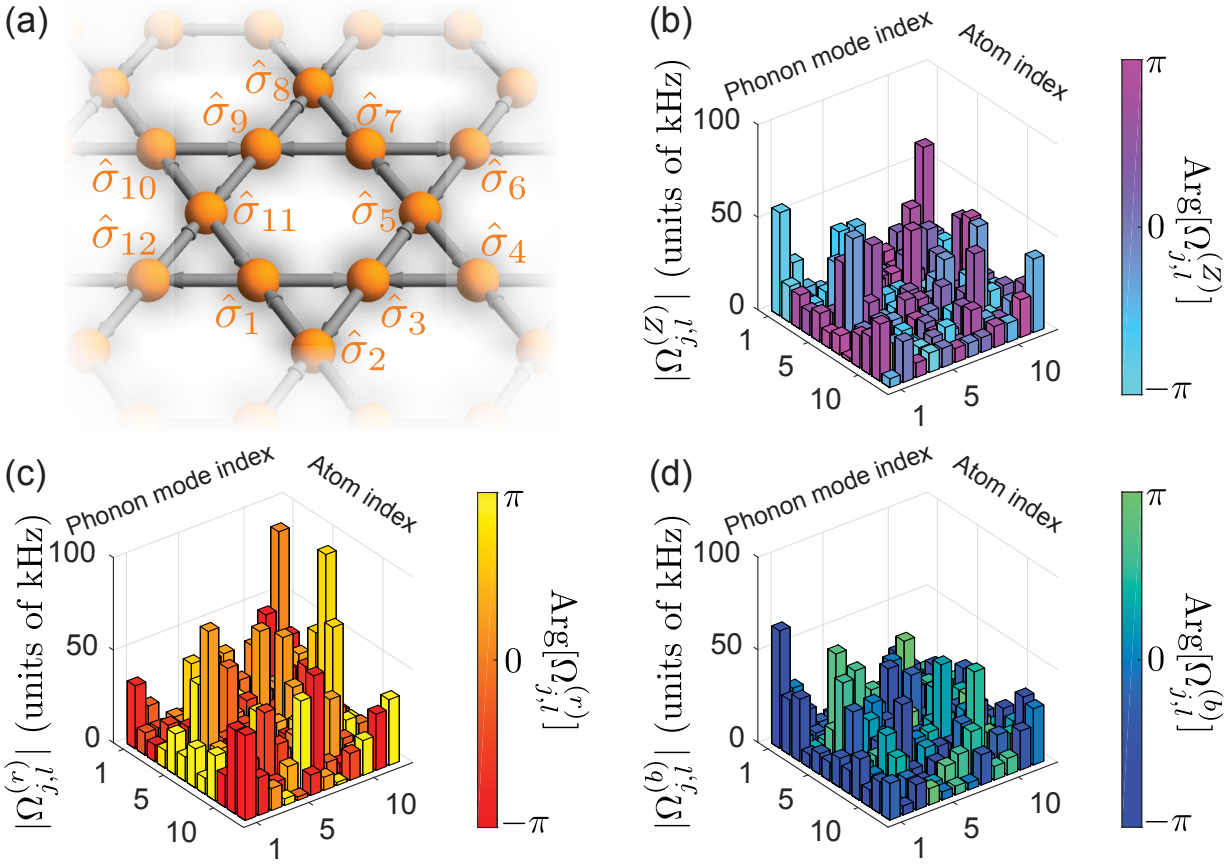

Figure 3.2: Chiral spin liquid phase in Kagome lattice with vector-spin coupling. (a) Antiferromagnetic Heisenberg model $\hat{H}_{\rm AF}$ with Dzyaloshinskii-Moriya interaction $\hat{\chi}_{\rm vector}$ is illustrated for spins in an artificial Kagome lattice. The grey arrows indicate the sign of the vector coupling in $\hat{\chi}_{\rm vector}$. Panels (b)–(d) Raman sidebands realize $\hat{H}_{\rm CSL}$ in Eq. 3.8 with tunable chirality $\hat{\chi}_{\rm vector}$ for $J_\perp = J_{ZZ} = 0.5$kHz and $\lambda = 0.1$kHz. Adiabatic evolution through a paramagnetic phase with time-dependent sidebands prepares the chiral spin liquid for cold atoms in PCWs.

In the presence of strong chiral interactions on the triangles Δ of the sublattice, e.g., scalar spin-chirality $\hat{\chi}_{\rm scalar} = \sum_{i,j,k\in\Delta} \vec{\hat{\sigma}}_i \cdot (\vec{\hat{\sigma}}_j \times \vec{\hat{\sigma}}_k)$, the ground state supports a topologically-

protected chiral edge mode circulating the macroscopic outer boundary with closed loops within the inner hexagons of the Kagome lattice [91]. As a convention, the sum $\sum_{i,j,k\in\Delta}$ runs clockwise over the nearest-neighbor sites around the triangles. To see how the extended chiral edge modes emerge in a Kagome lattice, we first identify that the ground state of a single closed loop $\hat{\chi}_{\text{scalar}}$ around a single triangle is the Kalmeyer-Laughlin wavefunction. By mapping the elementary triangular puddles into a Kondo-type network for edge states [91], individual puddles encircled with the chiral states merge together to develop a macroscopic puddle with a single chiral topological edge state around the outer boundary of the lattice, reminiscent of the two-channel Kondo problem. This allows for unidirectional spin transport along the boundary, and the bulk excitations are described by semionic exchange statistics ($\phi = \pi$).

The difficulty in realizing Eq. 3.8 as the low-energy theory of physical Hamiltonians with cold atoms is the spin-chiral coupling $\vec{\hat{\sigma}}_j \times \vec{\hat{\sigma}}_k$ that breaks the parity symmetry. The capability to realize universal pairwise interaction, including off-diagonal spin operators $\hat{\sigma}_\alpha \hat{\sigma}_\beta$, makes our approach highly suitable for analog quantum simulation of quantum liquids with chiral spin coupling. As an example, we realize here the minimal instance of CSL with 2-body vector chirality $\hat{\chi}_{\text{vector}} = \sum_{i,j\in\Delta} \hat{z} \cdot (\vec{\hat{\sigma}}^{(i)} \times \vec{\hat{\sigma}}^{(j)})$ in the form of Dzyaloshinskii-Moriya (DM) interaction. The Raman sideband matrices shown in Figs. 3.2(b)–(d) realize Eq. 3.8 on a unit cell of a Kagome lattice in Fig. 3.2(a). The DM interaction breaks the underlying SU(2) symmetry, while preserving the lattice and U(1) spin symmetry. Hence, unlike the case of $\hat{\chi}_{\text{scalar}}$, the CSL does not persist for $\hat{\chi}_{\text{vector}}$ in the limit of strong coupling $\lambda \gg J_\perp = J_{ZZ}$. However, it is numerically predicted that gapped CSL phase does exist for XXZ antiferromagnets with a finite vector spin-chirality $\lambda < J_\perp = J_{ZZ}$ at zero magnetic field [92, 93]. The capability to tune vector-chirality as well as other spin-orbit couplings also opens the route to synthetic multiferroics and emergent interfacial spin textures, including skyrmions and topological surface states.

3.5 Gauging waveguide QED simulator to interacting SU(n) lattice models

The native Hamiltonian of our waveguide QED simulator spans the universal binary analog models of SU(2)-spin operators. In analogy to lattice gauge theories (LGT) that give rise to constrained Hilbert space [96, 97], we can also design dynamical gauge structures that mediate a wide range of binary models consisting of SU(n)-operators in a completely analog fashion, such as the Heisenberg quantum magnet for interacting SU(n)-spins. While the digital quantum simulator can emulate the dynamics of arbitrary unitary dynamics,

we confine our discussion here to binary SU(n)-spin models that arise within the projected gauge-invariant subspace of the parent's SU(2) waveguide QED simulator. Such a "condensed matter" approach [96] can create deconfined quantum phase by direct cooling to its ground state, and the errors can be mitigated within the gauge sector of interest. Indeed, instead of merely replicating the target quantum state as with digital quantum simulators, the actual physical phenomena is encoded onto the low-energy sector of the waveguide QED simulator. In this section, we discuss a general Heisenberg SU(n) quantum magnet as an exemplary implementation, but more complex models involving vector and anisotropy can be realized in an analogous fashion.

Our goal is to create a programmable Heisenberg magnet $\hat{H}_{\rm H} = \sum_{j>i} \mathcal{J}_{ij} \sum_\alpha \hat{\Lambda}_\alpha^{(i)} \hat{\Lambda}_\alpha^{(j)}$, where $\hat{\Lambda}_\alpha$ is the generalized Gell-Mann matrix (3.10.1). The challenge of simulating SU(n)-spin with cold atoms and ions is that the spin operators cannot be efficiently mapped to a rotation within an internal DOFs due to limited transition pathways, e.g., selection rules. In addition, there is a difficulty to implement spin-models with certain symmetries that cannot be imposed to the fundamental symmetries of the atomic interactions, e.g., SU(n)-symmetric collisions in alkali-earth atoms limited by the nuclear spin DOF [98]. Apart from the programmability of $\mathcal{J}_{ij}$, the n^2-1 generators of SU(n) algebra and their interactions would need to be mapped to the physical system. Our method eliminates both bottlenecks, by locally encoding an ensemble of SU(2) spins to the SU(n)-subspace, and by building the interaction symmetry directly into the Hamiltonian in an emergent manner.

The general strategy is to impose an effective local gauge symmetry onto the spin system through the separation of time scale. We can then introduce a perturbative spin-exchange term that only virtually breaks the local symmetries. By construction, we aim to obtain a microscopic many-body dynamics within the gauge sector, which can be effectively interpreted as the macroscopic binary interactions between the SU(n) spins. From the viewpoint of lattice gauge theories, the constrained quantum dynamics can be qualitatively understood as quantum fluctuations within the background gauge field of a frustrated vacuum of the logical spin system, which give rise to a physical 4-body plaquette interaction.

As shown in Fig. 3.3, we partition the physical atomic lattice i, j into logical spins $\bar{i}, \bar{j} \in \mathcal{L}$, each containing n physical atoms, that encode the local SU(n) spin. This is achieved by local U(1)-gauge constraints $\hat{G}_{\bar{i}}$ that blockade the total excitation number within the logical spin $\bar{i}$ to reside in the single-excitation subspace $\{|\alpha\rangle \equiv |s_\alpha\rangle \prod_{\beta\neq\alpha} |g_\beta\rangle\}$ with $\alpha \in \{1 \cdots n\}$. Such a gauge generator $\hat{G}_{\bar{i}} = \sum_{i\in\bar{i}} \hat{\sigma}_z^{(i)} - \mathcal{Q}$ effectively imposes the Gauss law ("ice rules") with electric charge $\mathcal{Q} = n-2$, analogous to quantum spin ice models [21, 96] that mediate long-range ring-exchange interactions. The ground state (most excited state) sector of $\hat{H}_G = \lambda_G \sum_{\bar{i}} \hat{G}_{\bar{i}}^2$ for $\lambda_G > 0$ ($\lambda_G < 0$) is spanned by n-

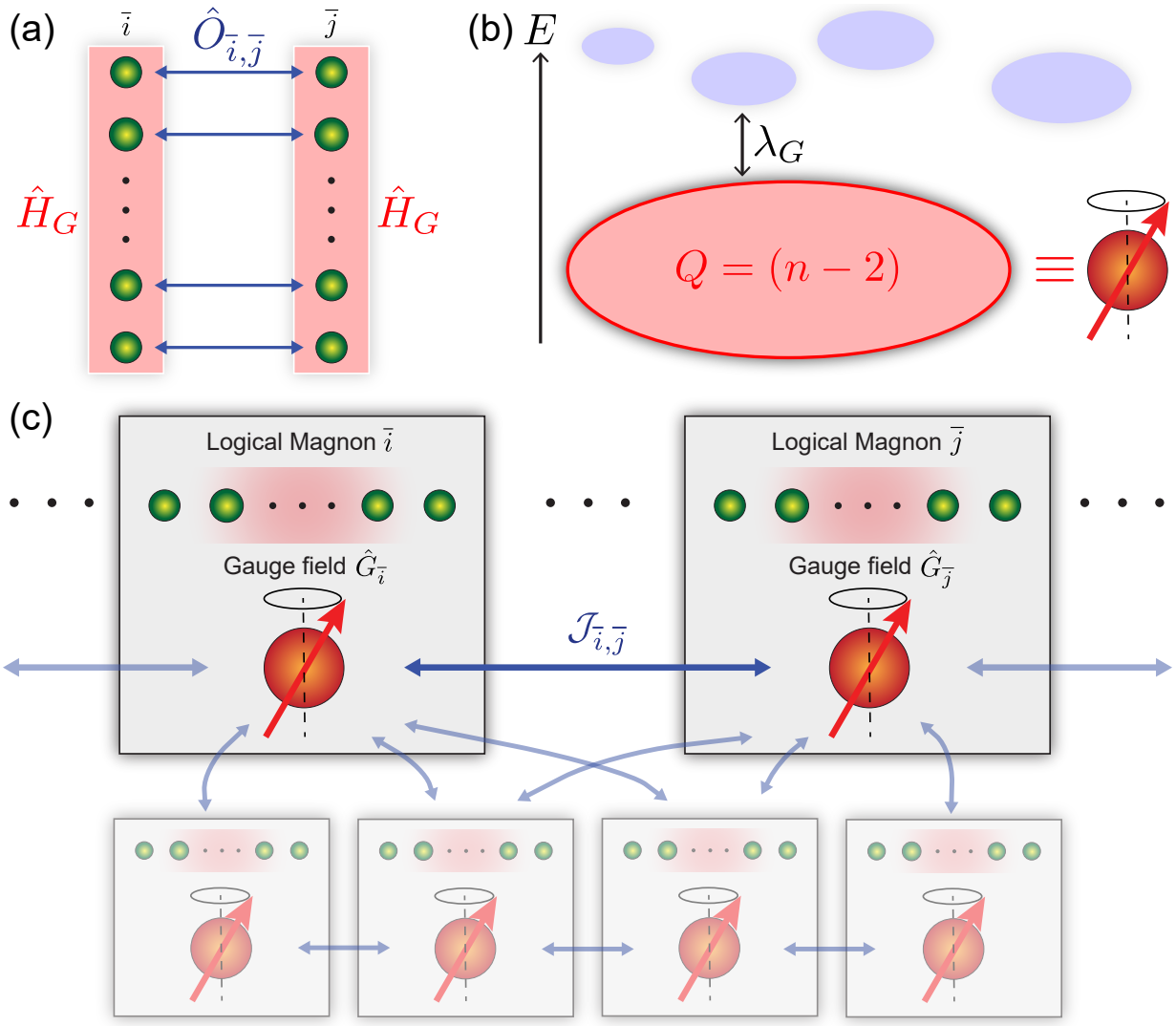

Figure 3.3: SU(n)-spin networks under spin ice gauge constraints. (a) Parent spin ice Hamiltonian. Trapped atoms in PCWs are subjected to local "ice" rules (Gauss laws) with an energetic cost $\hat{H}_G = \lambda_G \sum_{\bar{i}} \hat{G}_{\bar{i}}^2$ within logical blocks $\bar{i}, \bar{j}$. Quantum dynamics among the ice states is induced by a perturbative spin-exchange $\hat{O}_{\bar{i},\bar{j}}$ between atoms belonging to different blocks. (b) Effective reduction of the Hilbert space into gauge sectors. The low-energy dynamics is constrained within the SU(n) single-excitation sector, represented by a gauge charge $Q = n-2$, with errors protected by a many-body gap λ_G. (c) The global spin network is transformed into a network of logical SU(n) spins $\bar{i}, \bar{j}$ by encoding the SU(n)-spin with a collection of n SU(2)-spins. U(1)-gauge constraints $\hat{G}_{\bar{i}}$ block the excitation manifold within the logical spin so that the energy sectors of the parent Hamiltonian are separated by the total excitation number. Spin-exchange coupling between atoms belonging to different logical blocks $\bar{i}, \bar{j}$ induces an effective two-body interactions between SU(n) spins.

dimensional states $\{|\alpha\rangle\}$ of the SU(n)-representation. Without the loss of generality, we

rewrite the Heisenberg model within this definition,

$$\hat{H}_{\mathrm{H}} = \sum_{\bar{i}\neq\bar{j}} \mathcal{J}_{\bar{i},\bar{j}} \sum_{\alpha,\beta} \hat{\mathcal{T}}^{(\bar{i})}_{\alpha\beta} \hat{\mathcal{T}}^{(\bar{j})}_{\beta\alpha}, \tag{3.9}$$

where $\hat{\mathcal{T}}_{\alpha\beta} = |\alpha\rangle\langle\beta|$.

In order to introduce spin-spin interaction between the logical blocks, we treat the primitive Hamiltonian $\hat{H}_I = \sum_{\bar{i},\bar{j}} \hat{D}_{\bar{i},\bar{j}} + \hat{O}_{\bar{i},\bar{j}}$ as a perturbation to $\hat{H}_G$ with $\hat{D}_{\bar{i},\bar{j}} = D_{\bar{i},\bar{j}} \sum_\alpha \hat{\sigma}^{(\bar{i}_\alpha)}_{ss} \hat{\sigma}^{(\bar{j}_\alpha)}_{ss}$ and $\hat{O}_{\bar{i},\bar{j}} = O_{\bar{i},\bar{j}} \sum_\alpha \hat{\sigma}^{(\bar{i}_\alpha)}_{+} \hat{\sigma}^{(\bar{j}_\alpha)}_{-}$, where $\hat{\sigma}^{(i_\alpha)}$ denotes the spin operator acting on the α^{th} atom in the i^{th} logical block. With the local gauge constraints, we obtain the effective Hamiltonian within the gauge-invariant sector $\mathcal{Q}$ as

$$\hat{H}_{\mathrm{eff}} = \sum_{\bar{i}\neq\bar{j}} D_{\bar{i},\bar{j}} \sum_{\alpha} \hat{\mathcal{T}}^{(\bar{i})}_{\alpha\alpha} \hat{\mathcal{T}}^{(\bar{j})}_{\alpha\alpha} + \mathcal{J}_{\bar{i},\bar{j}} \sum_{\alpha\neq\beta} \hat{\mathcal{T}}^{(\bar{i})}_{\alpha\beta} \hat{\mathcal{T}}^{(\bar{j})}_{\beta\alpha}, \tag{3.10}$$

with the gauge-variant errors (spinon excitations) suppressed by the many-body gap λ_G (spinon energy). In the physical space, the spin-exchange coefficients $D_{\bar{i},\bar{j}}, \mathcal{J}_{\bar{i},\bar{j}} = -O^2_{\bar{i},\bar{j}}/2\lambda_G$ are the gauge-mediated ring-exchange interactions among the four spins selected by the primitive two-body model $\hat{H}_I$. With $D_{\bar{i},\bar{j}} = \mathcal{J}_{\bar{i},\bar{j}}$, the effective Hamiltonian is mapped to the universal SU(n)-Heisenberg magnet $\hat{H}_{\mathrm{H}}$. The gauge-projected Hamiltonian is derived in 3.10.2.

One feature of our synthetic approach is that the symmetries of the interaction can be directly built into the underlying Hamiltonian, without resorting to the fundamental symmetries of the atomic collisions. For instance, with a minor modification, we can easily create SU(n)-symmetric Hamiltonians for arbitrary n, e.g., unlimited by the nuclear-spin DOF, for the study of transition metal oxides [99] and heavy fermion systems. Furthermore, because we can design $\mathcal{J}_{\bar{i},\bar{j}}$ arbitrarily through the Raman fields, our system can be tailored to study novel frustrated magnetic ordering in long-range SU(n)-spin models with the Haldane gap [100–103]. As discussed in the next section, our waveguide QED simulator can be applied to the realization of quantum field theories [79, 104].

In 3.10.3, we discuss an efficient method to construct the real-time evolution of the Sachdev-Ye (SY) model [105] with dynamical Raman fields, an all-to-all $\lim_{n\to\infty}$SU(n)-Heisenberg model $\hat{H}_{\mathrm{SY}}$ (Eq. 3.9 with Gaussian-random $\mathcal{J}_{\bar{i},\bar{j}}$). The SY model describes a non-Fermi liquid state of matter, known as the "strange metal," characterized by the absence of long-ranged quasiparticle excitations analogous to high-T_c cuprate superconductors. In connection to quantum chaos [77], a quenched system under $\hat{H}_{\mathrm{SY}}$ rapidly loses the phase coherences and reaches a quantum many-body chaos within time scales that remarkably saturate the quantum bound of the Lyapunov time $\tau_L = \frac{\hbar}{2\pi k_B T}$. With

gauge-mediated many-body string Hamiltonian between a set of SU(n)-spins and an ancilla qubit, we can even directly assemble and measure arbitrarily complex OTOCs [106–108] $\langle \hat{W}^\dagger(\tau)\hat{V}^\dagger(0)\hat{W}(\tau)\hat{V}(0)\rangle \sim e^{\tau/\tau_L}$ for SU(n)-variables $\hat{W}, \hat{V}$ in our platform for the detection of the quantum chaos and the scrambling of entanglement in many-body quantum systems. The SY model also serves as a model of holography that duals quantum gravity in AdS_2/CFT [77, 105].

3.6 Strongly-coupled WZW field theory

Quantum field theories (QFT), defined on continuous spacetimes with each site supporting infinite-dimensional Hilbert spaces, become increasingly intractable to simulate in the regime of strong coupling even on quantum devices. Near the strong coupling, the physics of the UV fixed point is often described by conformal field theories (CFT) with a scale-invariant and universal description. Moreover, extracting the conformal data of the emergent CFT is a notoriously difficult task for real quantum hardwares. In an examplary fashion, we demonstrate the emergence of (1+1)D SU$(n)_k$ Wess-Zumino-Witten (WZW) CFT [79, 104, 109] in the waveguide-coupled SU(n) Hamiltonian (Fig. 3.4(a)), which describes the boundary physics of a bulk $(2+1)$D Chern-Simons topological gravity in the scaling limit [110]. In condensed matter systems, WZW theory serves as the parent that hosts a family of symmetry-protected gapless edge states in fractional quantum Hall systems. The primary fields Ψ of the CFT are produced and monitored by way of real optical fields of the guided modes. The long-wavelength conformal data, including the central charge c, the quantum dimensions $\mathcal{D}$, and operator product expansion of Ψ, is reconstructed from the correlation between physical observables of the microscopic simulator, as reflected by the fluctuation of the optical fields in the guided mode.

As discussed in Fig. 3.4(a), we consider a critical SU(3)-Heisenberg Hamiltonian for nearest-neighbor interacting N_{eff} logical SU(3) spins living on a ring with $\mathcal{J}_{\bar{i},\bar{i}+1} = \mathcal{J}_c$ for Eq. 3.9 (See the phase diagram of Fig. 3.4(b) with quantum critical point $\theta_{\text{ULS}} = \pi/4$). The target system is mapped to the waveguide QED simulator (i) by creating nearest-neighbore bonds between physical atoms with $\hat{H}_I$ (blue arrows of Fig. 3.4(a)) and (ii) by gauging the simulator to $\mathcal{Q}$ (red shaded area of Fig. 3.4(a)). The gauged spectra of the simulator (with λ_G) is thereby that of the target with an error $(D/\lambda_G)^2 \ll 1$. To access the ground state $|\tilde{g}\rangle$ of the target model (most excited state of the gauged simulator), we perform a hybrid matrix-product state (MPS) algorithm for the waveguide quantum simulator moving along a complex time, combining both density-matrix renormalization group (DMRG) and time-evolving block decimation (TEBD) methods. By evolving a

random MPS under the action $\lim_{t\to\infty}\exp\left[-i(\hat{H}_I+i\hat{H}_G)t\right]$, we obtain the most excited state within the low-energy sector $\mathcal{Q}=1$ of the simulator, which is isometric to the DMRG ground state of the logical antiferromagnetic SU(3) model (3.10.4).

To see how the $\mathrm{SU}(3)_1$ WZW CFT for level $k=1$ natively emerges from the Hamiltonian constraints of the simulator, let us consider the parton picture of the target Hamiltonian (See Eq. 3.9). We map the logical operators with 3-color fermions (quarks) $\hat{\mathcal{T}}^{(\bar{i})}_{\alpha\beta}=\hat{\psi}^{(\bar{i})\dagger}_{\alpha}\hat{\psi}^{(\bar{i})}_{\beta}$ under the constraint $\hat{\psi}^{(\bar{i})\dagger}_{\alpha}\hat{\psi}^{(\bar{i})}_{\alpha}=1$ for colors $\alpha,\beta=\{r,g,b\}$. The parton Hamiltonian

$$\hat{\mathcal{H}}_{\text{parton}}=\mathcal{J}\sum_{\bar{i}}\hat{\psi}^{(\bar{i})\dagger}_{\alpha}\hat{\psi}^{(\bar{i})}_{\beta}\hat{\psi}^{(\bar{i}+1)\dagger}_{\beta}\hat{\psi}^{(\bar{i}+1)}_{\alpha} \tag{3.11}$$

is equivalent to a SU(3) Hubbard model $\mathcal{H}_{\text{Hubbard}}=-\sum_{\bar{i}}t[\hat{\psi}^{(\bar{i})\dagger}_{\alpha}\hat{\psi}^{(\bar{i}+1)}_{\alpha}+h.c]+U[\hat{\psi}^{(\bar{i})\dagger}_{\alpha}\hat{\psi}^{(\bar{i})}_{\alpha}-1]^2$ for fermions in the interaction limit $U/t\gg 1$. In the infrared, low-energy excitations are only populated at the Fermi points $k_F=\pi/3$, thereby coarse-graining the fermionic fields $\hat{\psi}^{(\bar{i})\dagger}_{\alpha}=e^{ik_Fx_{\bar{i}}}\hat{\psi}_{L,\alpha}(x_{\bar{i}})+e^{-ik_Fx_{\bar{i}}}\hat{\psi}_{R,\alpha}(x_{\bar{i}})$ to the continuum. As the Hubbard model for $U/t\ll 1$ gives rise to 3-color free Dirac fermions (charge boson and $\mathrm{SU}(3)_1$ WZW gauge fields g), the Hubbard interaction asymptotically decouples the charge with a gap. Thus, the Hubbard interaction leaves the WZW fixed point in the low-energy sector with an action $S=\frac{1}{16\pi}\int_{\mathcal{G}^2}d^2\xi\mathrm{Tr}[\partial_\alpha g^{-1}\partial^\alpha g]+\Gamma(g)$ and topological term $\Gamma(g)=\frac{1}{24\pi}\int_{\mathcal{G}^3}d^3\xi\epsilon^{\alpha\beta\gamma}\mathrm{Tr}[(g^{-1}\partial_\alpha g)(g^{-1}\partial_\beta g)(g^{-1}\partial_\gamma g)]$. This is reminiscent to chiral Luttinger liquids (LL) on fractional quantum Hall edges [111]. Unlike the Haldane phase of the spin-1 counterpart, the emergent field theory of the SU(3) model is described by universal properties, where the (chiral) fermionic fields $\hat{\psi}_{L,\sigma},\hat{\psi}_{R,\sigma}$ become the Virasoro primary fields $g_{\alpha\beta}(z,\overline{z})=\hat{\psi}^{\dagger}_{L,\sigma}(z)e^{i\hat{\phi}(z,\overline{z})}\hat{\psi}_{R,\sigma}(\overline{z})$ of the WZW CFT with colors $\sigma=\{r,g,b\}$ and space-time $z=-i(x-t),\overline{z}=i(x+t)$. These fields are generated by the spin currents $J^a_L(x)=\frac{1}{2}\hat{\psi}^{\dagger}_{L,\sigma}(x)\tau^a_{\sigma,\sigma'}\hat{\psi}_{L,\sigma'}(x)$ and $J^a_R(x)=\frac{1}{2}\hat{\psi}^{\dagger}_{R,\sigma}(x)\tau^a_{\sigma,\sigma'}\hat{\psi}_{R,\sigma'}(x)$ following the $\mathrm{SU}(3)_1$ Kac-Moody algebra, where $\tau^a_{\sigma,\sigma'}=(\Lambda_a)_{\sigma,\sigma'}/2$ are the elements of the generalized Gell-Mann matrices in 3.10.1. Importantly, from the operator product expansion, the conformal data of $\mathrm{SU}(3)_1$ WZW CFT can be obtained for the central charge $c=2$, scaling dimensions $\mathcal{D}=\frac{2}{3}$ and critical exponents $\nu=2$ for the WZW field $g_{\alpha\beta}$.

In order to physically extract the conformal data from the simulator, we need to measure the static and dynamic response functions. To this end, we dissipate an observable $\hat{\mathcal{O}}^{(j)}$ of the physical atom at site j to the waveguide $\sum_{\bar{j}}g_{\bar{j}}\sum_{j\in\bar{j}}\hat{\mathcal{O}}^{(j)}\hat{a}_{k_0}e^{ik\bar{j}}$ with a well-defined momentum k. The first-order correlation $\langle:\hat{a}^\dagger(\tau)\hat{a}(0):\rangle_k$ of the optical field leaving the guided mode regresses towards the dynamical response function $\mathcal{S}^k_{\mathcal{O}}(\tau)=\langle 0_{\text{CFT}}|\hat{\mathcal{O}}_{-k}(\tau)\hat{\mathcal{O}}_k(0)|0_{\text{CFT}}\rangle$ of the logical spin system, where $|0_{\text{CFT}}\rangle$ is the vacuum state of the WZW CFT and $\hat{\mathcal{O}}_k=\sum_{\bar{j}}\frac{g_{\bar{j}}}{\kappa_0}\sum_{j\in\bar{j}}\hat{\mathcal{O}}^{(j)}e^{ik\bar{j}}$. This method allows us to construct

a broad class of static and dynamical structure factors of the many-body system, giving access to the low-energy excitations as well as the universal properties ν and $\mathcal{D}$ of the CFT. In 3.10.4, we analyze our result for the spin correlators $\langle \hat{S}_z^{(\bar{i})} \hat{S}_z^{(\bar{j})} \rangle \sim |\bar{i} - \bar{j}|^{-2\mathcal{D}}$ and extrapolate the scaling dimensions $\mathcal{D} = 0.67 \pm 0.02$ with the DMRG ground state up to $N_{\text{eff}} = 200$ logical blocks. We also characterize the correlation length $\xi \sim |\theta - \theta_c|^{-\nu}$ with the critical exponents $\nu = 2.10 \pm 0.05$ for the bilinear biquadratic (BBQ) spin-1 Hamiltonian with Uimin-Lai-Sutherland (ULS) quantum critical point (QCP) $\theta_c = \pi/4$ with an enlarged SU(3)-symmetry, corresponding to our SU(3) Heisenberg model.

In Fig. 3.4(b), we present the phase diagram of the BBQ model detected with the static spin structure factor $\mathcal{S}_{zz}^k = \langle \hat{S}_z^{-k} \hat{S}_z^k \rangle$. Near the ULS QCP, power-law singularities appear in the form of pinch points at the momentum $k = 2\pi/3$ and $4\pi/3$, indicative of absence of long-range order (disordered state) for the SU(3) spin model and the gapless soliton excitations on top of the CFT vacuum (algebraic spin liquid state). These topological solitons appear to carry anyonic statistics with Abelian phase $\phi = \pi$. Upon locally quenching the many-body system with $\hat{S}_z^{(i)}$, these solitons can be produced in pairs moving at the Fermi velocity $v_F = \pi/3$ (Fig. 3.4(d)). To assess the spectral properties of WZW fields, we probe the dynamical structure factor $\mathcal{S}_{zz}(w, k) = \int \exp(iw\tau) \mathcal{S}_{zz}^k(\tau)$ in Fig. 3.4(e). Two soliton modes are visible in the contour map $\mathcal{S}_{zz}(w, k)$ (See the two solid guiding lines), reflected by their length scales $3/2\pi$ and $3/4\pi$. In addition, the solitonic continuum appears smoothly as the quisiparticle populations between the two solid lines due the coherence between the soliton pairs, and higher order 4-local soliton excitations begin to appear between the dashed black line and the solid red line for $k > 2\pi/3$.

We characterize the central charge c of the CFT by scaling the entanglement entropy $S = -\text{Tr}[\rho_A \ln \rho_A]$ between the subsystems A and B of the logical system with $\rho_A = \text{Tr}_B |0_{\text{CFT}}\rangle\langle 0_{\text{CFT}}|$. In the framework of entanglement Hamiltonian $\tilde{H}_A = \sum_l \tilde{\epsilon}_l |\tilde{\epsilon}_l\rangle\langle\tilde{\epsilon}_l|$, we consider the problem of extracting thermodynamic property of the state $\rho_A = \exp(-\tilde{H}_A) = \sum_l e^{-\tilde{\epsilon}_l} |\tilde{\epsilon}_l\rangle\langle\tilde{\epsilon}_l|$, where $\{\tilde{\epsilon}_l\}$ is the entanglement spectrum for the CFT vacuum state $|0_{\text{CFT}}\rangle$ [112]. The entanglement entropy $S = \sum_l \tilde{\epsilon}_l \ln(\tilde{\epsilon}_l)$ is then obtained from the entanglement Hamiltonian $\tilde{H}_A$ at an effective temperature $T = 1$, whose eigenspectrum $\{\epsilon_l\}$ is determined by many-body spectroscopy [113, 114]. Importantly, due to the Bisognano-Wichmann theorem, the entanglement Hamiltonian $\tilde{H}_A$ can be cast in terms of the original model $\hat{H}_H$ (See Eq. 3.9) with inhomogeneous coupling $\mathcal{J}_{\bar{i},\bar{i}+1} = \mathcal{J}_c \Gamma(\bar{i})$ and prefactor $\Gamma(x) = \frac{N_{\text{eff}}}{\pi} \sin\left(\frac{\pi x}{N_{\text{eff}}}\right)$ defined over a subsystem $\bar{i} \in A$ [112], which can be simulated by the SU(N) toolbox of Eq. 3.10.

In Fig. 3.4(c), we present our result of the entanglement entropy for SU(3) Heisenberg model. At quantum critical points in (1 + 1)D, the vacuum-state entanglement entropy

$S(x, N_{\text{eff}})$ logarithmically scales with the system size N_{eff}, following the Calabrese-Cardy formula $S(x, N_{\text{eff}}) = \frac{c}{3} \log \left[\left(\frac{N_{\text{eff}}}{\pi} \sin \left(\frac{\pi x}{N_{\text{eff}}} \right) \right) \right]$ for the bipartite cut x up to a non-universal offset [115]. By fitting to the Calabrese-Cardy formula, we thereby obtain the central charge $c = 2.05 \pm 0.03$, consistent with the CFT prediction $c = 2$. In the parton theory, the $c = 2$ WZW CFT is manifested by the two-component non-Abelian bosons of the Luttinger liquid. The tensor product of compactified bosons, each carrying $c = 1$ in the dual space, effectively give rise to the $c = 2$ field theory for the SU(3)-symmetric spin model.

As a final remark, while this section focused on the minimal instance $(1 + 1)$D $\text{SU}(3)_1$ WZW CFT, our waveguide QED simulator and meausrement protocols are directly applicable to a wider class of WZW CFT. Namely, the symmetry group $\text{SU}(n)_k$ and level k can be engineered with the local encoding $n = N/N_{\text{eff}}$ and the sector $\mathcal{Q}$, and long-range interactions can be introduced for arbitrary spatial dimensions. Unlike the Abelian-like spin liquids described by $\text{SU}(3)_1$ WZW CFTs, $\text{SU}(3)_k$ WZW CFTs are genuinely interacting CFTs, and host a far richer family of non-Abelian anyons.

3.7 Discussion

Realization of universal quantum matter with waveguide QED simulator presents technological challenges which can be addressed by state-of-art nanophotonic experiments [59–62]. Defect-free atomic arrays can be generated in free-space with acousto-optical deflectors [116, 117] and spatial light modulators [118]. With evanescent cooling and advanced side-illumination loading techniques for PCW structures [57, 119], it is conceivable to prepare defect-free atom array on flat-band PCWs, such as the SPCW. In 3.9, we provide an example of a SPCW tailored to achieve the desired photonic bands for renormalizing individual Cs atoms to universal quantum matter. Programmable control of the exchange coefficients requires the capability to tune $\sim N^2$ phase-amplitudes of the Raman sideband matrices in tandem. Such a capability has been adapted for 100-spin coherent Ising machine [120, 121], and ultrafast multimode modulation techniques have been developed in the telecommunication industry. With present state-of-art technologies, it is thus perceivable that the universal quantum matter consisting of several tens of atoms could be realized with the proposed waveguide QED platform. We remark that there are also active research integrating 2D PCWs with cold atoms [122].

In the waveguide QED simulator, the correlated Lamb shift in the PCW generates mechanical interaction between the external motional states of the trapped atoms. In turn, the Bogoliubov phonons are exploited as a quantum bus for mediating the universal Hamiltonian. Compared to other networked quantum architectures, the PCW allows

a versatile control over both the dissipative loss and coherent dispersion (single-particle band structure) of such a bus. The figure of merit $\mathcal{F}$ provides a natural scaling parameter for the coherence-to-dissipation ratio of the simulator. In the reactive regime, $\mathcal{F} \sim m_e \exp(L_d/L_c) \gg 1$ exponentially improves with longer device length L_d for a given photon mass m_e. As an example, in 3.9, we numerically simulate the Green's function $G_{1\mathrm{D}}(\hat{x}_i, \hat{x}_j)$ and find $\mathcal{F} \sim 10^4$ for the Silicon Nitride SPCW structure.

In conclusion, we have proposed the realization of universal quantum matter with the waveguide QED platform. Compared to previous analogue simulation proposals, our platform stabilizes *universal* Hamiltonians that can be adapted to the emulation of arbitrary quantum matter [53]. Physically, our networked approach allows the direct control of the 2-local Hamiltonian $\hat{H}_{\mathrm{QMA}}$ at the operator level. Moreover, the static and dynamical structures of arbitrary k-local Hamiltonian $\hat{H}_{\mathrm{target}}$ with $k > 2$ of arbitrary dimension can be prescribed to the low-energy theory of the waveguide QED simulator. In particular, we discuss the emergence of programmable binary SU(n) models by gauging the waveguide QED simulator. Indeed, the SU(n) models should be considered as the application of the "universality" of the simulator, by which the target SU(n) physics is encoded onto the low-energy theory of the waveguide QED simulator. For instance, we have analyzed the paradigmatic quantum field theory, the Wess-Zumino-Witten model by accessing phase diagrams, static and dynamical response functions, and CFT entanglement of the many-body system with matrix product states.

With respect to digital approaches, the crucial difference is that $\hat{H}_{\mathrm{target}}$ is in fact manifested entirely by the waveguide QED simulator. That is, not only the quantum state, but also the entire spectrum of $\hat{H}_{\mathrm{target}}$ in tandem is emulated by another physical system. Cooling, thermalization, and dynamics of target quantum model can be mapped to the same equilibrium and non-equilibrium physics of the parent analogue quantum system. Thus, our approach promises a universal analogue quantum simulator, where all physical properties can in principle be replicated as an *emergent* phenomena.

Waveguide QED offers a unique playground for neutral atoms, in which light, motion and spin are all intertwined by the electromagnetic vacuum of the dielectric. By engineering the coupling between the phononic superfluid and the atomic spins, we have provided an analogue framework for simulating universal quantum matter with cold atoms. Such a simulator can be applied for universal quantum computation with continuous-time quantum cellular automata and Hamiltonian quantum computation [47–49]. Our waveguide QED simulator utilizes largely non-interacting phonons with $L_c \gg x_0$. In the limit $L_c \simeq x_0$, the kinetic term of the extended Bose-Hubbard model $\hat{H}_{\mathrm{M}}$ is constrained by the density-density interaction. Under such local gauge symmetries, complex lattice gauge theories beyond truncated quantum link models can emerge from the coherent coupling between

the spin matter and fluctuating gauge phonons, renormalizing ordinary non-interacting matter to quantum field theories with the waveguide dielectric.

3.8 Perfect Transfer in a Spin Chain

To benchmark and verify the various approximations made for Eq. 3.6, we simulate an 1D quantum wire that enables perfect quantum-state transfer (QST) between remote spin registers [123–129]. In particular, we compare the effective dynamics of $\hat{H}_{\rm QST}$ to that of the parent Hamiltonian $\hat{H} = \hat{H}_M + \hat{H}_A + \sum_{i,j}\sum_{\alpha,l} \frac{\Omega_{\alpha,l}^{(j)}}{2}\hat{\sigma}_\alpha^{(i)} \sin(k_{\alpha,l}^{(j)}\hat{x}_i)e^{-i\nu_{\alpha,l}^{(j)}t} + h.c$ in Section 3.3.1. We prepare an 1D spin medium with the translationally-variant XX Hamiltonian

$$\hat{H}_{\rm QST} = \sum_{i=1}^{N-1} \frac{J^{(i,i+1)}}{2}(\hat{\sigma}_x^{(i)}\hat{\sigma}_x^{(i+1)} + \hat{\sigma}_y^{(i)}\hat{\sigma}_y^{(i+1)}), \tag{3.12}$$

where $J^{(i,i+1)} = \alpha\sqrt{i(N-i)}$ and α is a global interaction constant. We solve the system parameters $\{\Omega_{x,k}^{(i)}, \Omega_{y,k}^{(i)}\}$ from the set of nonlinear equations for $J^{(i,i+1)}$ under the constraint of minimum total intensity $\sum_{i,l}(|\Omega_{x,l}^{(i)}|^2 + |\Omega_{y,l}^{(i)}|^2)$.

As discussed in Ref. [123], $\hat{H}_{\rm QST}$ achieves the perfect state transfer of arbitrary input states $|\psi_{\rm in}\rangle$ between the edge sites $i = 1, N$ over arbitrarily long N with unit fidelity by virtue of the mirror symmetry in the spin-exchange coefficients $J^{(i,i+1)}$. Unlike sequential direct state transfer, no external manipulation or feedback on the spin chain is required, and the complete transfer is achieved within transfer time $t_f = \pi/\alpha$ without state-preparation of the global spin chain. In Fig. 3.5(a), we simulate the full Hamiltonian dynamics of quantum-state transfer for two input states $|\psi_{\rm in}^{(1)}\rangle = (|g\rangle - |s\rangle)/\sqrt{2}$ (red line) and $|\psi_{\rm in}^{(2)}\rangle = |s\rangle$ (blue dashed line) through an 1D atomic chain with $N = 6$ atoms without eliminating the phonon fields. We keep the coupling terms between those mismatched sidebands and Bogoliubov phonon modes. By sampling various input states coupled to an initially polarized spin medium, the minimal QST fidelity for pure states is numerically determined $F = {\rm Tr}[|\psi_{\rm in}^{(1)}\rangle\langle\psi_{\rm in}^{(1)}|\rho_s] = 0.994$ at $t_f \simeq \pi/\alpha$, yielding only 0.5% error in the final state, testifying the accuracy of the effective Hamiltonian $\hat{H}_{\rm QMA}$ in Eq. 3.6.

As shown in the inset of Fig. 3.5(a), the phonons across the entire spin chain are hardly populated throughout the state transfer, justifying the adiabatic elimination procedure. In Fig. 3.5(b), we also compare the full atom-phonon dynamics (solid lines) of the individual spin-polarizations $\langle\hat{\sigma}_z^{(i)}\rangle$ for an initially polarized spin medium $|g\cdots g\rangle$ with that of the reduced two-body Hamiltonian $\hat{H}_{\rm QST}$ in Eq. 3.12 (dashed lines). When $|\psi_{\rm in}^{(2)}\rangle$ is injected to the first spin (black line), the spin-excitation delocalizes across the entire spin chain

and coherently builds up the its amplitude at the final spin with $\langle\hat{\sigma}_z^{(6)}\rangle \simeq 1$ at $t \simeq \pi/\alpha$ (red line). The minute difference between the solid and dashed lines affirms the various approximations for $\hat{H}_{\rm QMA}$. In 3.9, we simulate the full open-system dynamics of QST for Eq. 3.12, by starting from the Green's tensor $\boldsymbol{G}(\boldsymbol{x}, \boldsymbol{x}', w)$ of the candidate PCW structure in Fig. 3.1, and incorporate all known dissipative mechanisms intrinsic to our protocol. Such an effective dynamics is shown to be immune from the structural disorders of the PCW at the tolerance levels of state-of-art nanofabrication [130].

3.9 Squircle Photonic Crystal Waveguide

The full realization of our waveguide QED toolboxes requires the capability to maintain favourable figure of merit $\mathcal{F} = \Delta_{\rm Lamb}/\Gamma_{\rm tot}$ with short-ranged mechanical interactions between the trapped atoms, where the localization length $L_c = \sqrt{1/2m_e\Delta_e}$ is comparable to the lattice constant a_0. Here, $\Delta_e \simeq 2\Delta_b$ denotes the detuning of atomic transition to the effective cavity mode [65], and Δ_b is the detuning of the atomic transition frequency to the band edge. While it is not necessary to have nearest-neighbour interactions with sparse loading, the atomic collective motion can experience band-flattening effect due to the long-range phonon tunnelling, which reduces the local addressability of the spin-motion couplings. For laser cooling and trapping nearby the nanoscopic structures, the PCW requires a wide angular field of view for the optical access, and restrict the dimensions of PCW slabs to 1D and 2D. Because of the lack of full 3D PBGs, the total decay rate $\Gamma_{\rm tot} = \Gamma_{\rm 1D} + \Gamma'$ consists of both the waveguide decay $\Gamma_{\rm 1D}$ and the homogeneous decay Γ'. While $\Gamma_{\rm 1D}$ is significantly suppressed for large Δ_e, majority of slow-light PCWs do not have the adequate band structure with large m_e to induce strong coherent motional coupling with $\mathcal{F} \gg 1$ at small L_c.

3.9.1 System parameters

In this section, we discuss a variation of a slotted PCW that utilizes PBG of the 2D slab as the guiding mechanism [131–133]. As shown in Fig. 3.6, the dispersion is tailored by a line defect introduced to a triangular TE-PBG slab, where a significant portion of the energy of the GM is localized within the air slot. We introduce anomalous squircles in the vicinity of the air slots to alter their band curvatures. The rationale of our dispersion engineering is that the combination of the lattice constant a_0, the hole radius r, and the air slot width w_s can tune the locations of the band edge frequencies with respect to the band gap of the slab, while the additional squircle geometries defined by the asymmetry

a, b cause differential energy shifts between the z-even bands of opposite x-symmetry. By placing the bands deep into the PBG of the surrounding slab, we suppress the k-space interval $[k_c, k_l]$ where the in-plane field profile of the GM is localized by index-guiding near the light cone. The proximal squircle geometry then flattens the GM across the band-gap guided k-space fraction $[k_l, k_0]$. In addition, the out-of-plane emission Γ_h is affected by the distance of the squircles to the slot.

We apply a gradient descent algorithm for the SPCW geometry $n(\vec{r})$ (design variables) to minimize the objective function $F_{\text{total}}(n(\vec{r})) = F_c + F_{D2} + F_t$ with intermittent thermal excitations to avoid local extrema, as with simulated annealing. The objective function consists of the contributions from band curvature $F_c \propto |m_e|^{-2}$ and frequency deviations $F_{D2}(F_t) = |\omega_b - \nu_{D2} + \Delta_b|^2(|\omega_b - \nu_t|^2)$ of $|F = 4\rangle \rightarrow |F' = 5\rangle$ transition frequency ν_{D2} (blue-detuned magic wavelength frequency ν_t) for atomic Cesium from the band edges w_b of the respective modes. During the optimization sequence, the complex band diagram is computed to estimate the effective mass m_e and the localization length L_c with plane-wave expansions [134]. After convergence, we switch over to a finite structure with device length L_d and apply a combination of filter-diagonalized FDTD and FDFD methods [135, 136] on a high-bandwidth interconnected computational cluster with the Yee lattice modified to directly optimize the dyadic Green's function $\boldsymbol{G}(\boldsymbol{x}, \boldsymbol{x}', \omega)$ [137, 138] and arrive at the final design variable $n(\vec{r})$ in Table 3.1. To include imperfections of realistic devices, we introduce the uncertainty ± 1 nm to the system variables consistent with the state-of-art PCW nanofabrication techniques [130].

The result of dispersion engineering is shown in Fig. 3.6(a) for our flat-band Silicon Nitride SPCW slab, with the effective mass $m_e = 2.1\ \text{Hz}^{-1} \cdot \text{m}^{-2}$. In the single-band approximation, the localization length is expected to be $L_c \simeq 2a_0$ at $\Delta_e = 0.4$ THz. We assume that the atom is confined by the blue-detuned magic-wavelength GM trap ν_t at $\lambda_t = 793.5$ nm (blue line of Fig. 3.6(a)) with the intensity represented by the blue-colored contour map in Fig. 3.6(d). The excited states of the trapped atom is modified by the vacuum of ν_{D2}-mode (red line of Fig. 3.6(a)) as indicated by the red contour map in Fig. 3.6(d). At the band edge $k_0 = 0.5$, ν_{D2}-mode is highly localized with the effective mode area $A_{\text{eff}} \simeq 0.18\lambda_{D2}^2$. The resulting photonic lamb shift is $\Delta_{\text{1D}} \simeq 620$ MHz at $\Delta_e = 0.4$

Lattice constant a_0	366 ± 1 nm	Slot width w	226 ± 1 nm
Slab thickness t	200 ± 1 nm	Squircle radius r_s	99 ± 1 nm
Secondary radius r'	105 ± 1 nm	Hole radius r	109 ± 1 nm
First line shift l	413 ± 1 nm	Secondary line shift m	729 ± 1 nm
Squircle height a	79 ± 1 nm	Squircle width b	124 ± 1 nm

Table 3.1: Final design variables for the SPCW with slab index $n = 2$. The uncertainty ± 1 nm is added for the normal distributions of the disordered SPCW structure in Fig. 3.7.

THz.

We now turn to the numerical Green's function $\boldsymbol{G}(\boldsymbol{x}, \boldsymbol{x}', \omega)$ of a finite SPCW with device length $L_d = 80a_0$ in Fig. 3.7. We evaluate the collective decay and the coherent interaction

$$\Gamma_{\text{total}}^{(i,j)} = \frac{\mu_0 \omega^2}{\hbar} \text{Im}[\boldsymbol{d}^* \cdot \boldsymbol{G}(\boldsymbol{x}_i, \boldsymbol{x}_j, \omega) \cdot \boldsymbol{d}], \tag{3.13}$$

$$\Delta_{\text{Lamb}}^{(i,j)} = \frac{2\mu_0 \omega^2}{\hbar} \text{Re}[\boldsymbol{d}^* \cdot \boldsymbol{G}_s(\boldsymbol{x}_i, \boldsymbol{x}_j, \omega) \cdot \boldsymbol{d}], \tag{3.14}$$

where the scattering Green's function is $\boldsymbol{G}_s = \boldsymbol{G} - \boldsymbol{G}_0$ with respect to the vacuum $\boldsymbol{G}_0$. More generally, we also define the waveguide Green's function $\boldsymbol{G}_{wg} = \boldsymbol{G} - \boldsymbol{G}_h$ absent the homogeneous (non-guided) contributions $\boldsymbol{G}_h$ (coupling to the lossy modes beyond the light cone and to the free-space modes), where the waveguide portion $\boldsymbol{G}_{wg}$ can be estimated from a multimode cavity model [82] under a single-band approximation, with the resulting decay rate

$$\Gamma_{1\text{D}} = \frac{\mu_0 \omega^2}{\hbar} \text{Im}[\boldsymbol{d}^* \cdot \boldsymbol{G}_{wg}(\boldsymbol{x}_i, \boldsymbol{x}_j, \omega) \cdot \boldsymbol{d}], \tag{3.15}$$

into the waveguide GM.

As shown in Fig. 3.7, in the dispersive regime [61], the flat band ν_{D2} exhibits extreme slow-light enhancement of the decay rate with group index $n_g \simeq 1,000$ near the band edge. As the atom enters the band gap in the reactive regime $\Delta_e > 0$ [62], the waveguide decay rate $\Gamma_{1\text{D}}$ from $\boldsymbol{G}_{wg}$ is exponentially suppressed (red dashed line in Fig. 3.7(b)), while the highly asymmetric Fano-like resonance of $\boldsymbol{G}_{wg}$ around the band edge gives rise to a photonic Lamb shift $\Delta_{1\text{D}} \simeq 620$ MHz (Fig. 3.7(a)) that greatly exceeds $\Gamma_{\text{total}} \simeq 60$ MHz ($\Gamma_{1\text{D}} \simeq 4$ kHz) in the band gap with figure of merit $\mathcal{F} > 10^4$ at $\Delta_e = 0.4$ THz (Fig. 3.7(c)), indicating significant coherence fraction in the collective motion relative to the correlated phononic dissipation. With the close agreement between the numerical Green's function $\boldsymbol{G}$ (black lines) and the waveguide model $\boldsymbol{G}_{wg}$ (red dashed lines) in Fig. 3.7, we can reliably predict Γ_{1D} from $\boldsymbol{G}_{wg}$ and the mechanical loss factor γ_m from both $\boldsymbol{G}_{wg}$ and $\boldsymbol{G}$. Thanks to the large band flatness, we can operate as close as $\Delta_b = 5$ THz ($\Delta_e \simeq 10$ THz) and attain short-ranged motional coupling over $L_c \sim 2a_0 \ll L_d$, while maintaining inherent figure of merit $\mathcal{F} \sim 10^{10}$. We remark that $\mathcal{F}$ is defined as the ultimate coherence-to-dissipation ratio for the collective phonon modes in Section 3.3.1, where we only consider the inherent dissipation of the atomic motions in the photonic band gap. In practice, our method will be realistically limited by the phase-noises of Raman sideband lasers and the inhomogeneous hyperfine broadening of the trapped atoms, as well as various uncontrollable surface forces.

For disordered photonic structures, we compute the dyadic Green's functions with the Gaussian-random geometric disorder ~ 1 nm (positions and sizes of the holes, thickness

of the waveguide) distributed across the entire nanophotonic waveguide. In a single realization, the radiative enhancement factor at the band edge may be hindered by Anderson and weak localization. However, in the reactive regime $\Delta_e > 0$, we observe that the decay rate and the photonic Lamb shift in Fig. 3.7, as well as the nonlocal Green's function $\boldsymbol{G}(\boldsymbol{x}_i, \boldsymbol{x}_j, \omega)$ are not significantly modified by the structural disorders ~ 1 nm (grey dashed lines in Fig. 3.7). Such nano-fabrication tolerances have been demonstrated in Refs. [60, 62]. Because of the nature of the photonic bandgap, the non-radiative atom-field localized modes are resistant to the degree of structural disorder.

3.9.2 Ground-state potentials and phononic modes

We now turn our attention to the trapping mechanism for the atoms in the SPCW. To form an atomic chain, we confine the atoms in the $y-z$ plane by two incoherent side-illumination (SI) beams [58, 61] and localize the x-motion by a weak GM trap at 794 nm, as shown in Fig. 3.8. With the SI beams near the blue-detuned magic wavelengths $\lambda = 687$ nm in an optical accordion, we anticipate efficient loading into the GM trap. Because the SI beam provides additional confinement along z [139–141], we can operate the GM trap away from the band edge at $k_x = 0.48$, thereby reducing the intensity contrast along x. With this protocol we can gain a 3D FORT with trapping potential shown in Fig. 3.8 (d–f).

From the numerical non-local Green's function $\boldsymbol{G}(\boldsymbol{r}_i, \boldsymbol{r}_j, w)$, we observe that the localization length scales with $L_c = \sqrt{1/2m_e\Delta_e}$ and the effective mass $m_e = 2.1\ \mathrm{Hz}^{-1} \cdot \mathrm{m}^{-2}$ up to $\Delta_e \simeq 5$ THz. We attribute the deviation of the localization scaling beyond $\Delta_e > 5$ THz to the residual Lamb shift by the off-resonant couplings to the other bands and to the slab modes. Fig. 3.9 depicts the local nature of external atom-atom interaction $t_{ij} = \eta_l^2 f^2 \Delta_{\mathrm{Lamb}}(x_i, x_j)$ with $\eta_l = x_0/L_c$ relative to the mechanical decoherence $\gamma_m = \eta_l^2 f^2(\Gamma_{1\mathrm{D}} + |\Delta_{\mathrm{Lamb}}/\Delta_e|^2\Gamma')$, where the homogeneous decay rate $\Gamma' \simeq 0.7\Gamma_{\mathrm{vac}}$ is weakly inhibited. At $\Delta_e = 0.4$ THz, we find tunneling rate $t \simeq 2\pi \times 230$ kHz and localization length $L_c = 0.77\mu$m and phonon loss rate $\gamma_m \simeq 2\pi \times 5$ Hz. Another possible error source could be recoil heating from the trapping beam. Since we work with FORT in blue detuning, the heating rate can be estimated as $\gamma_{\mathrm{heat}} \simeq E_r(\Omega_t/\delta_t)^2\Gamma'/\hbar w_t$ [142], where Ω_t and δ_t are trapping Rabi frequency and laser-atom detuning respectively, and $E_r = 4\pi^2\hbar^2/2m\lambda_t^2$ is recoil energy. For cesium atom and our trapping setup, the heating rate is estimated as $\gamma_{\mathrm{heat}} \sim 0.2\mathrm{Hz} \ll \gamma_m$, therefore can be neglected safely.

Beyond the scope of the present work, we have also investigated SPCWs with strong phononic on-site U_0 interactions, which maps the phononic model to XXZ spin magnet and Luttinger liquids for finite filling factor. Further design variation that provides strong

Energy Hierarchy	Expression	Requirements	Typical Value	Effective Error source	Expression	Typical Value
Atom-PCW interaction	$g_c \simeq \sqrt{\frac{\omega_b d^2}{2\epsilon_0 A_{\rm eff} L_c}}$		$\sim$ 10GHz	Photon loss	$\kappa \simeq \kappa_0 \exp(-L_d/L_c) + \frac{g_e^2}{\Delta_e^2}\Gamma'$	$\sim$ 10MHz
Mechanical tunneling	$t_{ij} \simeq \eta_l^2 g_m$	$f \ll 1$	$\sim$ 1MHz	Phonon loss	$\gamma_m \simeq \frac{\eta_l^2 g_m}{\Delta_e}\kappa$	$\sim$ 10Hz
Spin-spin interaction	$J_{\alpha,\beta}^{(i,j)} = 2{\rm Re}[\frac{\tilde{\Omega}_{\alpha,l}^{(i)}\tilde{\Omega}_{\beta,l}^{(j)*}}{\Delta_M}]$	$\lvert\tilde{\Omega}_{\alpha,l}^{(i)}\rvert \ll \Delta_M \ll \lvert\epsilon_{l\pm1} - \epsilon_l\rvert$	$\sim$ 50kHz	Spin decoherence	$\gamma_{\alpha,\beta}^{(i,j)} \simeq \frac{\gamma_m}{\Delta_M} J_{\alpha,\beta}^{(i,j)}$	$\sim$ 0.1Hz

Table 3.2: A summary of energy scale hierarchy and corresponding effective error rates.

phononic density-density interaction $U_{ij}\hat{n}_i\hat{n}_j$ will be discussed elsewhere. Such a constraint on the local phonon field provides a mechanism to impose local symmetry similar to the context of lattice gauge theories in condensed matter systems.

3.9.3 Phonon-mediated spin-exchange coefficient

For universal spin-control with $N \simeq 50$ atoms, we estimate the spin-exchange coupling rate $J_{ij} \simeq 50$ kHz with the intrinsic decoherence rate $\gamma_{\alpha,\beta}^{(i,j)} \ll 1$ Hz at $\Delta_e = 0.4$ THz. As an example, we depict the open-system dynamics of the quantum-state transfer protocol in Fig. 3.10 by solving the master equation (Eqs. 3.6-3.7). As discussed above, because of $\gamma_m/\Delta_M \sim 10^{-4}$, the intrinsic phonon-induced spin decoherence $\gamma_{\alpha,\beta}^{(i,j)}$ is highly negligible. We thereby include the spin-relaxation rate $\gamma_{\rm FORT}^{(i,i)} < 1$ Hz of the FORT beams [143] by adding the following local dissipative terms to the original master equation in Eq. 3.7.

$$\begin{aligned}
\mathcal{L}_{ss}[\hat{\rho}_{\mathcal{S}}] &= -\sum_i \frac{\gamma_{\rm FORT}^{(i,i)}}{2}(\{\hat{\sigma}_{ss}, \hat{\rho}_{\mathcal{S}}\} - 2\hat{\sigma}_{gs}\hat{\rho}_{\mathcal{S}}\hat{\sigma}_{sg}), \\
\mathcal{L}_{gg}[\hat{\rho}_{\mathcal{S}}] &= -\sum_i \frac{\gamma_{\rm FORT}^{(i,i)}}{2}(\{\hat{\sigma}_{gg}, \hat{\rho}_{\mathcal{S}}\} - 2\hat{\sigma}_{sg}\hat{\rho}_{\mathcal{S}}\hat{\sigma}_{gs}).
\end{aligned}$$

We note that, due to the highly differential decay rates for the $D1$ and $D2$ lines of Cs by the SPCW, we do not observe any suppression of Raman spontaneous emission rates relative to the Reyleigh scattering by the FORT. The state-fidelities for $N = 1$ and $N = 6$ atoms are displayed as black and red solid lines n Fig. 3.10, respectively. We assume an initially injected spin state of $|s\rangle$ with the parameters of Fig. 3.5. For the clarity of presentation, the remaining spin-medium is prepared to the ground state $|g\cdots g\rangle$. As the spin-excitation is transferred within the dissipative spin chain, the overall spin medium is thermally depolarized by the actions of the local dissipation and the state-fidelity F is progressively reduced to $F \to 0.5$ with $\hat{\rho}_{\mathcal{S}} \to \prod_i \frac{1}{2}(|g_i\rangle\langle g_i| + |s_i\rangle\langle s_i|)$.

3.10 SU(N)-Gauged Waveguide Qed Simulator

3.10.1 Generalized Gell-Mann matrices

The n-dimensional Hermitian generalized Gell-Mann matrices (GGM) are the higher-dimensional extensions of the Pauli matrices (for qubit) and the Gell-Mann matrices (for qutrit). Similar to the roles which the Pauli (Gell-Mann) matrices play in SU(2) (SU(3)) algebra, they are the standard SU(n) generators. There are three different types of GGMs — $\frac{n(n-1)}{2}$ symmetric ones, $\frac{n(n-1)}{2}$ anti-symmetric ones and $n-1$ diagonal ones, which are defined respectively as

1. Symmetric GGMs ($1 \leq \alpha < \beta \leq n$)

$$\hat{\Lambda}_{\alpha\beta}^{(s)} = |\alpha\rangle\langle\beta| + |\beta\rangle\langle\alpha|, \tag{3.16}$$

2. Anti-symmetric GGMs ($1 \leq \alpha < \beta \leq n$)

$$\hat{\Lambda}_{\alpha\beta}^{(a)} = -i|\alpha\rangle\langle\beta| + i|\beta\rangle\langle\alpha|, \tag{3.17}$$

3. Diagonal GGMs ($1 \leq \alpha \leq n-1$)

$$\hat{\Lambda}_{\alpha\alpha}^{(d)} = \sqrt{\frac{2}{\alpha(\alpha+1)}} \sum_{\beta=1}^{\alpha} |\beta\rangle\langle\beta| - \alpha|\alpha+1\rangle\langle\alpha+1|, \tag{3.18}$$

Hence, in total, we have n^2-1 GGMs. From the definitions, one can verify that, similar to the Pauli matrices, all GGMs are Hermitian and traceless. They are orthogonal and form a basis together with identity $\hat{I}_n$.

3.10.2 Gauge-projected SU(n) Heisenberg model

To gauge the primitive Hamiltonian $\hat{H}_I$ to the local symmetry sector, we define a projection operator $\hat{P}_G$ which brings quantum states to the ground-state sector $\mathcal{Q} = n-2$ of the gauge Hamiltonian $\hat{H}_G$. Namely, $\hat{H}_G\hat{P}_G = \hat{P}_G\hat{H}_G = E_G\hat{H}_G$, where E_G is the ground-state energy of $\hat{H}_G$.

We perturbatively expand $\hat{H}_I$ within the sector $\mathcal{Q}$ with the Kato's series

$$\begin{aligned}\hat{H}_{\rm eff}^{(1)} &= \hat{P}_G\hat{H}_I\hat{P}_G \\ \hat{H}_{\rm eff}^{(2)} &= \hat{P}_G\hat{H}_I\hat{S}_{k1}\hat{H}_I\hat{P}_G \\ \hat{H}_{\rm eff}^{(3)} &= \hat{P}_G\hat{H}_I\hat{S}_{k1}\hat{H}_I\hat{S}_{k2}\hat{H}_I\hat{P}_G \\ &\cdots ,\end{aligned}$$

where $\hat{S}_0 = -\hat{P}_G$ and $\hat{S}_n = [(1-\hat{P}_G)(E_G - \hat{H}_G)^{-1}]^n$. Because $\hat{H}_I$ breaks the local gauge symmetry, the first-order term vanishes $\hat{H}_{\rm eff}^{(1)} = 0$. The low-energy dynamics is thereby described at the second order with

$$\hat{H}_{\rm eff}^{(2)} = \sum_{\bar{i},\bar{j}} \mathcal{J}_{\bar{i},\bar{j}} \Bigg(\sum_{\alpha\neq\beta} \hat{\sigma}_+^{(\alpha,\bar{i})}\hat{\sigma}_-^{(\beta,\bar{i})}\hat{\sigma}_+^{(\beta,\bar{j})}\hat{\sigma}_-^{(\alpha,\bar{j})} \prod_{k\neq\beta}\hat{\sigma}_{gg}^{(k,\bar{i})} \prod_{l\neq\alpha}\hat{\sigma}_{gg}^{(l,\bar{j})} + \hat{\sigma}_{ee}^{(\alpha,\bar{i})}\hat{\sigma}_{ee}^{(\beta,\bar{j})} \prod_{k\neq\alpha}\hat{\sigma}_{gg}^{(k,\bar{i})} \prod_{l\neq\beta}\hat{\sigma}_{gg}^{(l,\bar{j})} + h.c \Bigg), \quad (3.19)$$

where the ring-exchange coefficient $\hat{J}_{\bar{i},\bar{j}} = -\mathcal{O}^2_{\bar{i},\bar{j}}/2\lambda_G$ is mediated by a pair of virtual spinon excitations $\mathcal{Q}' = \mathcal{Q} \pm 2$. By the addition of a gauge-invariant 2-body Hamiltonian $\hat{H}_{\rm anc} = -\sum_{\bar{i},\bar{j}} \left(\mathcal{J}_{\bar{i},\bar{j}} \sum_{\alpha\neq\beta} \hat{\sigma}_{ee}^{(\alpha,\bar{i})}\hat{\sigma}_{ee}^{(\beta,\bar{j})} + \mathcal{D}_{\bar{i},\bar{j}} \sum_{\alpha} \hat{\sigma}_{ee}^{(\alpha,\bar{i})}\hat{\sigma}_{ee}^{(\alpha,\bar{j})} \right)$ to the perturbative Hamiltonian $\hat{H}_{\rm total} = \hat{H}_{\rm anc} + \hat{H}_{\rm eff}^{(2)} + \hat{H}_G$, we obtain the effective Hamiltonian in Eq. 3.10 within the single-excitation gauge sector $\mathcal{Q}$.

3.10.3 Sachdev-Ye quantum magnet

In Section 3.5, we discussed the all-to-all connected SU(n) Heisenberg model. However, as an effective model in terms of second-order perturbation, all connections $\mathcal{J}_{ij}$ must be all negative (ferromagnetic) or positive (antiferromagnetic), determined by the eigenenergy sector that we choose, while fully Gaussian-random-distributed couplings are the crucial ingredients for the generation of quantum chaos of the Sachdev-Ye (SY) model [77, 105]. SY Hamiltonian reads

$$\hat{H}_{\rm SY} = \frac{1}{\sqrt{n}} \sum_{j>i} \mathcal{J}_{ij} \sum_{\alpha} \hat{\Lambda}_\alpha^{(i)}\hat{\Lambda}_\alpha^{(j)}, \quad (3.20)$$

where the after-quench connections $\{\mathcal{J}_{ij}\}$ are drawn from the probability distribution $P(\mathcal{J}_{ij}) \sim \exp\left[-\mathcal{J}_{ij}^2/(2\mathcal{J}^2)\right]$.

We describe a stroboscopic strategy to simulate the dynamics driven by such a Hamiltonian. For an arbitrary SY Hamiltonian, we can separate it into two parts $\hat{H}_{\rm SY} = \hat{H}_{\rm SY}^{(+)} + \hat{H}_{\rm SY}^{(-)}$, where $\hat{H}_{\rm SY}^{(+)}$ ($\hat{H}_{\rm SY}^{(-)}$) contains only all terms with positive (negative) con-

nections and thus can be realized efficiently in our platform. To realize a coarse-grained unitary evolution in a single time step Δt, we first turn on the positive Hamiltonian $\hat{H}_{\rm SY}^{(+)}$ for a time period of $\Delta t/2$. Then, we switch on the $\hat{H}_{\rm SY}^{(-)}$ for the same period and keep the Hamiltonian for another Δt. At last, we evolve the system again under $\hat{H}_{\rm SY}^{(+)}$ for $\Delta t/2$. The entire dynamics is then given by $\exp\left[-i\hat{H}_{\rm SY}\Delta t\right]+\mathcal{O}(\Delta t^3)$ with an error of the order Δt^3 due to the non-commuting $\hat{H}_{\rm SY}^{(+)}$ and $\hat{H}_{\rm SY}^{(-)}$.

We can also measure the out-of-time-operator-correlations for the SY model in our platform, which is essential for describing the entanglement scrambling in this system. The crucial step is creating a controlled GMM operation $\hat{U}_{C-\Lambda_\alpha}=|g\rangle\langle g|\otimes\hat{I}+|s\rangle\langle s|\otimes\hat{\Lambda}_\alpha$, which can be used to decompose an arbitrary SU(n) operator. Let us take a controlled symmetric GGM C-$\hat{\Lambda}_{\alpha\beta}^{(s)}$ as an example. To realize this kind of controlled operations, we can couple an ancilla qubit to the αth and the βth qubits in a single logical block with the two-body term $\hat{H}_{\alpha\beta}=\chi_\alpha\hat{\sigma}_{ss}^{(\mathcal{A})}\hat{\sigma}_+^{(\alpha)}+\chi_\beta\hat{\sigma}_{ss}^{(\mathcal{A})}\hat{\sigma}_+^{(\beta)}+h.c.$ This leads to an effective interaction $\tilde{\chi}_{\alpha\beta}\hat{\sigma}_{ss}^{(\mathcal{A})}\hat{\mathcal{T}}_{\alpha\beta}+h.c.$ within the gauge-invariant sector $\mathcal{Q}$, where $\tilde{\chi}_{\alpha\beta}=\chi_\alpha^*\chi_\beta/\lambda_G$ and λ_G is the coupling constant in gauge Hamiltonian $\hat{H}_G$ defined in Section 3.5. According to the definition of GGMs, if $\tilde{\chi}_{\alpha\beta}$ is real, the evolution under this Hamiltonian for an interaction time $t=\pi/2|\tilde{\chi}_{\alpha\beta}|$ yields $\hat{U}_{C-\Lambda_{\alpha\beta}^{(s)}}$. And if we set $\tilde{\chi}_{\alpha\beta}$ as pure imaginary, a controlled anti-symmetric GGM C-$\hat{\Lambda}_{\alpha\beta}^{(a)}$ would be realized.

We next describe a general method to construct and efficiently measure OTOCs for arbitrary SU(n) observables in this system driven by arbitrary Hamiltonian $\hat{H}_{\rm SY}$ without tomographic reconstruction. Unlike other protocols, our strategy is to encode the OTOC onto the single ancilla qubit $\mathcal{A}$ through controlled string operation and interferometrically read out the internal state of a *single* ancilla qubit. We consider two operators, $\hat{V}^{(i)}=\sum_\alpha v_\alpha^{(i)}\hat{\Lambda}_\alpha^{(i)}$ and $\hat{W}^{(j)}=\sum_\beta w_\beta^{(j)}\hat{\Lambda}_\beta^{(j)}$, acting on the system logical magnons and decomposed by the GGM operators $\{\hat{\Lambda}_\alpha^{(i)}\}$ and $\{\hat{\Lambda}_\beta^{(i)}\}$. The goal is then to measure all $C_{\alpha,\beta,\alpha',\beta'}\equiv\langle\hat{\Lambda}_{\beta'}^{(j)}(\tau)\hat{\Lambda}_{\alpha'}^{(i)}(0)\hat{\Lambda}_\beta^{(j)}(\tau)\hat{\Lambda}_\alpha^{(i)}(0)\rangle$ and construct the overall OTOC with weighted distribution $w_{\beta'}^*v_{\alpha'}^*w_\beta v_\alpha$. The circuit in Fig. 3.11(b) facilitates the transformation that maps the dynamical correlators $C_{\alpha,\beta,\alpha',\beta'}$ to the ancilla qubit with the initial system-ancilla state $|\psi(0)\rangle_{\mathcal{S}}\otimes|g\rangle_{\mathcal{A}}$. The ancilla atom can be physically represented by the atoms in close proximity to the impedance-matching tethers of PCWs, so that the internal spins of the ancilla atom can readily evanescently dissipate to the input and output couplers. The sequence of gate sets maps the initial state to $\hat{V}_{\alpha'}^{(i)}(0)\hat{W}_{\beta'}^{(j)}(\tau)|\psi(0)\rangle_{\mathcal{S}}|s\rangle_{\mathcal{A}}+\hat{W}_\beta^{(j)}(\tau)\hat{V}_\alpha^{(i)}(0)|\psi(0)\rangle_{\mathcal{S}}|g\rangle_{\mathcal{A}}$ with $\hat{O}(\tau)=e^{i\hat{H}\tau}\hat{O}e^{-i\hat{H}\tau}$. Here, the time-inverse evolution can be realized in a positive time flow but inverse the sign of all $\mathcal{J}_{ij}$. As with Ramsey interferometer, we measure the expectation values of the local spin vectors for qubit $\mathcal{A}$, where the dynamic correlators of the system atoms are $C_{\alpha,\beta,\alpha',\beta'}=\frac{1}{2}\left[\langle\hat{\sigma}_x\rangle_{\mathcal{A}}+i\langle\hat{\sigma}_y\rangle_{\mathcal{A}}\right]$. This method can be extended to

high-order dynamic correlations in a straightforward fashion.

3.10.4 Wess-Zumino-Witten quantum field theory

As a minimal SU(N) model, we discuss the realization of a stringly conformal field theory with an integrable 1D SU(3) Heisenberg model. Here, we investigate the universal features of the $\mathrm{SU}(3)_1$ Wess-Zumino-Witten (WZW) quantum field theory of level $k = 1$. In particular, we extract the conformal data by accessing the entanglement entropy for an 1D SU(3) Heisenberg model at the Ulmin-Lai-Sutherland (ULS) critical point, the parent Hamiltonian for generating a zoo of strongly-correlated ground states, such as those found in fractional quantum Hall systems. Because of the versatile programmability, the gauged waveguide QED simulator can be readily extended to the low-energy states of the 2D antiferromagnetic SU(n) model (Eq. 3.10), which are described by the (2+1)D WZW conformal field theory and holographically connected to a 3D Chern-Simons quantum gravity in the scaling limit.

Namely, we consider the realization of a (1+1)D $\mathrm{SU}(3)_1$ WZW CFT for the antiferromagnetic SU(3) Heisenberg model

$$\hat{H}_{\mathrm{WZW}} = \mathcal{J}_c \sum_{\bar{i}} \sum_{\alpha} \hat{\Lambda}_{\alpha}^{(\bar{i})} \hat{\Lambda}_{\alpha}^{(\bar{i}+1)}, \tag{3.21}$$

for the logical SU(3) spins on a ring within the sector of $\mathcal{Q} = n - 2$ of the waveguide QED simulator. Since $\mathcal{J}_c = -\mathcal{O}_{\bar{i},\bar{i}+1}^2/2\lambda_G < 0$, the vacuum state of the WZW CFT is encoded onto the most excited state of Eq. 3.21 within the sector $\mathcal{Q}$. This model has been extensively studied in the context of Haldane phase of the bilinear biquadratic (BBQ) spin-1 model

$$\hat{H}_{\mathrm{BBQ}} = \mathcal{J}_c \sum_{\bar{i}} \cos\theta \hat{\boldsymbol{S}}_{\bar{i}} \hat{\boldsymbol{S}}_{\bar{i}+1} + \sin\theta \left(\hat{\boldsymbol{S}}_{\bar{i}} \hat{\boldsymbol{S}}_{\bar{i}+1} \right)^2. \tag{3.22}$$

The enlarged SU(3) symmetry of Eq. 3.21 (Eq. 3.22 at $\theta_{\mathrm{ULS}} = \pi/4$) can be thought of as the consequence of the critical point of Berezinskii-Kosterlitz-Thouless (BKT) transition between the massive Haldane phase and an extended critical phase, described by the WZW field theory.

Enlarged SU(3)-symmetry of bilinear biquadratic spin-1 models

To understand the relationship between the familiar Haldane gap for spin-1 Heisenberg magnets at the exactly solvable point $\theta_{\mathrm{AKLT}} = \arctan(1/3)$ (AKLT valence bond state)

and the massless WZW field theory at $\theta_{\rm ULS} = \pi/4$ (See also Fig. 3.4(b)), we describe how the SU(3)-breaking marginal operator in the vicinity to the SU(3)-symmetric critical point $\theta_{\rm ULS}$ deforms the WZW CFT and dynamically generate a mass term in the Haldane phase by way of a BKT transition [111]. By moving into the fermionic parton picture defined in Section 3.6, the BBQ Hamiltonian can be mapped to

$$\hat{\mathcal{H}}^{\rm BBQ}_{\rm parton} = \hat{\mathcal{H}}_{\rm parton} + \epsilon^2 \hat{\mathcal{H}}_{\rm marginal}, \tag{3.23}$$

under the constraint $\sum_\alpha \hat{\psi}^{(\bar{i})\dagger}_\alpha \hat{\psi}^{(\bar{i})}_\alpha = 1$. The SU(3)-symmetric parton Hamiltonian $\hat{\mathcal{H}}_{\rm parton}$, defined in Eq. 3.11, is the dominant term near the ULS point, and kinetically exchanges excitations between the sites. The marginal operator $\hat{\mathcal{H}}_{\rm marginal} = \mathcal{J} \sum_{\bar{i}} \hat{\psi}^{(\bar{i})\dagger}_\alpha \hat{\psi}^{(\bar{i})}_\beta \hat{\psi}^{(\bar{i}+1)\dagger}_\alpha \hat{\psi}^{(\bar{i}+1)}_\beta$, proportional to $\epsilon^2 = \tan\theta - 1$, projects the neighbouring sites to the singlet space, similar to the singlet projectors of the AKLT Hamiltonian.

By applying the Hubbard-Stratotonovich transformation to Eq. 3.23 at the ULS point $\theta_{\rm ULS}$, we obtain the mean-field Hamiltonian $\hat{H}_{\rm mf} = |\chi_{\bar{i},\bar{i}+1}|^2 + \mu_{\bar{i}}(\hat{\psi}^{(\bar{i})}_\alpha \hat{\psi}^{(\bar{i})}_\alpha - 1) - \chi_{\bar{i},\bar{i}+1} \hat{\psi}^{(\bar{i})\dagger}_\alpha \hat{\psi}^{(\bar{i}+1)}_\alpha + h.c$ with the auxiliary fields $\chi_{\bar{i},\bar{i}+1} = \langle \hat{\psi}^{(\bar{i})\dagger}_\beta \hat{\psi}^{(\bar{i}+1)}_\beta \rangle$ and the constraints expressed in terms of the chemical potential $\mu_{\bar{i}}$, with a Fermi sea filled up to the momentum $k_F = \pi/3$. Around this saddle point, the low-energy physics of Eq. 3.23 at $\theta_{\rm ULS}$ is described by $\hat{\psi}^{(\bar{i})\dagger}_\alpha = e^{ik_F x_{\bar{i}}} \hat{\psi}_{L,\alpha}(x_{\bar{i}}) + e^{-ik_F x_{\bar{i}}} \hat{\psi}_{R,\alpha}(x_{\bar{i}})$ with the chiral fermions $\hat{\psi}_{L,\alpha}(x), \hat{\psi}_{R,\alpha}(x)$ only populated at the Fermi points, and write Eq. 3.23 as

$$\begin{aligned} \hat{\mathcal{H}}(x) \simeq \pi v_F \int \; dx \; & \sum_{\alpha,\beta} (\hat{j}^{\alpha,\beta}_R \hat{j}^{\beta,\alpha}_R + \hat{j}^{\alpha,\beta}_L \hat{j}^{\beta,\alpha}_L) \\ & + \epsilon^2 (\hat{j}^{\alpha,\beta}_R \hat{j}^{\alpha,\beta}_R + \hat{j}^{\alpha,\beta}_L \hat{j}^{\alpha,\beta}_L), \end{aligned} \tag{3.24}$$

in terms of U(3)-currents $\hat{j}^{\alpha,\beta}_L (\hat{j}^{\alpha,\beta}_R) = \hat{\psi}^\dagger_{L,\alpha} \hat{\psi}_{L,\beta} (\hat{\psi}^\dagger_{R,\alpha} \hat{\psi}_{R,\beta})$ and Fermi velocity v_F.

For the first term (with a global U(3)=U(1)$\oplus$SU(3) symmetry), a U(1) charge gap opens and leaves the SU(3)-symmetric WZW model $\hat{\mathcal{H}}_{\rm WZW}$ at the low-energy sector. Following the Abelian bosonization procedure $\hat{\psi}_{L,\alpha} =: 1/2\pi \exp(-i\sqrt{4\pi}\hat{\phi}_\alpha) :$ of Ref. [111], the SU(3)-symmetric continuum Hamiltonian reads

$$\hat{\mathcal{H}}_{\rm WZW} \sim \int dx (\partial\phi_1 \partial\phi_1 + \partial\phi_2 \partial\phi_2 + \text{a.h}) \tag{3.25}$$

with two compact SU(3) boson fields $\phi_{1,2}$ (each with central charge $c = 1$). Fig. 3.4(a) depicts the CFT scaling behaviour of entanglement entropy following the Calabrese-Cardy formula for different system size N_L ($c = 2.05 \pm 0.03$). The entanglement entropy is computed by system-size expansion of finite matrix product states (MPS) for logical spins

on a ring with a maximum bond dimension $\chi = 8000$. The finite MPS was optimized using a hybrid complex-time evolution algorithm (Section 3.10.4). Following the operator product expansion, it can be shown that $\langle \hat{S}_z^{(\bar{i})} \hat{S}_z^{(\bar{j})} \rangle_{\rm ULS} \sim \frac{\cos(2k_F|\bar{i}-\bar{j}|)}{|\bar{i}-\bar{j}|^{2\mathcal{D}}}$ with a scaling dimension $\mathcal{D} = 2/3$ [144]. Fig. 3.4(d) displays the correlation function obtained by optimizing uniform MPS with infinite DMRG algorithm truncated to $\chi = 500$, and the scaling dimension is fitted to $\mathcal{D} = 0.68 \pm 0.03$. The marginal perturbation of Eq. 3.24, on the other hand, breaks the global SU(3) symmetry of the ULS point, and a mass gap $m_\theta = \exp[-\gamma(\theta_{\rm ULS} - \theta)^{-0.6}]$ is dynamically generated for increasing coupling constant $\epsilon > 0$ ($\theta < \theta_{\rm ULS}$) with spin-spin correlation $\langle \hat{S}_z^{(\bar{i})} \hat{S}_z^{(\bar{j})} \rangle_\theta \sim \cos(2k_F|\bar{i} - \bar{j}|) e^{-m_\theta|\bar{i}-\bar{j}|}$ and non-universal constant γ. The asymptotic freedom of the marginal interaction at $\epsilon > 0$ can be thought of as a BKT phase transition in terms of the renormalization group flow [144]. The yellow line of Fig. 3.4(b) illustrates the scaling behavior of the correlation length $\eta_c \sim 1/m_\theta$ in comparison to those obtained from uniform MPS, where the non-universal constant γ is fitted to the data points. The maximum correlation length $\xi_c \simeq 40$ at the ULS point is artificially cut off due to the finite $\chi = 500$ truncation to the uniform MPS.

Hybrid complex-time algorithm

Because the vacuum state of WZW CFT corresponds to the most excited state within the low-energy sector $\mathcal{Q}$, standard DMRG algorithms cannot be adequately adapted to access the ground state of the target Hamiltonians (See also the inset of Fig. 3.4(a)). We instead apply a hybrid complex-time evolution to a random MPS in order to relax the system to the most excited state (target ground state) within the ground-state sector of the simulator by way of a time-evolving block decimation (TEBD) algorithm on the modified Hamiltonian

$$\hat{H} = \sum_{\bar{i},\bar{j}} (\hat{\mathcal{O}}_{\bar{i},\bar{j}} + \hat{D}_{\bar{i},\bar{j}}) + i\hat{H}_G, \tag{3.26}$$

where the definitions of $\hat{\mathcal{O}}_{\bar{i},\bar{j}}, \hat{D}_{\bar{i},\bar{j}}, \hat{H}_G$ in Section 3.5. The imaginary constraint $\hat{H}_G$ allows the cooling of the random MPS to the sector $\mathcal{Q}$, while the first term mediates the gauge-invariant ring-exchange Hamiltonian (Eq. 3.19) with an imaginary $\hat{J}_{\bar{i},\bar{j}} = i\mathcal{O}^2_{\bar{i},\bar{j}}/2\lambda_G$, which heats the system to the most excited state of the low-energy sector $\mathcal{Q}$.

Following the complex-time evolution, an isometric matrix product projector (MPO) is locally contracted with the time-evolved MPS to map the physical SU(2) spins to the logical SU(3) spins. While the isometric tensor is not necessary to the protocol, we have found that such a practice allows a more intuitive interpretation on the operations taking place in the logical degrees of freedom. In particular, the converted MPS obtained through this method coincides to that obtained by performing a finite DMRG on the logical WZW

Hamiltonian in Eq. 3.21. Fig. 3.13 displays the energy relaxation for the hybrid algorithm (solid line), which prepares the vacuum state of the WZW CFT (dashed line).

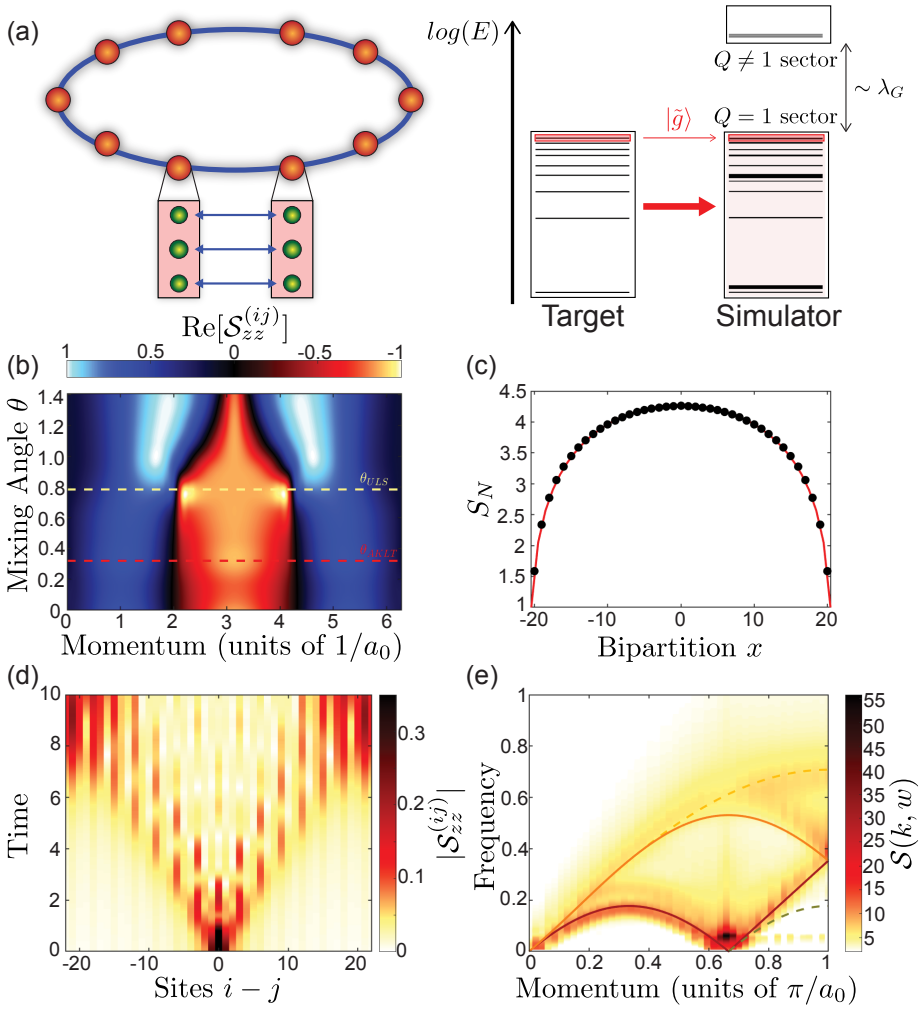

Figure 3.4: Emergence of Wess-Zumino-Witten (WZW) conformal field theories (CFT). (a) Local Hamiltonian encoding of $\mathrm{SU}(3)_{k=1}$ field theories on a ring onto SU(2) waveguide QED simulator. The target WZW CFT is isometrically transformed to the local Hilbert space of the simulator with electric charge $Q = 1$. (b) Phase diagram of the bilinear biquadratic spin-1 model with $N_{\text{eff}} = 42$ logical blocks ($N = 124$ atoms). Pinch points of static structure factor $\mathcal{S}^k_{zz} = \langle S^k_z S^{-k}_z \rangle$ at momentum $k = 2\pi/3, 4\pi/3$ signify the existence of divergent correlations at the Uimin-Lai-Sutherland (ULS) quantum critical point (QCP). The static structure factor is obtained from the correlation functions in 3.10.4 with uniform matrix product states (MPS) in the thermodynamic limit. (c) Critical scaling for entanglement entropy for vacuum state of (1+1)D $\mathrm{SU}(3)_k$ WZW field theory of level $k = 1$. The vacuum entanglement entropy follows the Calabrese-Cardy formula for (1+1)D conformal field theories (CFT). The central charge $c = 2.05 \pm 0.03$ is extracted from the finite-size scaling. (d) Production of $c = 2$ primary fields (quasiparticles) upon local quenching. Topological solitons carry fractional quantum statistics of Abelian anyonic phase $\phi = 2\pi/3$. (e) Dynamical probes for quasiparticles of the WZW CFT. Ground states are obtained with a hybrid DMRG-TEBD algorithm for finite MPS in a complex-time coordinate (3.10.4). Dynamical structure factor is obtained by real-time evolving the ground state MPS with a TEBD algorithm.

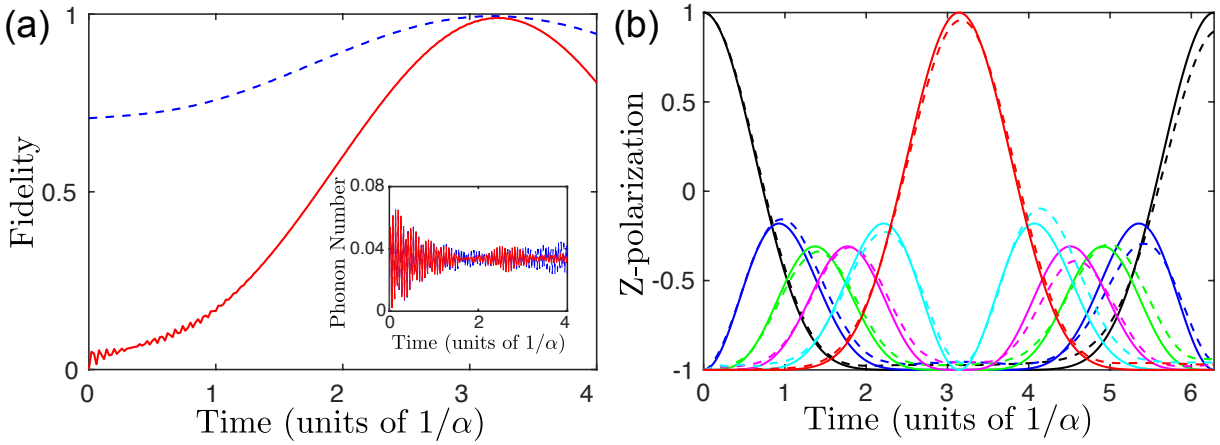

Figure 3.5: Quantum-state transfer over a spin chain. (a) Fidelity between the real-time state on the last spin and the initial state on the first spin for two input states $|\psi_{\rm in}^{(1)}\rangle = (|g\rangle - |s\rangle)/\sqrt{2}$ (red line) and $|\psi_{\rm in}^{(2)}\rangle = |s\rangle$ (blue dashed line). Inset is the mean number of phonons with a maximum value about 0.06, which shows that phonon is rarely populated in the whole process and validates the adiabatic elimination of phonons. The dynamics is numerically simulated for the full Hamiltonian, which includes the interactions of the atomic internal states, phonons, and electromagnetic vacuum. Close-to-unit fidelity $F = 0.994$ is achieved over time scale $t_f \simeq \pi/\alpha$. (b) Real-time dynamics of spin polarization $\langle\hat{\sigma}_z\rangle$ for all sites on the chain. The dashed (solid) line is obtained from the full (effective) Hamiltonian (in Eq. 3.12)

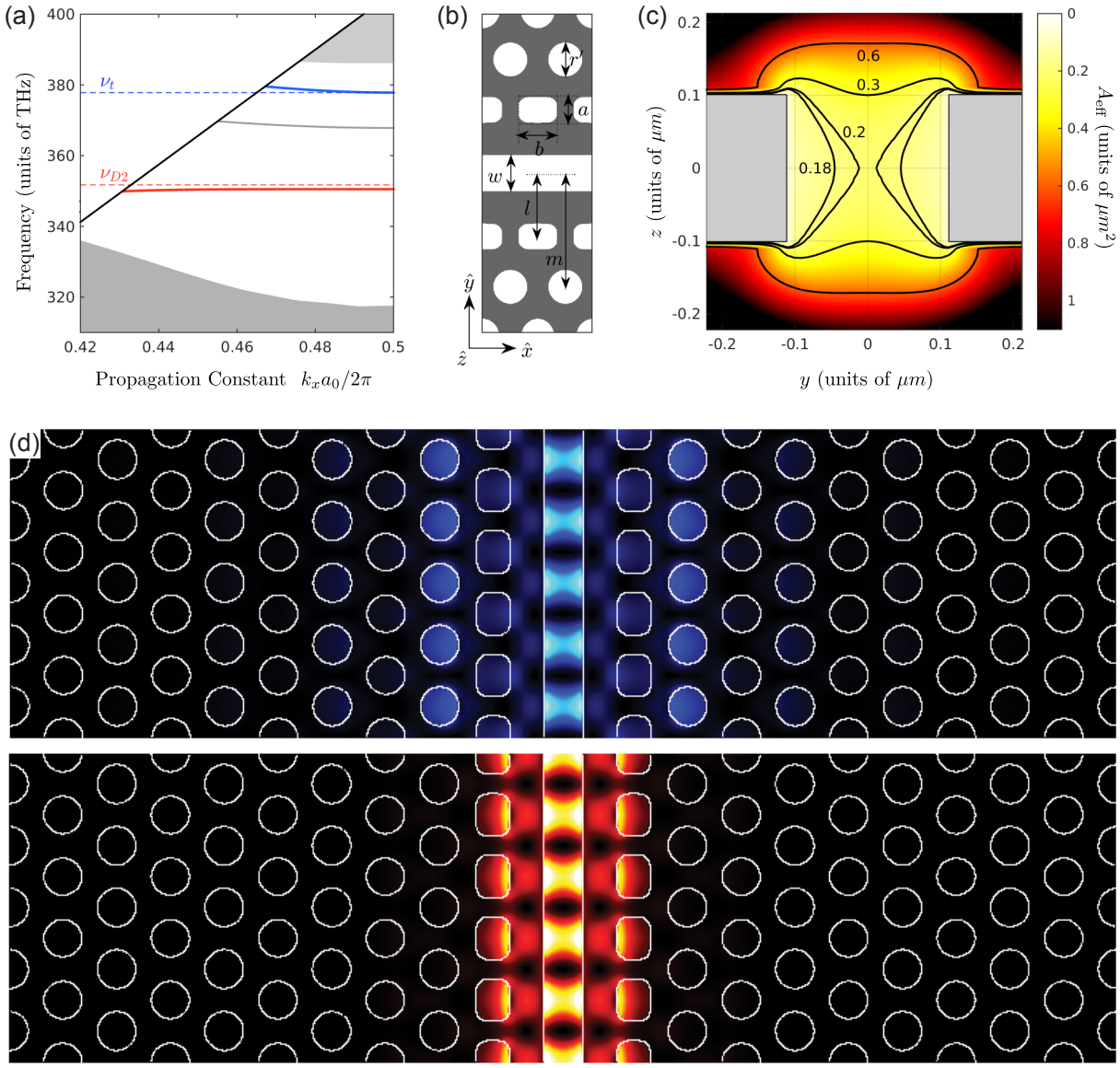

Figure 3.6: Slotted squircle photonic crystal waveguide. (a) SPCW band diagram. The guided modes are depicted as solid lines for both the excitation ν_{D2} (red) and trapping modes ν_t (blue). Through our optimization iterations, the guided modes (GM) ν_{D2}, ν_t are flattened around the Cesium D_2-transition and magic-wavelength trapping frequencies. GM ν_t is defined to operate at the blue-detuned magic wavelength condition for the D_2-transition at $\lambda_t = 793.5$ nm. The grey shaded region indicates the presence of slab modes. (b) SPCW geometry. The parameters that define the SPCW structure is provided in Table 3.1. (c) Effective mode area A_{eff}. We depict the x-cut contour map of A_{eff} for GM ν_{D2}. At the trapping region, we anticipate sub-wavelength localization $A_{\text{eff}}/\lambda_{D2}^2 \simeq 0.18$ and effective coupling rate $g_c \simeq 11.5$ GHz. The resulting photonic Lamb shift and localization length are $\Delta_{1\text{D}} \simeq 620$ MHz and $L_c \simeq 0.77$ μm at $\Delta_e = 0.4$ THz. (d) Contour intensity map of the guided modes ν_{D2}, ν_t.

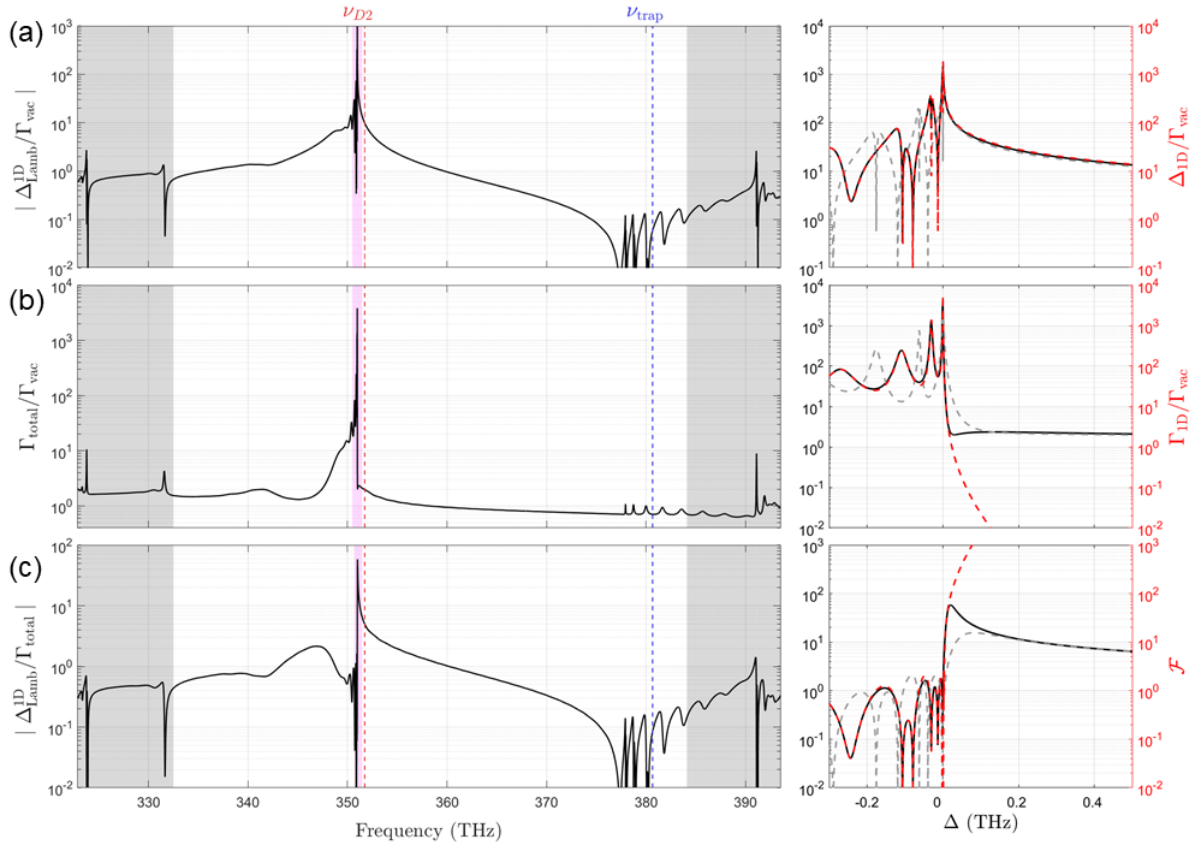

Figure 3.7: Collective atomic decay and photonic Lamb shift of a finite SPCW. (a) Photonic Lamb shift $\Delta^{1D}_{\mathrm{Lamb}}$ for electronically excited states. The energy shift Δ_{1D} of the excited state $|6P_{3/2}, F = 4\rangle$ of Cs is computed by the numerically evaluating the local scattering Green's function $\boldsymbol{G}_s(\boldsymbol{x}, \boldsymbol{x}', \omega)$. We only consider the level shift caused by the SPCW structure, but not the absolute renormalization by the electromagnetic vacuum. As a benchmark, we normalized the Lamb shift by the free-space decay rate Γ_{vac}. We also display the photonic Lamb shift Δ_{1D} under the single-band approximation as red dashed line. The close agreement between the two models testify the accuracy of the extrapolated Γ_{1D}. (b) The enhancement and inhibition of spontaneous emission in dispersive and reactive regimes. The total decay rate Γ_{total} is strongly enhanced at the band edge, and is exponentially inhibited in the band gap with $\Gamma_{\mathrm{total}} \simeq \Gamma_{1D} \exp(-L_d/L_c)$, where Γ_{1D} is the enhanced decay rate at the resonance closest to the band edge, $L_d = 80a_0$ is the device length for lattice constant a_0, and L_c is the localization length. Deep into the band gap $\Delta_e \gg 0$, the reduction of Γ_{total} is limited by the weakly inhibited homogeneous decay rate $\Gamma' \simeq 0.7\Gamma_{\mathrm{vac}}$ that predominantly emits photons out of plane of the slab. (c) Lamb shift to decay rate ratio $\Delta_{1D}/\Gamma_{\mathrm{total}}$ across a wide detuning range up to $\Delta_e \simeq 10$ THz. Inset. Figure of merit $\mathcal{F} \gg 1$ (red dashed line). The grey shaded region indicates the presence of slab modes.

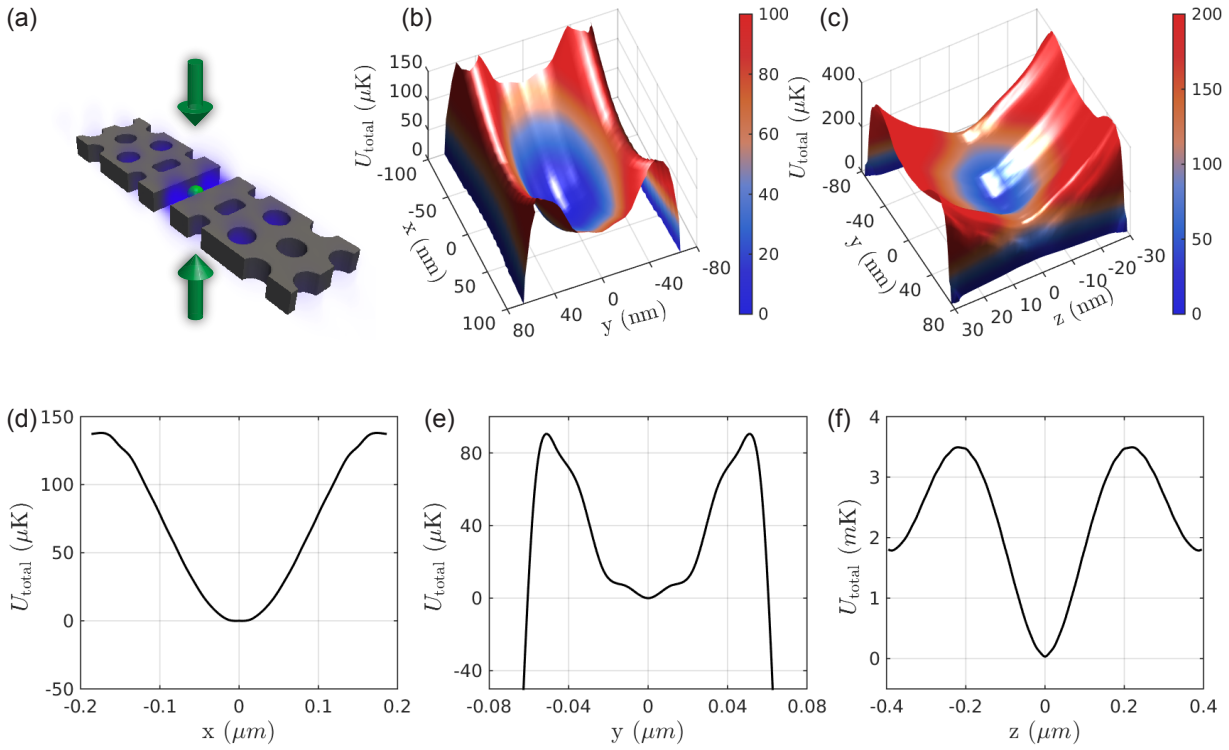

Figure 3.8: Adiabatic ground-state potentials for Cesium atom assisted by side-illumination beams. Cesium trapping potentials of $|6S_{1/2}\rangle$ for (b) $x-y$ plane and (c) $y-z$ plane with (d) the x-, (e) y-, and (f) z-slices. We assume that the refractive index n is frequency-independent. The coordination system (x, y, z) of the SPCW is defined in Fig. 3.6(b).

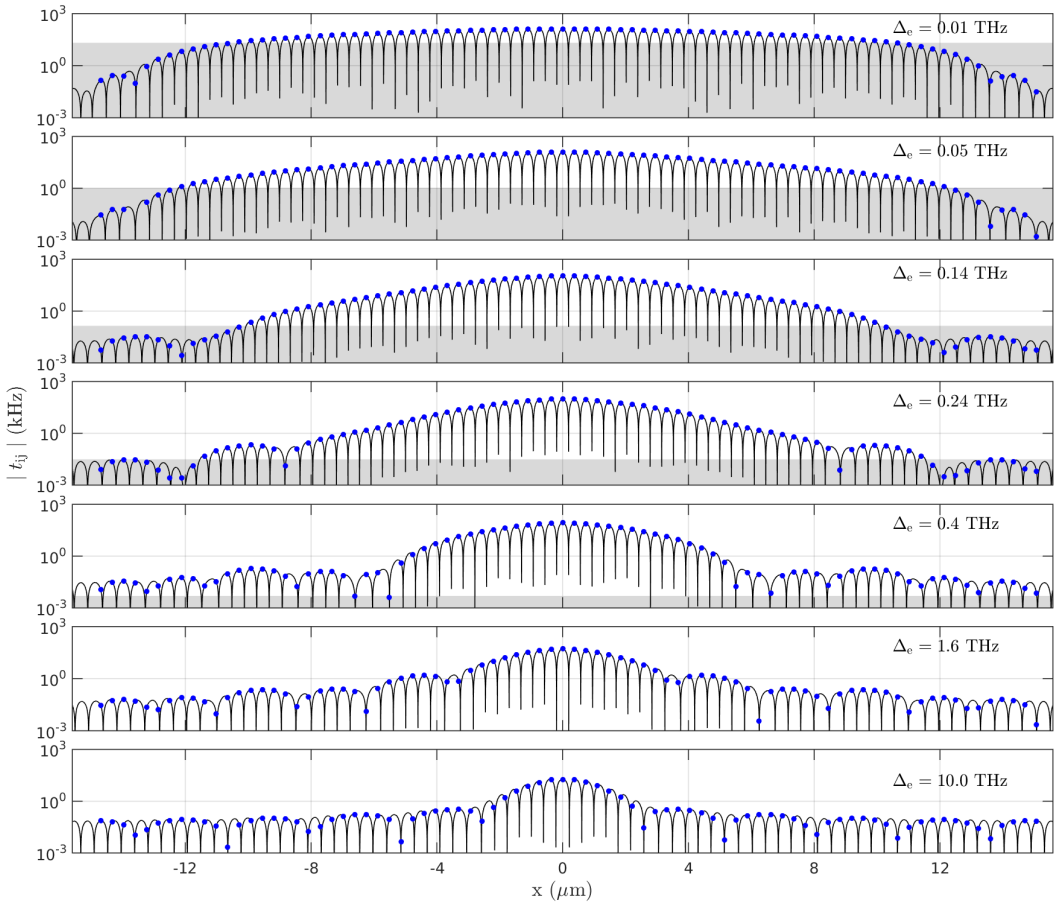

Figure 3.9: Short-ranged atom-atom interaction in a photonic band gap. We numerically evaluate the non-local Green's function $\boldsymbol{G}(\boldsymbol{x}_i, \boldsymbol{x}_j, w)$ for the SPCW and obtain the figure of merit for effective detunings $\Delta_e = 0.01, 0.05, 0.14, 0.24, 0.4, 1.6, 10$ THz. Due to the large photon mass m_e, the atoms experience exponentially localized tunneling interactions $t_{ij}/\gamma_m \gg 1$ over lengths L_c. The grey shaded regions depict the dissipative regime with $t_{ij} < \gamma_m$, where collective phononic loss dominates over the coherent tunneling rate. For large Δ_e, the ratio $t_{ij}/\gamma_m \gg 10^4$ is exponentially enhanced at the expense of reduced values $t_{ij} \simeq 2\pi \times 20$ kHz and localized length $L_c \simeq 2.5a_0$ at $\Delta_e \simeq 10$ THz.

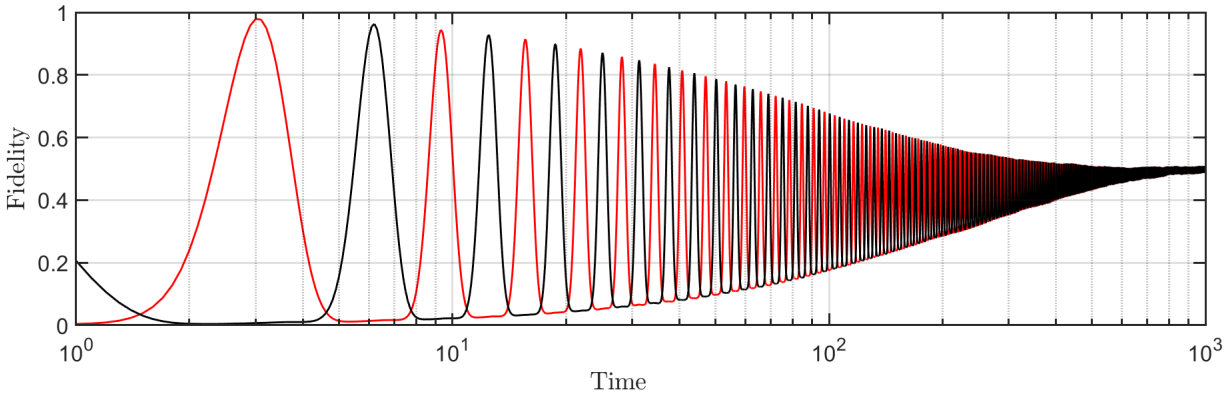

Figure 3.10: Quantum-state transfer over a dissipative spin chain. The open-system dynamics is numerically computed for the quantum-state transfer across $N = 6$ atoms with figure of merit $\mathcal{F} \simeq 10^4$ by the quantum trajectory method. In addition to the intrinsic mechanical dissipation, we include spin-relaxation processes in the far-off-resonant optical trap. The state fidelity of the first (last) atom in the spin chain is displayed as a black (red) line.

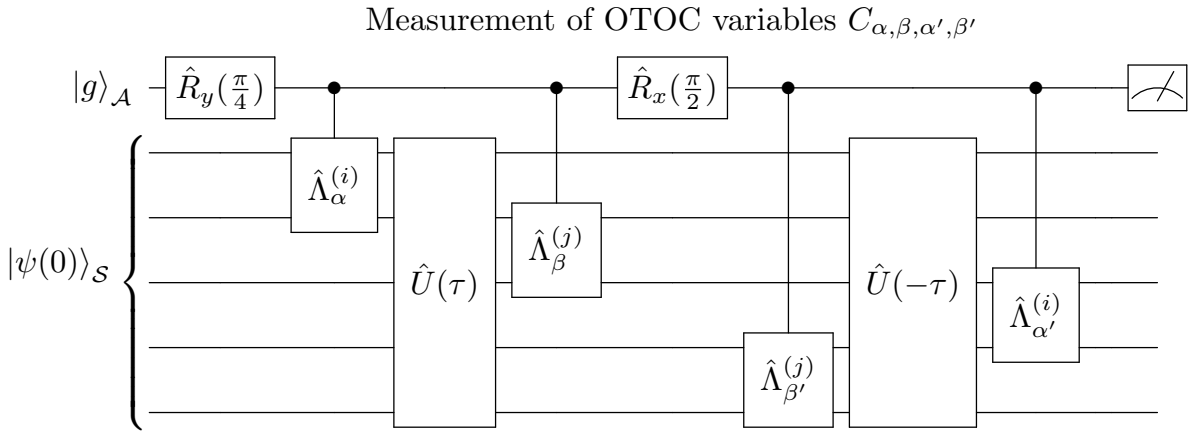

Figure 3.11: Construction of SU(n) OTOCs. Measurement prescription of highly complex out-of-time-order correlators (OTOC). The circuit constructs the OTOC variables $C_{\alpha,\beta,\alpha',\beta'} \equiv \langle \hat{\Lambda}_{\beta'}^{(j)}(t)\hat{\Lambda}_{\alpha'}^{(i)}(0)\hat{\Lambda}_{\beta}^{(j)}(t)\hat{\Lambda}_{\alpha}^{(i)}(0)\rangle$ of system atoms $\mathcal{S}$ and maps the values to the internal state of a single ancilla qubit $\mathcal{A}$. The time-inverse evolution for the global dynamics $\hat{U}(-\tau) = e^{-i(-\hat{H}_{\rm SY})\tau}$ can be realized still in a positive time flow but with a negative Hamiltonian $-\hat{H}_{\rm SY}$, i.e., inverting the sign of all $\mathcal{J}_{ij}$.

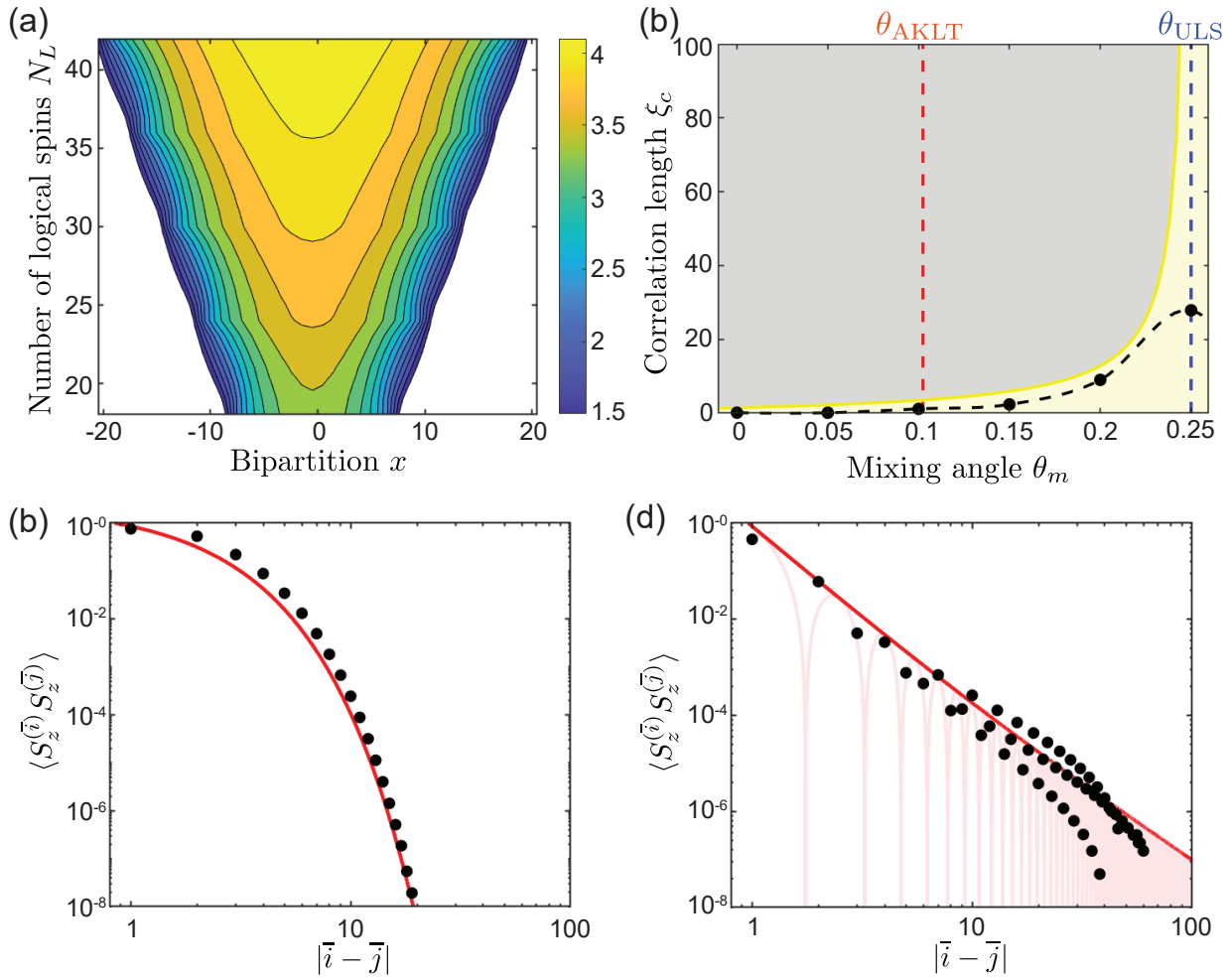

Figure 3.12: Bilinear biquadratic spin-1 model. (a) CFT scaling of entanglement entropy at the Uimin-Lai-Sutherland (ULS) point $\theta_{\rm ULS} = \pi/4$. (b) Quantum phase transition between gapped Haldane phase and gapless nematic phase at the ULS quantum critical point. (c) Spin-spin correlation function $\langle \hat{S}_z^{(\bar{i})} \hat{S}_z^{(\bar{j})} \rangle$ at the Affleck-Lieb-Kennedy-Tasaki (AKLT) point $\theta_{\rm AKLT} = \arctan(1/3)$ with a valence-bond ground state. (d) Spin-spin correlation function $\langle \hat{S}_z^{(\bar{i})} \hat{S}_z^{(\bar{j})} \rangle$ at the ULS point $\theta_{\rm ULS} = \pi/4$. The correlation functions and the phase diagram are computed from the uniform matrix product states (MPS), optimized by infinite DMRG algorithm with truncated bond dimension up to $\chi = 500$. Finite χ generates an artificial cutoff in the correlation length ξ_c to the otherwise algebraic correlation function. The fitting thereby only takes $|\bar{i} - \bar{j}| < \xi_c \simeq 40$ as the input. The entanglement entropy is simulated from a finite MPS for the logical SU(3) spins (3 physical spins per logical spin) on a ring with bond dimension up to $\chi = 8000$.

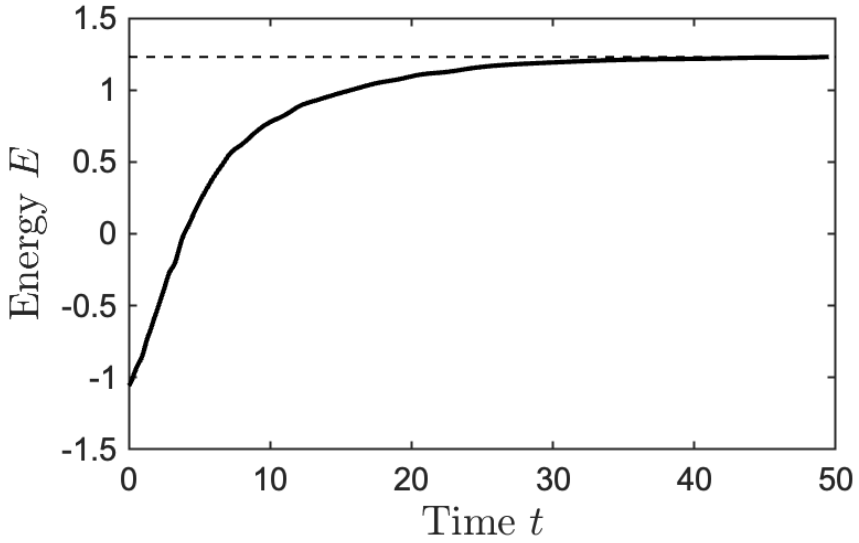

Figure 3.13: Complex-time matrix-product state evolution. Random matrix product state (MPS) is initially prepared for 54 physical spins ($N_L = 18$ logical spins), and the MPS is evolved under complex-time coordinate (Eq. 3.26) by way of time-evolving block decimation (TEBD) algorithm with an open boundary condition. At each time step, the SU(2) MPS of the physical spins is transformed to the SU(3) MPS for the logical spins by locally contracting the SU(2) MPS with an isometric matrix product operator (MPO) that projects the physical spins to the low-energy sector $\mathcal{Q}$. The overall dynamics is described by a cooling (heating) to (within) the ground state sector $\mathcal{Q}$, corresponding to the preparation of the vacuum state of the WZW CFT. The dashed line indicates the DMRG ground-state energy obtained for the target WZW Hamiltonian. The maximum bond dimension is $\chi = 200$.

Chapter 4

Quantum phases of strongly-coupled many-body QED in reactive regime

4.1 Summary

This chapter is largely based on the preprint [2]. My role in this work consisted of performing the numerical work and discussing its implications.

The quantum spin liquid was first proposed in 1973 as the ground state of an antiferromagnetic hexagonal lattice [145]. It was formulated as a "resonant valence bond" (RVB) state, which is a superposition of exponentially many valence bond states (states comprised of a series of tensor producted singlets). It wasn't until Kitaev that critical insights into spin liquids and their usefulness were uncovered with his toric code [146].

The toric code is the quintessential example of a spin liquid, displaying many of the critical features that make them so interesting. The toric code has 4 degenerate ground states that are topologically protected. The ground states are gapped and only a macroscopic operator which scales like the system size can perform transitions from one ground state to the other. The gap works to suppress errors in the form of quasi-particles [146]. This topological protection makes the toric code an incredibly error-resistant form of quantum memory [146, 147]. In particular by utilizing these topologically degenerate ground states as your computational basis.

When they do form, excitations take the form of anyons with fractional spin that are created in pairs. These two anyons could travel together and then annihilate each other, creating a loop in their path. If the loop is topologically trivial it does not affect the information stored in the logical basis [146]. Otherwise, it will have an impact on the data stored in the logical basis. For quantum memory, this is not desired. However, for

performing computation, this is exciting. By moving anyons together in a way that forms topologically non-trivial loops, you can perform operations on their computational basis.

The question then arises does there exist quasi-particles that through braiding would enable universal quantum computation [148]? The toric code's quasiparticles are not sufficient for universal quantum computation[149], however, it did inspire a search for other so-called non-abelian anyons that would be. An example of such a search is that into Majorana Fermions [150].

The toric code result is that of a Z2 spin liquid, and the Hamiltonian utilized by it is very difficult. It consists of 4 body terms, which are hard to create as nature tends to act with 2 bodies. It is only recently that Google managed to implement it experimentally by "brute forcing" it with repeated gates applications [151]. The creation and analysis of spin liquids continues to garner significant interest [145]. Some other experimental proposals for spin liquids is that of a Z2 spin liquid in a kagome lattice, for which there have been several AMO and material proposals for its generation and detection [152–154]. This is especially true when using cold atoms like trapped ions or Rydberg atoms. For instance, a recent Harvard paper using a ruby lattice (which is the dual of the kagome lattice) has even achieved positive identification of a spin liquid. [155]

What this section will do is provide an investigation into a many-body QED platform model that is experimentally relevant. This model will be shown to allow the stabilization of a Z2 spin liquid and potentially a never-before realized QED3 spin liquid. The model works by combining QED fluctuations with Rydberg interaction induced local U(1) gauge constraints. Numerous exotic phases were found, including a superradiant phase, valence-bond crystals, and topological and conformal phases. Most interestingly, we find signatures of a deconfined spin liquid described by a QED3 CFT. In this work, the numerics were used to support the existence of these phases. This ranges from obtaining operational metrics for topological and CFT entanglement entropy, decay of correlation functions, and the scaling behaviour of Wilsonian loops in both the deconfined and confined phases. Furthermore, we have constructed the modular matrices that encode the full braiding statistics of the anyons in the Z2 spin liquid phase.

The novel contributions within this section are as follows:

- We provide the first experimental proposal for stabilizing spin liquid states.
- This is the first application of many-body QED in reactive limit.
- We provide a new experimentally viable method of positively detecting spin liquid states.

Understanding and creating novel forms of light-matter quantum systems stimulates broad and fundamental insights in quantum information science. Remarkably, complex physical processes can arise as an emergent phenomena from an interacting network of light and matter. Here, we introduce a new class of strong-coupling quantum optics, where coherent atom-cavity dynamics is intertwined with the internal constraints imposed on the quantum material. We develop a conceptual paradigm of many-body quantum electrodynamics (QED), for which exotic quantum phases can be stabilized for a Rydberg ice when reactively coupled to the QED vacuum of the cavity field. We investigate how the cavity back-action induces a quantum melting of a Rydberg ice to topological and conformal spin liquids belonging to distinct superselection sectors. We discuss laboratory toolboxes for unambiguously detecting the spin liquid states and for probing their exotic quasiparticles with topological string operators, uncertainty-based entanglement witness, and cavity photon statistics. The quest to explore the surprising phenomena of light and matter awaits the arrival of many-body QED, where interacting matter and light are put on equal footing at the level of individual quanta.

4.2 Introduction

Much of the phenomena in atomic, molecular, optical and condensed matter physics are described by the interaction between light and matter [156–159]. Often, the behaviours of such dynamical systems are captured by system-size expansion of the light-matter coupling constant g_c. Cavity quantum electrodynamics (QED) offers a paradigmatic framework for non-perturbative dynamics of open quantum systems as a parent model for a broad range of light-matter quantum systems [58, 59, 61, 62, 132, 160–206]. In the strong coupling regime, the statistical description of its system dynamics can no longer be captured by a small-parameter fluctuation δn around a mean field $n_c \to 0$ [207–209]. As the scaling parameter n_c required to exert non-trivial dynamics vanishes in the face of dissipation, the observable system evolution becomes intricately dependent on the dynamical fluctuation δn at the level of individual quanta [165, 166].

As a scaling parameter of cavity QED, the critical atom (photon) number $n_c^{(a)}$ ($n_c^{(\gamma)}$) describes the characteristic number of atoms (photons) required to modify the entire atom-cavity level structure, initiating multiphoton processes for $n_c^{(\gamma)}, n_c^{(a)} \to 0$ [210]. However, in the presence of a macroscopic number of background atomic (photonic) excitations $N_a(N_\gamma) \gg 1$, the radiative dynamics of strongly-coupled cavity QED and their generalized cousins is reduced to a "simple" mean-field description involving collective spin excitations (coherent states) with negligible fluctuations, limiting single-quanta-level optical nonlin-

earity only to a small $N_a(N_\gamma)$ [167, 211]. Indeed, the ranges of cavity-mediated interactions with few modes are nearly divergent, and the effects of quantum fluctuation are suppressed by a large N-expansion of a classical background field [212]. Thus, the overall "scale" of quantum fluctuations and the achievable dynamical "complexity" of macroscopic light-matter quantum systems are generally restricted by their inverse system size $\sim 1/N$.

Here, we present a new regime of strong-coupling quantum optics, many-body QED, where short-ranged internal constraints Λ of a many-body quantum material compete with the long-range QED fluctuations of the cavity modes. Ubiquitous questions arising from the study of quantum matter breath new life in the domain of strong-coupling quantum optics. The general spirit of our work is that long-range cavity-mediated coupling can dramatically modify the spectral dimension and the universal properties that characterize the bare theory of the quantum material. In particular, we investigate how long-range QED vacuum can reactively melt a two-dimensional Rydberg ice [97, 213–222] to topological and conformal spin liquids [21, 145, 154, 223–228]. We describe laboratory toolboxes of many-body QED for the positive identification of spin liquid states with topological string operators and uncertainty-based entanglement witness, as well as powerful methods for probing and detecting anyons in the spin liquid with cavity photon statistics. Moreover, we investigate the entanglement response and low-energy spectra of the spin liquid with anyon flux insertion, and characterize the modular transformation of the topological and conformal sectors.

A crucial observation of our finding is that the long-wavelength description of reactive many-body QED bear essentially little similarity to the ground-state phase of the original material system, but neither do they retain the universal mean-field properties of the macroscopic cavity QED without a local gauge structure [212]. Instead, the frustration of the two competing long-range orders (infinite-range QED vacuum and local gauge symmetries) provides a powerful mechanism to disseminate quantum fluctuations and entanglement and to stabilize quantum orders heretofore not expected when the degrees of freedom for light and matter are taken separately. The present investigation supplements the recent experimental discovery of cavity spin liquids and quasiparticles in strongly-coupled many-body QED [229], and opens a new paradigm of quantum optics in the exploration of highly-entangled states, where dynamical complexities of light and matter fundamentally intertwine and enrich at scale.

Our general approach is to first begin with the expectations from collective atom-field Hamiltonians for non-interacting materials and then to build an understanding of locally gauging a reactive chequerboard-lattice cavity QED media under an ice constraint. After presenting the model in Section 4.4, we discuss the ground-state phase diagram for the many-body QED on a chequerboard lattice. In particular, we emphasize the principal role

of long-range QED fluctuations that promotes a Z_2 topological spin liquid as the ground state of U(1) lattice gauge theory coupled to Higgs scalar fields and speculate a "deconfined" quantum criticality between incompatible valence bond solid patterns in different charge sectors that stabilizes a conformal spin liquid state described by QED_3. We then provide the signatures that support the two flavours of spin liquids with the absence of long-range ordering for local operators and the low-energy transfer-matrix spectrum. Moreover, we unambiguously demonstrate the presence of the spin liquid states by calculating the universal corrections to the entanglement entropy in the long-wavelength limit and the modular transformation between the superselection sectors. We further classify the projective symmetry groups of the spin liquids by analyzing the responses of the entanglement entropy and the modular states transformed by a topological flux insertion.

Before proceeding, we caution that the ultimate goal of this work is to motivate further investigations of local gauging and non-local baths as the physical mechanisms for enriching complexities of light and matter. Moving beyond the reactive limit, our theoretical formalism only serves as a case study towards the daunting "spaghetti" regime of strongly-coupled many-body QED with a general local symmetry group $\mathcal{G}$ (Fig. 4.1). In this domain of strong coupling quantum optics, highly-entangled states can be born entirely from quantum fluctuations and "surprising" behaviour of light and matter can emerge from the dynamical frustration between global strong-coupling and local constraints beyond renormalization theories.

4.3 Many-body quantum electrodynamics

The model we consider can arise in a variety of contexts [178, 230, 231], but a crucial requirement for strongly-coupled many-body QED is that the local gauge constraints Λ_G dominate over atom-cavity coupling rate g_c in the single-quanta level strong coupling [197, 229], namely $\Lambda_G \gg g_c > \max(\kappa, \gamma)$. Thus, a natural host to explore many-body QED is a lattice of Rydberg atoms strongly coupled to an optical cavity [232, 233] and Rydberg ions coupled to their collective motions, where g_c (κ) is interpreted as the spin-motion coupling (heating) rate [230]. For the sake of concreteness, we consider the setting of Fig. 4.1, similar to the experiment [229], where a programmable tweezer array of neutral atoms [116–118, 234–240] is strongly coupled to a single-mode optical cavity and local Ising constraints are generated by Rydberg blockades [219, 221, 241–244].

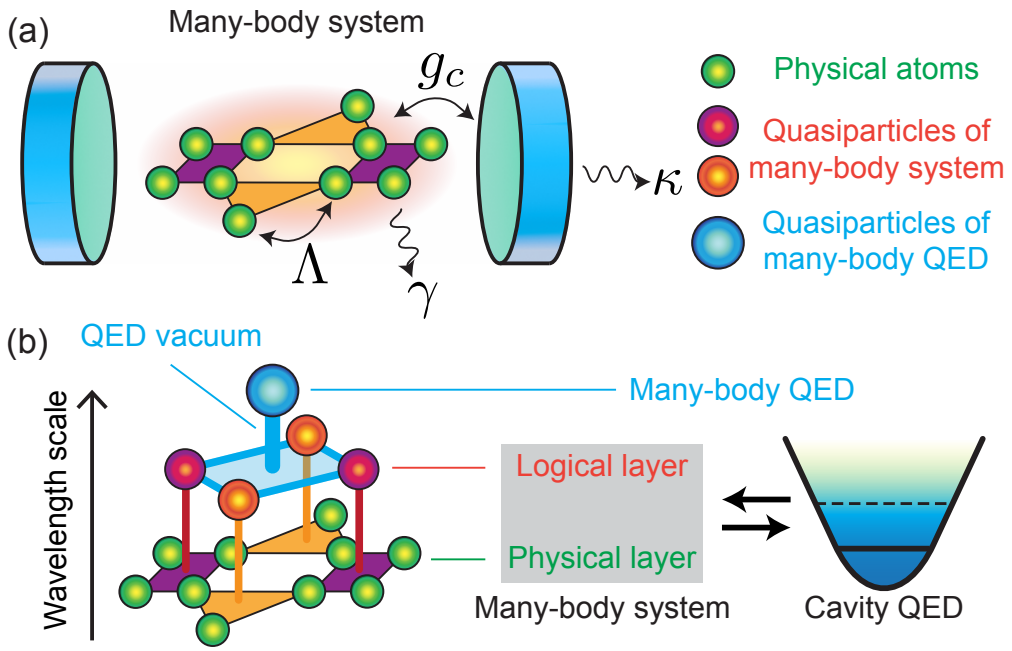

Figure 4.1: Strongly-coupled many-body quantum electrodynamics (QED) in the reactive limit. (a) Coupling a many-body system, characterized by local symmetry groups $\mathcal{G}$, to the QED vacuum of a general optical cavity. The characteristic interaction graph of the many-body system is represented by Λ. The many-body system is strongly coupled to the cavity with a single-atom vacuum Rabi splitting $g_c \gg (\kappa, \gamma)$, compared to the the cavity (κ) and atomic decay rates γ. Many-body QED is realized in the limit $\Lambda \gg g_c$, where coherent atom-field dynamics is constrained by the local symmetry sectors $\mathcal{G}$ of the many-body system. (b) Emergent degrees of freedom in many-body QED. Low-energy quasiparticles populate the local symmetry sectors $\mathcal{G}$ (logical layer) and dynamically couple to the vacuum of the cavity, enriching the background field of the many-body system to complex quantum dynamics in the reactive limit.

We thereby consider the constrained atom-cavity dynamics within some local symmetry sector $\mathcal{G}$ of the many-body (Rydberg) Hamiltonian $\hat{H}_G$ with the Liouvillian motion $\dot{\hat{\rho}} = i[\hat{H}_{\mathrm{mQED}}, \hat{\rho}] + \kappa \mathcal{D}_a[\hat{\rho}] + \gamma \mathcal{D}_\sigma[\hat{\rho}]$ and many-body QED Hamiltonian

$$\hat{H}_{\mathrm{mQED}} = \Delta_c \hat{a}^\dagger \hat{a} + \hat{H}_{\mathrm{cQED}} + \Lambda_G \hat{H}_G, \tag{4.1}$$

with cavity QED Hamiltonian $\hat{H}_{\mathrm{cQED}} = g_c(\hat{a} + \hat{a}^\dagger)\hat{S}_x$, dissipative superoperators $\mathcal{D}_{\mathcal{O}}[\hat{\rho}] = \hat{\mathcal{O}}\hat{\rho}\hat{\mathcal{O}}^\dagger - \{\hat{\mathcal{O}}^\dagger\hat{\mathcal{O}}, \hat{\rho}\}/2$ for the jump operators $\hat{\mathcal{O}} \in \{\hat{\sigma}_-^{(i)}, \hat{a}\}$ and collective spin operators $\hat{S}_\alpha = \sum_{i=1}^{N_a} \hat{\sigma}_\alpha^{(i)}$. With $\Lambda_G \gg g_c$, the local constraint $\hat{H}_G = \sum_{\blacksquare} (\hat{\mathcal{G}}_{\blacksquare} - \mathcal{Q})^2$ (e.g., Kitaev toric code [245]) acting on sites $\blacksquare$ restricts the many-body dynamics within a charge sector $\mathcal{Q}$ by the generator $\hat{\mathcal{G}}_{\blacksquare}$ of the Abelian gauge symmetry.

More generally, the many-body term $\hat{H}_G$ may include more complex terms that embed

non-Abelian gauge theories (e.g., Kitaev Honeycomb model [246]) with its own quasiparticles (e.g., Ising anyons) and dynamical gauge fields. The crucial philosophy here is that the quasiparticles of $\hat{H}_G$ necessarily couple to light fields and are renormalized by the cavity-mediated long-range interaction between the deconfined charges of the dynamical gauge theory (See the logical level of the coarse-graining procedure in Fig. 4.1b). It is conceivable that the cavity backaction on the anyons can impart and enrich the quantum dynamics with wholly emergent degrees of freedom heretofore not present in the original quantum matter $\hat{H}_G$ by way of the radiative coupling to the cavity baths. Moreover, on resonance $\Delta_c = 0$ ("spaghetti" regime), these new degrees of freedom incorporate radiative excitations of the cavity and strongly-coupled many-body QED necessarily involves the coherent interactions between light fields and the exotic quasiparticles.

To illustrate this, we adiabatically eliminate the cavity field in the reactive limit $\Lambda_G > \Delta_c \gg g_c$ and obtain the low-energy theory,

$$\begin{aligned} \hat{H}_{\text{mQED}} &= -\sum_{n=1}^{\infty} \hat{P}_{\mathcal{Q}} \left(\frac{\hat{H}_{\text{cQED}}(1-\hat{P}_{\mathcal{Q}})}{\Delta_c \hat{a}^\dagger \hat{a} + \Lambda_G \hat{H}_G} \right)^{n-1} \hat{H}_{\text{cQED}} \hat{P}_{\mathcal{Q}} \\ &\quad + \Delta_c \hat{a}^\dagger \hat{a} + \Lambda_G \hat{H}_G, \end{aligned} \tag{4.2}$$

where $\hat{P}_{\mathcal{Q}}$ projects the atom-cavity system into the vacuum sector $|0\rangle_c |\mathcal{Q}\rangle_{\blacksquare}$. As $\hat{H}_{\text{cQED}}$ creates gauge charges from $|0\rangle_c |\mathcal{Q}\rangle_{\blacksquare}$, gauge-invariant multi-particle quantum dynamics remains the only dominant process as the lowest order of the expansion in the first term of Eq. 4.2 after integrating out the cavity field. On the other hand, a single-mode cavity absent the constraint Δ_c can only generate a semi-classical flip-flop interaction $\sim -\frac{g_c^2}{\Delta_c} \hat{S}_+ \hat{S}_-$ with mean-field operators $\hat{S}_\pm = \sum_i^N \hat{\sigma}_\pm^{(i)}$ and stabilize a global spin singlet in the form of Dicke state

$$|G\rangle_{\text{cQED}} = |S = 0, S_z = 0\rangle, \tag{4.3}$$

as its ground state in the language of collective spin algebra.

To qualitatively see how $\hat{P}_{\mathcal{Q}}$ can promote and enhance quantum fluctuations in the system, let us consider how a four-particle dimerized state $|\square\rangle = |\text{-}_{1,3}\rangle \otimes |\text{-}_{2,4}\rangle$ with the singlet $|\text{-}_{i,j}\rangle = \frac{1}{\sqrt{2}}(|e_i g_j\rangle - |g_i e_j\rangle)$ is transformed under a projective constraint $\hat{P}_1^{(i,j)}$ that selects local components on sites $i, j \in \{1,2\}$ ($\{3,4\}$) with a single collective excitation. Qualitatively, $\hat{P}_1^{(i,j)}$ can be thought of as the action of Rydberg blockade acting on geometrically local sites $\{1,2\}$ ($\{3,4\}$), while cavity fields mediate geometrically long-range dimer bonds $|\text{-}_{i,j}\rangle$ between the remote sites $\{1,3\}$ ($\{2,4\}$). Here, the local projection with

appropriate normalization factor $\mathcal{N}$ produces a GHZ entangled state

$$\frac{1}{\sqrt{\mathcal{N}}}\hat{P}_1^{(1,2)}\hat{P}_1^{(3,4)}|\square\rangle = \frac{1}{\sqrt{2}}(|g_1e_2g_3e_4\rangle + |e_1g_2e_3g_4\rangle) \tag{4.4}$$

among the four spins. The key message is that the local symmetry imposed onto cavity-mediated long-range bonds (with a permutation symmetry) enhances the quantum fluctuation for the ground states stabilized by many-body QED.

Moreover, with tunable coupling $\hat{H}_{\text{cQED}}$ to multiple cavity modes [70, 198], universal QMA-complete Hamiltonian (programmable variant of Eq. 4.2) can be boostrapped from the flip-flop dynamics of $\hat{H}_{\text{cQED}}$ when projected by a local constraint [247]. Thus, the global spin singlets $|G\rangle_{\text{cQED}}$ prepared by long-range cavity-mediated Hamiltonian serve as a "resource substrate" on top of which long-range entanglement can emerge when the Hilbert space is restricted locally. As we will show, quantum phases simply generated from global interactions (e.g., $|G\rangle_{\text{cQED}}$) fundamentally differ from those under combinatorial constraints (global permutation symmetry and local gauge symmetry). The dynamical frustration between the global and local degrees of freedom can promote the stability of highly entangled phases that are not possible when only one of the conservation rules is allowed. In turn, a seemingly simple dissipative process (e.g., spontaneous emission) can have profound impact to the open-system evolution of the many-body state, when constrained by both the global (cavity) and local (Rydberg) symmetries [247]. The computational complexity of the light-matter quantum dynamics can be enriched exponentially by local projections of the many-body Hamiltonian [248]

We further remark that the general strategies of enriching complexity by local projections are also be found in the AKLT representation of tensor network states, parton theory of spin liquids, and the theories of universal Hamiltonian. In tensor network states, highly-complex multipartite entangled states are constructed from building blocks of disconnected dimer bonds between auxiliary particles by local gauging [249]. In the parton description, a classical parton wavefunction within an enlarged Hilbert space is promoted to long-range entangled spin liquids by a local Gützwillar projection that brings back the system to its physical Hilbert space [224, 250]. In addition, all static and dynamical properties of any local Hamiltonian can be universally emulated by the action of local gadgets acting on a long-range 2-local Hamiltonian in a larger Hilbert space [53, 251, 252].

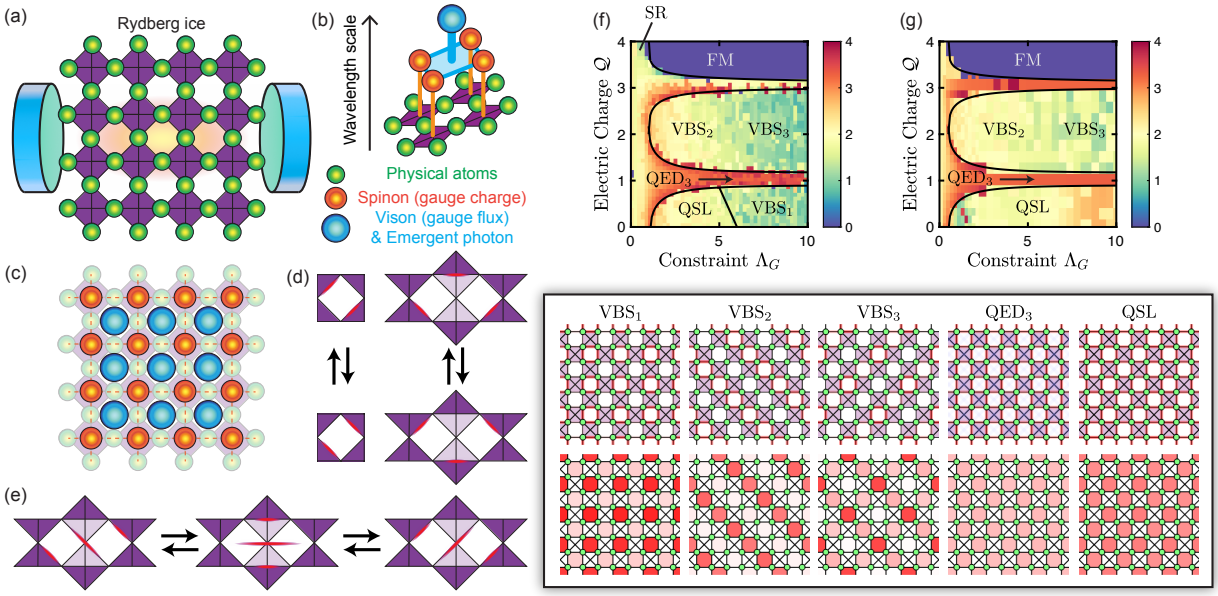

Figure 4.2: Quantum phases of reactive many-body QED in a chequerboard lattice. (a) Coupling a 2D Rydberg spin ice with a local $U(1)$ gauge symmetry to a multimode optical cavity in the reactive limit. Many-body states are locally constrained by an Ising-like Hamiltonian to the gauge sector $\mathcal{Q}$ within the purple plaquettes, while quantum fluctuation is injected to the many-body system by way of cavity QED. (b) Coarse-graining procedure of many-body QED for stabilizing the vacuum state of topological and conformal field theories. In the long-wavelength limit, non-trivial quasiparticles (spinon, visons, and collective photon modes) emerge within different topological and conformal sectors. (c) Spinons and visons in the deconfined phase of $\mathbb{Z}_2$ lattice gauge theory. Spinon and vison are mutual semions with a non-trivial statistical phase $\theta_{sv} = \pi/2$. (d) Quantum dimer dynamics mediated by cavity QED vacuum bath. Quantum dynamics involving non-bipartite dimers are driven by long-range cavity-mediated interactions.

4.4 Cavity-assisted melting of a Rydberg ice

We now turn to the question of the possible quantum phases stabilized for the reactive many-body QED in Eq. 4.1 when a Rydberg ice is coupled to a single-mode cavity. We assume that the chequerboard lattice wrapped around an infinitely-long cylinder ($N_x \to \infty$) with a finite circumference N_y. The many-body QED Hamiltonian reads

$$\hat{H}_{\text{mQED}} = \Delta_c \hat{a}^\dagger \hat{a} + \hat{H}_{\text{cQED}} + \Lambda_G \hat{H}_{\text{ice}}, \tag{4.5}$$

$$\hat{H}_{\text{ice}} = \sum_{\boxtimes} (\hat{G}_{\boxtimes} - \mathcal{Q})^2, \tag{4.6}$$

with the generator $\hat{G}_{\boxtimes} = \sum_{i \in \boxtimes} \hat{\sigma}_z^{(i)}$ acting on the corner-sharing ice sites $i \in \boxtimes$, as shown in Fig. 4.2(a). The ice constraints can be generated on a chequerboard lattice Rydberg

tweezer array (Fig. 4.1(a)) by integrating out driven-dissipative dynamics of reservoir atoms [253].

Before we proceed to the discussion of the full phase diagram in the reactive limit, let us review some properties for the ground state $|G\rangle_{\mathrm{cQED}}$ of cavity QED with $\Lambda_G = 0$ from the perspective of dimer physics. The Dicke state $|G\rangle_{\mathrm{cQED}}$ possesses global symmetries $\hat{S}_z = 0$ and $\hat{S} = 0$ and their physical properties can be described by the macroscopic mean fields $\hat{S}$ and their descendants. The global singlet state $|G\rangle_{\mathrm{cQED}}$ is an example of an insulating and disordered state, similar to a quantum spin liquid.

From a dimer language, $|G\rangle_{\mathrm{cQED}}$ can be written as an "infinite-range" resonating valence bond (RVB) state, an equal-weight macroscopic superposition of fully-packed dimer configurations

$$|G\rangle_{\mathrm{cQED}} = \frac{1}{\sqrt{\mathcal{N}}} \sum_{\mathcal{C}\in \mathrm{all}} \prod_{i,j\in\mathcal{C}} |\text{-}_{i,j}\rangle \tag{4.7}$$

However, unlike short-ranged RVB states, the perfect filling of the dimers is not due to some local constraints that promote the pairing and regulate the dimer patterns. Indeed, the dimer movements of $|G\rangle_{\mathrm{cQED}}$ are not microscopically constrained (e.g., six or eight vertex models), and the unit filling is merely a consequence of the global quantum numbers $S = 0$ and $S_z = 0$. Thus, this ground state can be thought of as a liquid-like superradiant (SR) phase characterized at the level of classical mean field theory by the all-to-all permutation symmetry of the cavity field and a well-defined global phase with maximal fluctuations of the dimer number, similar to a superfluid.

While $|G\rangle_{\mathrm{cQED}}$ is a trivial disordered state, it serves as a useful background field template for many-body QED to construct more complex quantum phases when infinite-range cavity-mediated dimer resonances are restricted to the local symmetry sector $\mathcal{Q}$. Qualitatively, with increasing order of Λ_G/g_c, the scale of quantum fluctuation is amplified across the system by local constraints, and the long-range entanglement survive as a universal property at the thermodynamic limit. In this setting, bona fide spin liquid states (short-ranged RVB state) may be born from manifestly quantum fluctuations (cavity QED vacuum), locally preserving an extensive ground-state entropy and acquiring a macroscopic quantum field theory description. Beyond directly accessing the elusive spin liquid states, many-body QED is a controlled laboratory platform to investigate the symmetry-broken phases that harbour the deconfined states by anyonic condensations for classifying the projected symmetry groups of the spin liquids in an experiment.

To illustrate this for the symmetry sector $\mathcal{Q} = 0$, we systematically derive the coarse-grained Liouvillian quantum plaquette dynamics up to the sixth order of $\mathcal{O}(g_c/\Lambda_G)$ [89] for a Rydberg ice reactively coupled to a zero-dimensional quantum bath of the single-mode

optical cavity. We obtain the projected master equation at the sixth order of Nakajima-Zwanzig projection operator formalism $\dot{\hat{\rho}}_{\mathcal{S}} = -i[\hat{H}_{\rm eff}, \hat{\rho}_{\mathcal{S}}] + \sum_k (\hat{c}_k^{\rm eff} \hat{\rho}_{\mathcal{S}} \hat{c}_k^{\rm eff\dagger} - \{\hat{\rho}_{\mathcal{S}}, \hat{c}_k^{\rm eff\dagger} \hat{c}_k^{\rm eff}\}/2)$. In the $\mathcal{Q} = 0$ sector, the relevant effective Hamiltonian and jump operators are (apart from the single-atom decay $\hat{c}_i = \sqrt{\gamma}\hat{\sigma}_-^{(i)}$)

$$\begin{aligned} \hat{H}_{\rm eff} &= -J_{\rm ring} \sum_{\square} \hat{W}_{\square}^{(ijkl)} - K_{\rm ring} \sum_{\hexagon} \hat{W}_{\hexagon}^{(ijklmn)} \\ &\quad + \Lambda_G \sum_{\boxtimes} \left(\sum_{i \in \boxtimes} \hat{\sigma}_z^{(i)} \right)^2 , \end{aligned} \tag{4.8}$$

with plaquette operators $\hat{W}_{\square}^{(ijkl)} = \hat{\sigma}_+^{(i)} \hat{\sigma}_-^{(j)} \hat{\sigma}_+^{(k)} \hat{\sigma}_-^{(l)} + h.c$ and $\hat{W}_{\hexagon}^{(ijklmn)} = \hat{\sigma}_+^{(i)} \hat{\sigma}_-^{(j)} \hat{\sigma}_+^{(k)} \hat{\sigma}_-^{(l)} \hat{\sigma}_+^{(m)} \hat{\sigma}_-^{(n)} + h.c$ and ring-exchange couplings $J_{\rm ring} = 4g_{\rm eff}^4/\Lambda_G(\Lambda_G + \Delta_c)^2$ and $K_{\rm ring} = 36 g_{\rm eff}^6/\Lambda_G(\Lambda_G + \Delta_c)^4$. The corresponding dimer resonances for $\hat{W}_{\square}^{(ijkl)}$ and $\hat{W}_{\hexagon}^{(ijklmn)}$ are illustrated in Figs. 4.1(d) and (e), respectively. Notably, the additional hexagonal dimer resonance $\hat{W}_{\hexagon}^{(ijklmn)}$ is driven by the "zero"-dimensional cavity baths and will play a crucial role in the stabilization of a topological spin liquid within the context of a U(1) lattice gauge theory.

In the reactive limit of strongly-coupled many-body QED, the system remains coherent with negligible dissipation. Different dissipative processes give rise to unique types of "errors" that create a pair of anyons in a topological spin liquid. System's spontaneous emission $\hat{c}_i$ ($\hat{c}_{\square}$) generates or annihilates a pair of spinons (visons). On the other hand, $\hat{c}_{\rm ring}$ is a source of inhomogeneous broadening for the visons. We only remark the expression for the correlated spin-flip decay $\hat{c}_2 = \sqrt{\kappa_2} \sum_{\square} \left(\sum_{i,j \in \square} \hat{\sigma}_x^{(i)} \hat{\sigma}_x^{(j)} \right)$, which lead to the production of photon pairs at the output mode of the cavity. $\hat{c}_2$ facilitates the time-resolved characterization of conditional response function of plaquette dynamics $\hat{W}_{\square}$ upon the production of vison pairs by monitoring the correlated photon pairs leaking through the cavity mode.

In the limiting case $\Lambda_G \to \infty$ ($K_{\rm ring} \to 0$), the ground state for $\mathcal{Q} = 0$ is the projected wavefunction of the Dicke state $|{\rm VBS}_1\rangle_{\rm mQED} = \frac{1}{\sqrt{\mathcal{N}}} \hat{P}_{Q=0} |G\rangle_{\rm cQED}$ and is described by a resonating plaquette "solid" phase. As shown in the inset of Fig. 4.2, the dimer and plaquette patterns of $|{\rm VBS}_1\rangle_{\rm mQED}$ depict a classical phase with a broken lattice translation symmetry (i.e., a crystalline phase of localizeable plaquettes $\square$ with $\langle \hat{W}_{\square} \rangle > 0$) in the so-called magnetic field basis. With negligible $K_{\rm ring}$, Eq. 4.8 corresponds to the lattice Hamiltonian of a pure frustrated compactified U(1) gauge theory, $(2+1)$D fcQED,

$$\hat{\mathcal{H}}_{\rm fcQED} = -2J_{\rm ring} \sum_{\boxdot} \cos(\nabla \times A_{\boxdot}) + \frac{U}{2} \sum_{\boxtimes} E_{\boxtimes}^2 \tag{4.9}$$

on a bipartite lattice (in this case, on the dual square lattice of Fig. 4.1(c)) with $U \gg J_{\rm ring}$ [145]. Here, we label the plaquettes $\boxtimes$ ($\boxdot$) as "star" ("flux") sites on the dual lattice

description of Fig. 4.1(c), where electric/spinon (magnetic/vison) excitations may exist respectively. The local quantum number $\mathcal{Q}$ of $\hat{H}_{\rm ice}$ is thereby interpreted as the electric gauge charge of QED. It is well-known that the celebrated Polyakov mechanism for (2+1)D QED [254] induces *confined* phase, in place of a *gapless* Coulomb spin liquid, by the proliferation of instantons. The condensation of those instantons in turn gaps out the artificial photon of the Coulomb phase and drives a symmetry breaking transition to a valence bond solid. In fact, the resonating plaquette solid state $|{\rm VBS}_1\rangle_{\rm mQED}$ is precisely the anticipated *confined* phase of the fcQED $\hat{\mathcal{H}}_{\rm fcQED}$ on the dual square lattice without a static charge $\mathcal{Q}=0$.

In the intermediate regime $\Lambda_G \gtrsim g_c$, the long-range dimer resonance $\hat{W}^{(ijklmn)}_{\hexagon}$ occurs within an hexagon of extended Kagome lattice that is embedded into the physical chequerboard lattice (See Fig. 4.1(d)-(e)). The existence of such cavity-mediated resonances, which breaks the bipartiteness of the geometric lattice, plays a crucial role in the enhanced stability of the *gapped* spin liquid state of U(1) lattice gauge theories. Indeed, the physical theory of many-body QED is not strictly defined on the two-dimensional lattice. Instead, it is a hybrid dimensional theory of a zero-dimensional quantum fluctuation progressively constrained with increasing order $\mathcal{O}(\Lambda_G/g_c)$ by the Hamiltonian graph $\hat{H}_{\rm ice}$ defined on a two-dimensional lattice, only recovering the two-spatial dimensional infrared fcQED limit when $\Lambda_G \to \infty$. Between the SR and VBS phases at $\mathcal{Q}=0$, the local constraint $\hat{H}_{\rm ice}$ is soft, and higher-order dimer resonances begin to involve the fluctuations of dimer pairs on the diagonal bonds (Fig. 4.1(d)-(e)). For example, for $\Lambda_G\Delta/g_c^2 \sim 3$, the hexagonal resonance contributes significantly to the delocalized dimer (plaquette) dynamics with $J_{\rm ring}/K_{\rm ring} \sim 2$. In particular, these diagonal dimers can play an active role in locally breaking down the U(1) gauge symmetry in an emergent manner. The delicate conditions to host new quantum phase harbouring these two competing quantum orders are now ripe.

The full phase diagram of the reactive many-body QED is shown in Fig. 4.1(f)-(g) for a Rydberg ice placed on an infinitely-long cylinder with $N_y=8$. The phase diagram was obtained by translational-invariant matrix product states with a snaking-algorithm on a cylinder optimized with infinite-size density-matrix renormalization group (iDMRG). To simulate the physics in the thermodynamical limit with long-range cavity modes, we restrict the simulation with algebraically-decaying cavity-mediated interaction leading to a quantum fluctuation $\sim t_{ij}(\hat{\sigma}^{(i)}_x\hat{\sigma}^{(j)}_x+\hat{\sigma}^{(i)}_y\hat{\sigma}^{(j)}_y)$ with spin-exchange coefficient $t_{ij}\sim\left(\frac{a_0}{r_{ij}}\right)^{\alpha}$ and a_0 (r_{ij}) is the lattice constant (interatomic distance). Tunable-range quantum fluctuation can also be realized by multimode cavity QED in the limit $\Delta \gg g_c$ [188] with the single-mode limit recovered for $\alpha \to 0$ (infinite-range quantum fluctuation). The phase diagram of the entanglement entropy for $\alpha=6$ ($\alpha=3$) is shown in Fig. 4.1(f) (Fig. 4.1(g)) as a function of constraint Λ_G and electric charge $\mathcal{Q}$.

Apart from the trivial ferromagnetic phase $|\mathrm{FM}\rangle = |e \cdots e\rangle$, we find that a plethora of exotic quantum phases can be stabilized in the chequerboard-lattice reactive many-body QED, as summarized below:

Symmetry-broken phases

- Superradiance-like phase (SR): This state represents the trivially disordered and locally featureless phase at $\Lambda_G \to 0$, corresponding to the global spin-singlet phase in the limit of $\alpha \to 0$. The system is superfluid-like and the macroscopic wavefunction is described by a single-parameter global phase ϕ and by large dimer fluctuation. It is qualitatively similar to a coherent state consisting of superextensive unrestricted dimer patterns. As shown in Fig. 4.3 (c) and (d), the dimer fluctuations of the SR phase violate the local constraints. As such, gauge charge fluctuation proliferate in the system, and can condensed into a superfluid. This superfluid, from the perspective of the topological spin liquid, is our SR phase.

- Resonating plaquette solid (VBS_1): VBS_1 phase approximates the ground-state of the fcQED (Eq. 4.9) on a square lattice at $\mathcal{Q} = 0$ sector in the limit $U \to \infty$. The valence bond (plaquette) order and their crystalline pattern of the magnetic flux $\langle \hat{X}_{\square}^{(ijkl)} \rangle$ with $\hat{X}_{\square}^{(ijkl)} = \prod_{i \in \square} \hat{\sigma}_x^{(i)}$ over $\square$ persist over a long range. From the spin liquid perspective, VBS_1 is driven by the condensation of visons, breaking the translation symmetry.

- Stripped plaquette solid (VBS_2): The stripped VBS_2 phase is valence bond solid pattern of $\langle \hat{X}_{\square}^{(ijkl)} \hat{Z}_{\boxtimes}^{(lmno)} \rangle$ with $\hat{Z}_{\boxtimes}^{(ijkl)} = \prod_{i \in \boxtimes} \hat{\sigma}_z^{(i)}$ over $\boxtimes$, which extends over an enlarged square lattice. This phase is generated by condensing emergent fermions (vison-spinon bound state) of the $\mathbb{Z}_2$ spin liquid.

- Resonating plaquette solid (VBS_3): VBS_3 phase is another pattern of valence bond solid over an extended lattice, yet incompatible with the dimer/plaquette patterns of VBS_2.

Quantum phases

- Gapped $\mathbb{Z}_2$ spin liquid (QSL): The $\mathbb{Z}_2$ spin liquid is the Higgs phase of the U(1) lattice gauge theory. In the intermediate range of Λ_G, the local constraint is now only soft and the long-range dimer resonances explicitly break the bipartiteness of the chequerboard lattice. In particular, diagonal dimers placed on the chequerboard lattice act as charge-2 Higgs scalar fields, which themselves can locally condense and

induce a symmetry breaking of the gauge group to $\mathbb{Z}_2$. The Higgs condensation mechanism opens up a gap for the instantons, which otherwise would destroy the spin liquid. The spin liquid phase itself is belongs to the toric-code universality class and is stabilized by the presence of long-range cavity QED fluctuation. As shown in the inset to Fig. 4.1, the QSL phase remain featureless and disordered when probed locally by both plaquette operators $\hat{X}_{\square}^{(ijkl)}$, $\hat{Z}_{\square}^{(ijkl)}$, while the extensive dimer patterns of its RVB representation restricted to the local symmetry sector $\mathcal{Q} = 0$. It is thus a short-ranged RVB state. Direct evidences for the $\mathbb{Z}_2$ spin liquid are provided in the following sections, including the real-space topological string order parameter, topological entanglement entropy, and the modular S transformation between the superselection sectors.

- Critical QED_3 spin liquid (QED_3): This spin liquid state is generated by a possible deconfined quantum criticality (DQC) at $\mathcal{Q} = 1$ between two mutually incompatible symmetry-broken phase VBS_1 and VBS_3. Similar to the Kagome lattice, the low-energy theory for this critical phase is described by a dynamical U(1) gauge field coupled to dynamical matter fields. Similar to the easy-axis Kagome lattice with triangular constraints, at $\mathcal{Q} = 1$, there are two flavours of gapless gauge charges that can strongly couple to the dynamical gauge field. The key evidences for the projected symmetry group of the gapless spin liquid are the existence of logarithmically scaling entanglement entropy, the gapless collective photon mode in the transfer matrix spectrum, and the ground-state response to a vison flux insertion threading the cylinder. An indirect consequence of the gapless collective photon modes is found in the inset to Fig. 4.1, where faint blue-colored excited dimer modes are delocalized over the entire system. Further investigation of QED_3 phase is required to determine the particular conformal field theory in the strong coupling, as there are other competing theories of gapless $\mathbb{Z}_2$ spin liquids on a square lattice [255–257].

The symmetry-broken VBS phases are unique in that their spin-spin correlations, like their spin liquid counterpart, do not exhibit long-range order. However, VBS is a weakly entangled phase and have structuring ordering of the dimers. As such, the hidden order can be exposed in Fig. 4.3(g)-(h) by examining the plaquette-plaquette correlations. Upon such an analysis, only the QSL and QED_3 phases demonstrate the absence of long-range ordering of local operators in both spin and dimer/plaquette degree of freedom. This is most radically shown in the exponential (algebraic) decay of the plaquette-plaquette correlations for the QSL (QED_3) phase in Fig. 4.3(e).

Another crucial aspect is that the stability of the spin liquid arises from the Higgs condensation of the diagonal dimer bonds. With smaller scaling form $\alpha \to 0$, the stability

of the topological phase is expected to persist, as shown vividly in Fig. 4.3(f). The QSL phase is indeed marked by the reduction of the dimer structural factor (SFF).

We now turn to the question of a positive identification of the deconfinement. In Fig. 4.4, we demonstrate the utilization of the real-space Wilson loop $\hat{X}_{\mathcal{C}}(\hat{Z}_{\mathcal{C}}) = \prod_{i\in\mathcal{C}} \hat{\sigma}_x^{(i)}(\hat{\sigma}_z^{(i)})$ along a close contour $\mathcal{C}$ for the electric and magnetic field basis, respectively. The deconfined phase of a gauge theory is describe by a boundary-scaling decay of the Wilsonian loops. The boundary scaling of the Wilson loop is clearly demonstrated in Fig. 4.4(e)-(f) for both the QSL and QED_3 phase, as well as the VBS_1.

The physical origin of the boundary-scaling relationship for these loop operators is the entanglement structure of the quantum field theory. However, in the presence of matter fields, in this case with the Higgs fields, it is not possible to distinguish the local structure arising from the interaction between the gauge fields and the Higgs charges, from the genuine deconfinement arising from the free gauge theory. As such, the Wilson loop themselves cannot correctly identify the deconfined phase. We thereby consider an alternative measure as follows.

Now, we consider normalized half-loops in the real-space, also known as the FM order parameter. Qualitatively, the FM order parameter describes the degree of entanglement of the loops. Namely, if the loops can be factorized as a product of two strings, the normalized order parameter will reach 1. On the other hand, the suppression of the string order parameter indicates the presence of strong correlations and entanglement for the loop. From a different perspective, the string operator measures the density of the anyons at the end points of the string. For instance, the X_{string} (Z_{string}) measures the spinon (vison) density at the end points.

As shown in Fig. 4.5, the FM order parameters $F_{X,Z}$ are suppressed for both quantum phases QSL and QED_3. As a non-local order parameter, the FM order parameter can correctly capture the deconfined nature of the two spin liquids. What is even more intriguing is that it can provide a correct projected symmetry classification by analysing the proximal classical phases harboring the quantum phases.

Namely, the SR and VBS_3 are identified by the proliferation of emergent fermions (vison-spinon bound states) in Fig. 4.5, which condense the classical phases of SR and VBS_3 (superconductor with different orbital pairing from the perspective of the anyons). On the other hand, the VBS_1 exhibits a large vison population, consistent with the theory of valence bond solids for the quantum dimer model on a square lattice. Hence, from the analysis of the descendent classical phases, we provide a strong evidence of a $\mathbb{Z}_2$ spin liquid characterized by four topological sectors (unity, vison, spinon, emergent fermion threading through the cylinder).

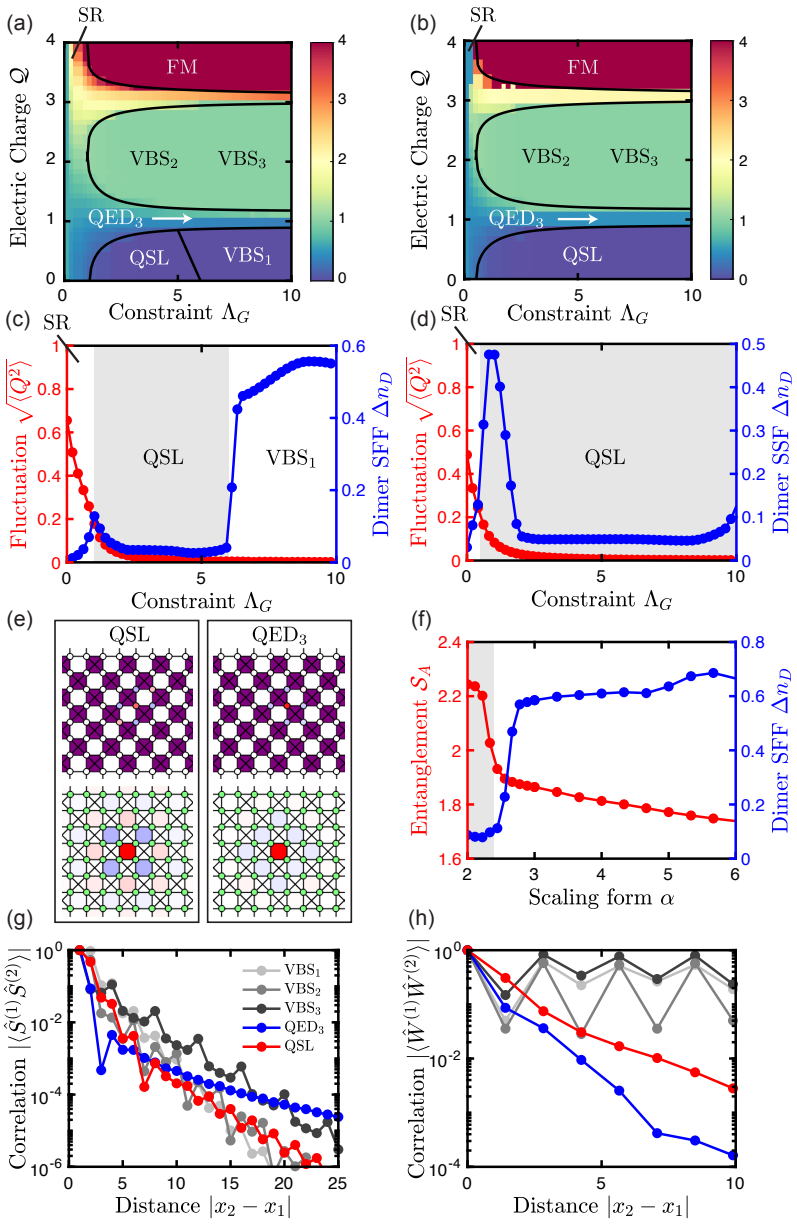

Figure 4.3: Enforcement of local gauge symmetry and valence bond structure. (a) Coupling a 2D Rydberg spin ice with a local $U(1)$ gauge symmetry to a multimode optical cavity in the reactive limit. Many-body states are locally constrained by a Ising-like Hamiltonian to the gauge sector $\mathcal{Q}$ within the purple plaquettes, while quantum fluctuation is injected to the many-body system by way of cavity QED. (b) Coarse-graining procedure of many-body QED for stabilizing the vacuum state of topological and conformal field theories. In the long-wavelength limit, non-trivial quasiparticles (spinon, visons, and collective photon modes) emerge within different topological and conformal sectors. (c) Spinons and visons in the deconfined phase of $\mathbb{Z}_2$ lattice gauge theory. Spinon and vison are mutual semions whose mutual exchange statistics is governed by an Abelian phase $\theta_{sv} = \pi/2$. (d) Quantum dimer dynamics mediated by cavity QED vacuum bath. Quantum dynamics involving non-bipartite dimers are driven by long-range cavity-mediated interactions.

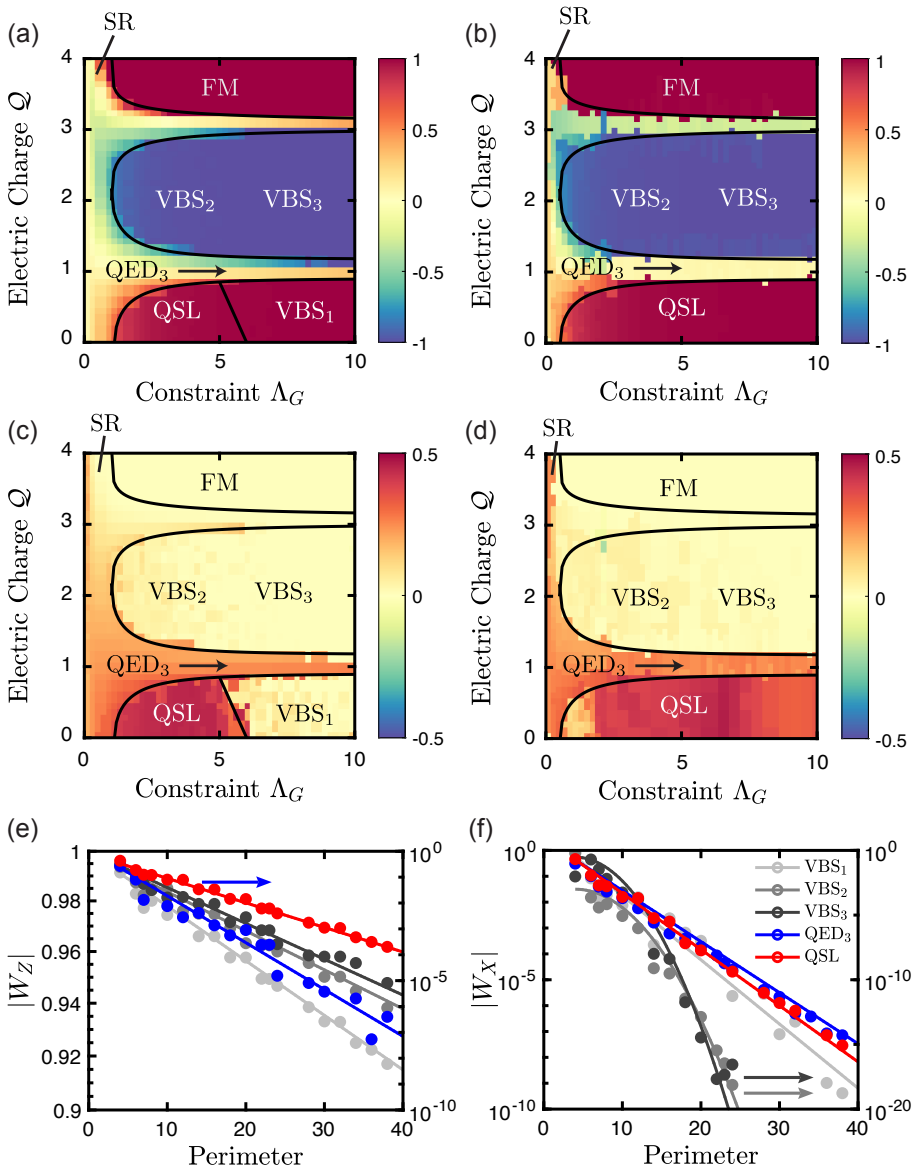

Figure 4.4: Detection of deconfined quantum liquids with loop tomography. (a) Coupling a 2D Rydberg spin ice with a local $U(1)$ gauge symmetry to a multimode optical cavity in the reactive limit. Many-body states are locally constrained by a Ising-like Hamiltonian to the gauge sector $\mathcal{Q}$ within the purple plaquettes, while quantum fluctuation is injected to the many-body system by way of cavity QED.

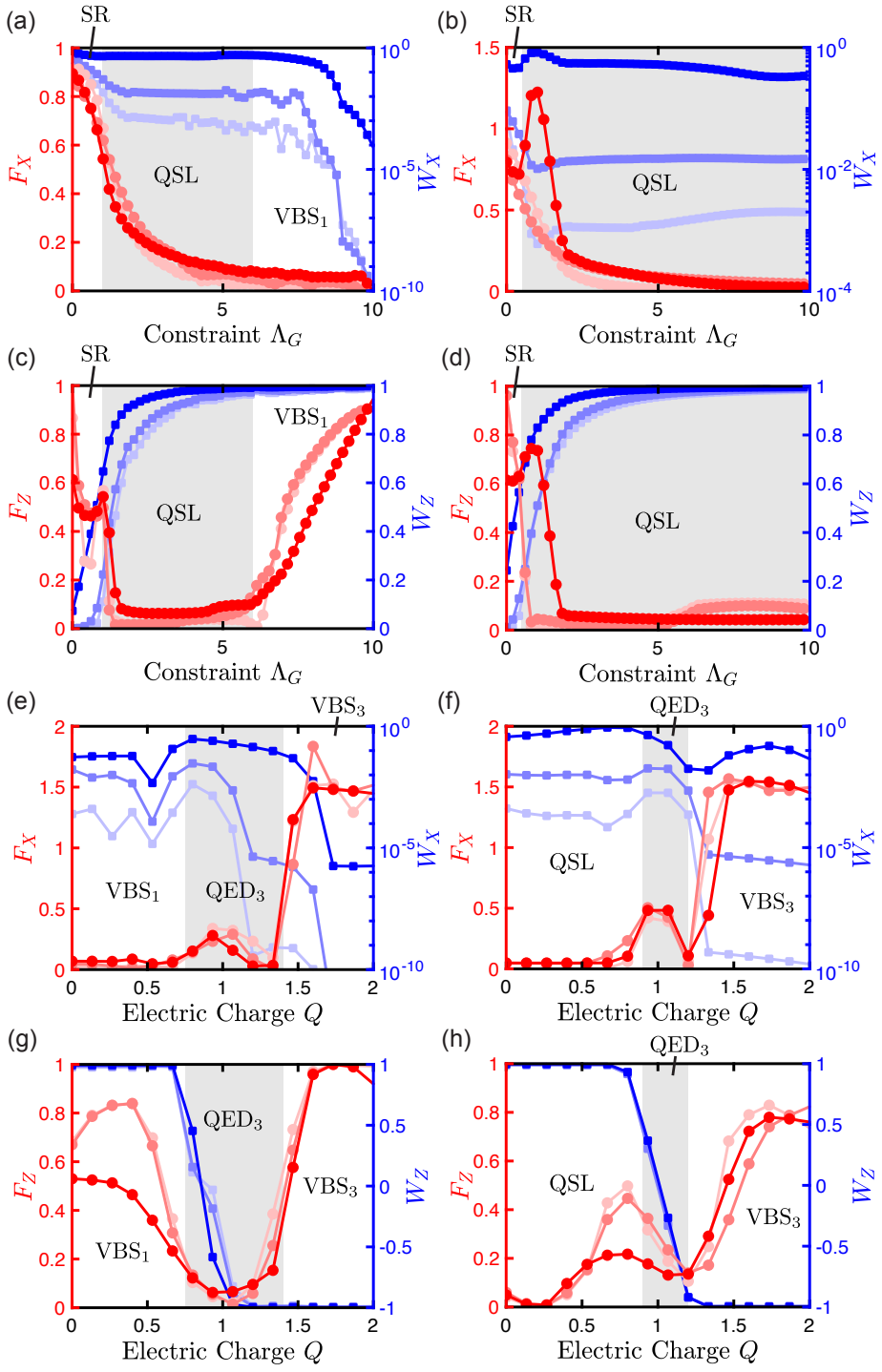

Figure 4.5: FM order parameter. (a) Coupling a 2D Rydberg spin ice with a local $U(1)$ gauge symmetry to a multimode optical cavity in the reactive limit. Many-body states are locally constrained by a Ising-like Hamiltonian to the gauge sector $\mathcal{Q}$ within the purple plaquettes, while quantum fluctuation is injected to the many-body system by way of cavity QED.

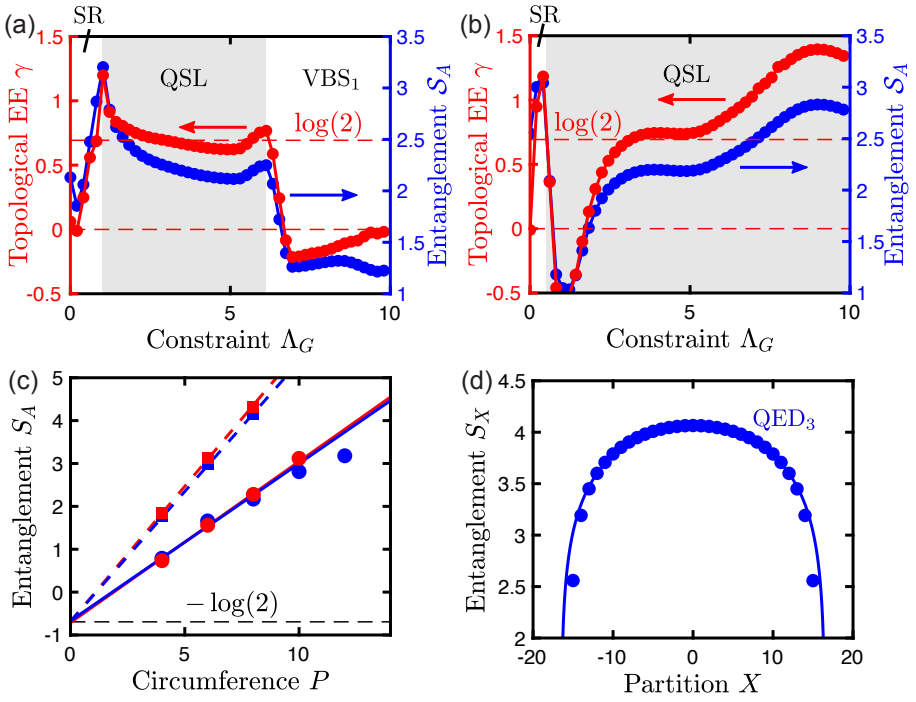

Figure 4.6: Entanglement signatures of quantum spin liquids. (a) Coupling a 2D Rydberg spin ice with a local $U(1)$ gauge symmetry to a multimode optical cavity in the reactive limit. Many-body states are locally constrained by a Ising-like Hamiltonian to the gauge sector $\mathcal{Q}$ within the purple plaquettes, while quantum fluctuation is injected to the many-body system by way of cavity QED.

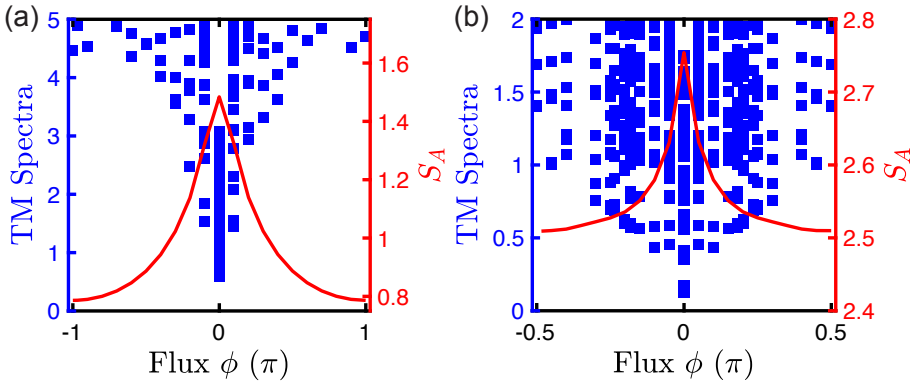

Figure 4.7: Low-energy excitations of quantum spin liquids. (a) Coupling a 2D Rydberg spin ice with a local $U(1)$ gauge symmetry to a multimode optical cavity in the reactive limit. Many-body states are locally constrained by a Ising-like Hamiltonian to the gauge sector $\mathcal{Q}$ within the purple plaquettes, while quantum fluctuation is injected to the many-body system by way of cavity QED.

Chapter 5

Conclusion

5.1 Summary of thesis

In chapter 2, I presented an in-depth background on the construction of tensor network states and commonly used variational methods arising from them for the classical simulation of quantum many-body systems. This included the representations of quantum states within the framework of matrix product states (MPS) and quantum operators in matrix product operators (MPO).

A description of their basic creation and an explanation of their utility were given. Following this, I presented standard algorithms such as the iterative variational optimization of ground states for MPOs using the Density Matrix Renormalization Group (DMRG) and its infinite state variant, IDMRG. Then, I described a method for simulating time-evolution (both within a domain of real and imaginary time) of a MPS called, Time Dependent Variational Principles (TDVP).

A discussion was given about performing a numerical simulation of open quantum systems and how the master equation is handled in practice. In this, I provided two common numerical methods; the first being the trajectory method, which consists of performing a non-Hermitian evolution along with the possibility of jumps several times to generate statistics required for the density matrix. The second being the vectorized density matrix, which consists of treating the entire density matrix as a quantum state within an enlarged Hilbert space. The later works by either evolving or obtaining the steady-state solution via a DMRG to reduce the Liouvillian functional of the vectorized super-operator describing the open system dynamics.

In chapter 3, we propose a waveguide QED platform capable of realizing universal quantum matter through direct control of the 2-local Hamiltonian $\hat{H}_{\mathrm{QMA}}$ operators. This

is implemented by engineering the coupling between the phononic superfluid and the atomic spins as needed. This work was originally published in Ref. [1].

The waveguide toolbox, unlike a digital simulator, is analog and fully manifests the system of the virtual matter, not just the ground state, allowing the entirety of the spectrum to be utilized. We discuss the emergence of SU(n) models by gauging the waveguide QED simulator and encoding it onto the low-energy theory of the waveguide QED simulator. Moreover, the static and dynamical structures of arbitrary k-local Hamiltonian $\hat{H}_{\text{target}}$ with $k > 2$ of arbitrary dimension can be prescribed to the low-energy theory of the waveguide QED simulator. To access our SU(n) simulators capability we have analyzed the paradigmatic quantum field theory, the Wess-Zumino-Witten (WZW) model by accessing phase diagrams, static and dynamical response functions, and CFT entanglement of the many-body system with matrix product states.

Currently, the waveguide quantum simulator works by using non-interacting phonons as a linear mediator. One approach would be to create a phonon-phonon interaction that directly implements a gauge constraint, similar to the one we used to compute SU(N). In principle, this should not give us any wider range of computeability since the toolbox is already universal. However, allowing us to directly implement the gauge constraint still yields some potential advantages. Implementing a higher number of spin interactions may necessitate several layers of perturbative expansion. It is particularly evident in the simple case of a many-body fermion model and the Jordan Wigner transformation, which requires an N-body operator. In theory, it is possible to simulate it, but it may become impractical in practice. This is often true for lattice gauge theory systems, in particular [20]. Alternatively, we could try to directly engineer interactions between the spins to have a direct gauge symmetry. In this case, some natural phenomenon like the Van der Waal [258] interactions of Rydberg atoms would be used. We could then try to add quantum fluctuations to this system. Doing this would allow our toolbox to perform computations in a manner similar to that of chapter 4.

In chapter 4, we discussed our recent work on stabilizing dynamical gauge fields in the many-body QED platform. We described the physics of many-body QED, where local U(1) gauge constraints on the Rydberg gain medium (in a chequerboard lattice) can be promoted to frustrated compact QED plus Higgs fields. These Higgs fields can condense and break the local gauge symmetry to a finite gauge group, such as Z_2. These Higgs fields originate from the long-range nature of the cavity-mediated interactions and the insertion of zero-dimensional quantum fluctuations into the 2D Rydberg ice. We describe a mean-field method based on a novel Jordan-Wigner transformation to obtain the parton picture of the QED_3 deconfined criticality. This gapless spin liquid is thought to be the parent of the purported gapped Z2 spin liquid, which exists at intermediate coupling.

We provide strong theoretical evidence for the spin liquids by examining the real-space FM string operators and Wilson/Hooft's loop operators. We find the divergence of string tensions in the symmetry-broken phases harbouring the disordered liquid phase. On the other hand, Wilson loops over non-contractable topologies provide signatures of the topological order for the ground state wavefunction, enabling positive identification of the spin liquid. Moreover, the correlations between the Wilson loops and the uncertainty can be mapped to an entanglement witness, called quantum Fisher information, allowing us to obtain the topological index of the gapped spin liquid. This method allows us to identify the spin liquid as in the toric code's universality class. Furthermore, we reconstruct the modular matrices for the collective excitations from the vacuum of the spin liquid, directly accessing the anyonic nature of the braiding statistics (spinon, vison, and emergent fermions). Finally, we examine the flux-dependent entanglement entropy and low-energy spectrum via transfer matrix methods. This provides us access to the presence of a linearly dispersed gapless mode in the CFT state, strongly suggestive of the emergent photon mode of QED_3. Together with this evidence, we conclude that the ground state of the cavity-coupled Rydberg ice permits a rich phase diagram, consisting of two flavours of quantum spin liquid phases.

5.2 Prospects

5.2.1 Dissipative ground-state cooling of universal lattice spin models

One direction that we are presently working on is quantum reservoir engineering of the many-body QED platform in the limit of dissipative SU(2) constraints. Unlike prior work on steady-state entangled states and reservoir computation [259], our recent work allows the dissipative preparation of low-energy states (thermal states) of universal models. That is, the 2-local spin model can encode the entire spectrum and dynamical response functions of any Hamiltonian. Ground-state cooling of a universal local Hamiltonian is known to be QMA-complete, and, as such, even universal quantum computers would not be able to efficiently solve the ground-state energy problem in polynomial time. From a computational complexity perspective, our dissipative mechanism likely has similar constraints. However, a major benefit is that our cooling procedure is entirely independent of the fine-tuning of the Hamiltonian. That is, the cooling procedure requires no knowledge of the target model, whether or not it is gapped. As such, we do not suffer from the spectral gap of some adiabatic path.

5.2.2 Resonant coupling of many-body QED

In this work, we are currently investigating the resonant regime of many-body QED. The steady-state transmission spectra of many-body QED in earlier experiments in the UQML group have indicated highly complex and nonlinear excitation modes. The goal of this work is to explore the possible many-body atom-field states that would persist by a mere transmission measurement. While further work is required, the early experimental signature includes extreme bunching and anti-bunching at different frequency modes and pump power. This indicates the breakdown of the scaling parameter and strong-coupling effects for large $N \gg 1$, radically departing from the microscopic description of generalized cavity QED systems.

Bibliography

[1] Ying Dong, J Taylor, Youn Seok Lee, HR Kong, and KS Choi, "Waveguide-qed platform for synthetic quantum matter", Physical Review A **104**, 053703 (2021).

[2] J. Taylor, H. R. Kong, Y. Dong, and K. S. Choi, "Quantum phases of strongly-coupled many-body qed in reactive regime", arXiv:XXXX.XXXX (2022).

[3] Peter W Shor, "Polynomial-time algorithms for prime factorization and discrete logarithms on a quantum computer", SIAM review **41**, 303–332 (1999).

[4] Keren Li, Muxin Han, Dongxue Qu, Zichang Huang, Guilu Long, Yidun Wan, Dawei Lu, Bei Zeng, and Raymond Laflamme, "Measuring holographic entanglement entropy on a quantum simulator", npj Quantum Information **5**, 1–6 (2019).

[5] Jonathan Olson, Yudong Cao, Jonathan Romero, Peter Johnson, Pierre-Luc Dallaire-Demers, Nicolas Sawaya, Prineha Narang, Ian Kivlichan, Michael Wasielewski, and Alán Aspuru-Guzik, "Quantum information and computation for chemistry", arXiv preprint arXiv:1706.05413 (2017).

[6] Tomi H Johnson, Stephen R Clark, and Dieter Jaksch, "What is a quantum simulator?", EPJ Quantum Technology **1**, 1–12 (2014).

[7] Román Orús, "A practical introduction to tensor networks: matrix product states and projected entangled pair states", Annals of physics **349**, 117–158 (2014).

[8] Di Yan, Tao Wu, Ying Liu, and Yang Gao, "An efficient sparse-dense matrix multiplication on a multicore system", in 2017 ieee 17th international conference on communication technology (icct) (IEEE, 2017), pages 1880–1883.

[9] J Robert Johansson, Paul D Nation, and Franco Nori, "Qutip: an open-source python framework for the dynamics of open quantum systems", Computer Physics Communications **183**, 1760–1772 (2012).

[10] Dominik Muth, "Particle number conservation in quantum many-body simulations with matrix product operators", Journal of Statistical Mechanics: Theory and Experiment **2011**, P11020 (2011).

[11] Brian M Austin, Dmitry Yu Zubarev, and William A Lester Jr, "Quantum monte carlo and related approaches", Chemical reviews **112**, 263–288 (2012).

[12] Valentin Zauner, Damian Draxler, Laurence Vanderstraeten, Matthias Degroote, Jutho Haegeman, Marek M Rams, Vid Stojevic, Norbert Schuch, and Frank Verstraete, "Transfer matrices and excitations with matrix product states", New Journal of Physics **17**, 053002 (2015).

[13] Frank Verstraete and J Ignacio Cirac, "Valence-bond states for quantum computation", Physical Review A **70**, 060302 (2004).

[14] David Perez-Garcia, Frank Verstraete, Michael M Wolf, and J Ignacio Cirac, "Matrix product state representations", arXiv preprint quant-ph/0608197 (2006).

[15] Norbert Schuch, Michael M Wolf, Frank Verstraete, and J Ignacio Cirac, "Entropy scaling and simulability by matrix product states", Physical review letters **100**, 030504 (2008).

[16] Matthew B Hastings, "Entropy and entanglement in quantum ground states", Physical Review B **76**, 035114 (2007).

[17] Seth Lloyd, "Universal quantum simulators", Science **273**, 1073–1078 (1996).

[18] Rainer Blatt and Christian F Roos, "Quantum simulations with trapped ions", Nature Physics **8**, 277–284 (2012).

[19] Hannes Bernien, Sylvain Schwartz, Alexander Keesling, Harry Levine, Ahmed Omran, Hannes Pichler, Soonwon Choi, Alexander S Zibrov, Manuel Endres, Markus Greiner, et al., "Probing many-body dynamics on a 51-atom quantum simulator", Nature **551**, 579–584 (2017).

[20] Immanuel Bloch, "Quantum coherence and entanglement with ultracold atoms in optical lattices", Nature **453**, 1016–1022 (2008).

[21] Leon Balents, "Spin liquids in frustrated magnets", Nature **464**, 199–208 (2010).

[22] JS Helton, K Matan, MP Shores, EA Nytko, BM Bartlett, Y Yoshida, Y Takano, A Suslov, Y Qiu, J-H Chung, et al., "Spin dynamics of the spin-1/2 kagome lattice antiferromagnet zncu 3 (oh) 6 cl 2", Physical review letters **98**, 107204 (2007).

[23] Yoshihiko Okamoto, Minoru Nohara, Hiroko Aruga-Katori, and Hidenori Takagi, "Spin-liquid state in the s= 1/2 hyperkagome antiferromagnet na 4 ir 3 o 8", Physical review letters **99**, 137207 (2007).

[24] R Miller, TE Northup, KM Birnbaum, ADBA Boca, AD Boozer, and HJ Kimble, "Trapped atoms in cavity qed: coupling quantized light and matter", Journal of Physics B: Atomic, Molecular and Optical Physics **38**, S551 (2005).

[25] Edwin T Jaynes and Frederick W Cummings, "Comparison of quantum and semi-classical radiation theories with application to the beam maser", Proceedings of the IEEE **51**, 89–109 (1963).

[26] Tracy E Northup, *Coherent control in cavity qed* (California Institute of Technology, 2008).

[27] Mark Saffman, Thad G Walker, and Klaus Mølmer, "Quantum information with rydberg atoms", Reviews of modern physics **82**, 2313 (2010).

[28] Ulrich Schollwöck, "The density-matrix renormalization group in the age of matrix product states", Annals of physics **326**, 96–192 (2011).

[29] Ian P McCulloch, "Infinite size density matrix renormalization group, revisited", arXiv preprint arXiv:0804.2509 (2008).

[30] Mingru Yang and Steven R White, "Time-dependent variational principle with ancillary krylov subspace", Physical Review B **102**, 094315 (2020).

[31] Jacob Biamonte and Ville Bergholm, "Tensor networks in a nutshell", arXiv preprint arXiv:1708.00006 (2017).

[32] J Ignacio Cirac, David Perez-Garcia, Norbert Schuch, and Frank Verstraete, "Matrix product states and projected entangled pair states: concepts, symmetries, theorems", Reviews of Modern Physics **93**, 045003 (2021).

[33] Guifré Vidal, "Efficient classical simulation of slightly entangled quantum computations", Physical review letters **91**, 147902 (2003).

[34] Matthew Fishman, Steven R White, and E Miles Stoudenmire, "The itensor software library for tensor network calculations", arXiv preprint arXiv:2007.14822 **28** (2020).

[35] David J Griffiths and Darrell F Schroeter, *Introduction to quantum mechanics* (Cambridge university press, 2018).

[36] "An iteration method for the solution of the eigenvalue problem of linear differential and integral operators", Journal of research of the National Bureau of Standards **45**, 255–282 (1950).

[37] Walter Edwin Arnoldi, "The principle of minimized iterations in the solution of the matrix eigenvalue problem", Quarterly of applied mathematics **9**, 17–29 (1951).

[38] Eduardo Mascarenhas, Hugo Flayac, and Vincenzo Savona, "Matrix-product-operator approach to the nonequilibrium steady state of driven-dissipative quantum arrays", Physical Review A **92**, 022116 (2015).

[39] Jutho Haegeman, J Ignacio Cirac, Tobias J Osborne, Iztok Pižorn, Henri Verschelde, and Frank Verstraete, "Time-dependent variational principle for quantum lattices", Physical review letters **107**, 070601 (2011).

[40] Paul A Gagniuc, *Markov chains: from theory to implementation and experimentation* (John Wiley & Sons, 2017).

[41] Mikhail Lukin, *Lecture notes 285b*, 2005.

[42] Ehud Altman, Kenneth R Brown, Giuseppe Carleo, Lincoln D Carr, Eugene Demler, Cheng Chin, Brian DeMarco, Sophia E Economou, Mark A Eriksson, Kai-Mei C Fu, et al., "Quantum simulators: architectures and opportunities", PRX Quantum **2**, 017003 (2021).

[43] Shuntaro Takeda and Akira Furusawa, "Toward large-scale fault-tolerant universal photonic quantum computing", APL Photonics **4**, 060902 (2019).

[44] Jiehang Zhang, Guido Pagano, Paul W Hess, Antonis Kyprianidis, Patrick Becker, Harvey Kaplan, Alexey V Gorshkov, Z-X Gong, and Christopher Monroe, "Observation of a many-body dynamical phase transition with a 53-qubit quantum simulator", Nature **551**, 601–604 (2017).

[45] Frank Arute, Kunal Arya, Ryan Babbush, Dave Bacon, Joseph C Bardin, Rami Barends, Rupak Biswas, Sergio Boixo, Fernando GSL Brandao, David A Buell, et al., "Quantum supremacy using a programmable superconducting processor", Nature **574**, 505–510 (2019).

[46] Jae-yoon Choi, Sebastian Hild, Johannes Zeiher, Peter Schauß, Antonio Rubio-Abadal, Tarik Yefsah, Vedika Khemani, David A Huse, Immanuel Bloch, and Christian Gross, "Exploring the many-body localization transition in two dimensions", Science **352**, 1547–1552 (2016).

[47] Jacob D Biamonte and Peter J Love, "Realizable hamiltonians for universal adiabatic quantum computers", Physical Review A **78**, 012352 (2008).

[48] Daniel Nagaj and Pawel Wocjan, "Hamiltonian quantum cellular automata in one dimension", Physical Review A **78**, 032311 (2008).

[49] Karl GH Vollbrecht and J Ignacio Cirac, "Quantum simulators, continuous-time automata, and translationally invariant systems", Physical review letters **100**, 010501 (2008).

[50] Luigi Amico, Rosario Fazio, Andreas Osterloh, and Vlatko Vedral, "Entanglement in many-body systems", Reviews of modern physics **80**, 517 (2008).

[51] H Jeff Kimble, "The quantum internet", Nature **453**, 1023–1030 (2008).

[52] Immanuel Bloch, Jean Dalibard, and Wilhelm Zwerger, "Many-body physics with ultracold gases", Reviews of modern physics **80**, 885 (2008).

[53] Toby S. Cubitt, Ashley Montanaro, and Stephen Piddock, "Universal quantum hamiltonians", Proceedings of the National Academy of Sciences **115**, 9497–9502 (2018).

[54] Sajeev John and Jian Wang, "Quantum electrodynamics near a photonic band gap: photon bound states and dressed atoms", Physical review letters **64**, 2418 (1990).

[55] Gershon Kurizki, "Two-atom resonant radiative coupling in photonic band structures", Physical Review A **42**, 2915 (1990).

[56] Sajeev John and Tran Quang, "Quantum optical spin-glass state of impurity two-level atoms in a photonic band gap", Physical review letters **76**, 1320 (1996).

[57] CL Hung, SM Meenehan, DE Chang, O Painter, and HJ Kimble, "Trapped atoms in one-dimensional photonic crystals", New Journal of Physics **15**, 083026 (2013).

[58] Jeffrey Douglas Thompson, TG Tiecke, Nathalie P de Leon, J Feist, AV Akimov, M Gullans, Alexander S Zibrov, V Vuletić, and Mikhail D Lukin, "Coupling a single trapped atom to a nanoscale optical cavity", Science **340**, 1202–1205 (2013).

[59] T. G. Tiecke, J. D. Thompson, N. P. de Leon, L. R. Liu, V. Vuletić, and M. D. Lukin, "Nanophotonic quantum phase switch with a single atom", Nature **508**, 241–244 (2014).

[60] A Goban, C-L Hung, S-P Yu, JD Hood, JA Muniz, JH Lee, MJ Martin, AC McClung, KS Choi, Darrick E Chang, et al., "Atom–light interactions in photonic crystals", Nature communications **5**, 1–9 (2014).

[61] A. Goban, C.-L. Hung, J. D. Hood, S.-P. Yu, J. A. Muniz, O. Painter, and H. J. Kimble, "Superradiance for atoms trapped along a photonic crystal waveguide", Phys. Rev. Lett. **115**, 063601 (2015).

[62] Jonathan D Hood, Akihisa Goban, Ana Asenjo-Garcia, Mingwu Lu, Su-Peng Yu, Darrick E Chang, and HJ Kimble, "Atom–atom interactions around the band edge of a photonic crystal waveguide", Proceedings of the National Academy of Sciences **113**, 10507–10512 (2016).

[63] Polnop Samutpraphoot, Tamara orević, Paloma L Ocola, Hannes Bernien, Crystal Senko, Vladan Vuletić, and Mikhail D Lukin, "Strong coupling of two individually controlled atoms via a nanophotonic cavity", Physical review letters **124**, 063602 (2020).

[64] Tamara Dordević, Polnop Samutpraphoot, Paloma L Ocola, Hannes Bernien, Brandon Grinkemeyer, Ivana Dimitrova, Vladan Vuletić, and Mikhail D Lukin, "Entanglement transport and a nanophotonic interface for atoms in optical tweezers", Science **373**, 1511–1514 (2021).

[65] James S Douglas, Hessam Habibian, C-L Hung, Alexey V Gorshkov, H Jeff Kimble, and Darrick E Chang, "Quantum many-body models with cold atoms coupled to photonic crystals", Nature Photonics **9**, 326–331 (2015).

[66] Tao Shi, Ying-Hai Wu, Alejandro González-Tudela, and J Ignacio Cirac, "Bound states in boson impurity models", Physical Review X **6**, 021027 (2016).

[67] Giuseppe Calajó, Francesco Ciccarello, Darrick Chang, and Peter Rabl, "Atom-field dressed states in slow-light waveguide qed", Physical Review A **93**, 033833 (2016).

[68] Michael Gullans, TG Tiecke, DE Chang, J Feist, JD Thompson, J Ignacio Cirac, P Zoller, and Mikhail D Lukin, "Nanoplasmonic lattices for ultracold atoms", Physical review letters **109**, 235309 (2012).

[69] Alejandro González-Tudela, C-L Hung, Darrick E Chang, J Ignacio Cirac, and HJ Kimble, "Subwavelength vacuum lattices and atom–atom interactions in two-dimensional photonic crystals", Nature Photonics **9**, 320–325 (2015).

[70] C.-L. Hung, Alejandro González-Tudela, J. Ignacio Cirac, and H. J. Kimble, "Quantum spin dynamics with pairwise-tunable, long-range interactions", Proceedings of the National Academy of Sciences **113**, E4946–E4955 (2016).

[71] Michael J Hartmann, Fernando GSL Brandao, and Martin B Plenio, "Strongly interacting polaritons in coupled arrays of cavities", Nature Physics **2**, 849–855 (2006).

[72] Andrew D Greentree, Charles Tahan, Jared H Cole, and Lloyd CL Hollenberg, "Quantum phase transitions of light", Nature Physics **2**, 856–861 (2006).

[73] Tomás Ramos, Hannes Pichler, Andrew J Daley, and Peter Zoller, "Quantum spin dimers from chiral dissipation in cold-atom chains", Physical review letters **113**, 237203 (2014).

[74] Peter Lodahl, Sahand Mahmoodian, Søren Stobbe, Arno Rauschenbeutel, Philipp Schneeweiss, Jürgen Volz, Hannes Pichler, and Peter Zoller, "Chiral quantum optics", Nature **541**, 473–480 (2017).

[75] Hannes Pichler, Soonwon Choi, Peter Zoller, and Mikhail D Lukin, "Universal photonic quantum computation via time-delayed feedback", Proceedings of the National Academy of Sciences **114**, 11362–11367 (2017).

[76] Marco T Manzoni, Ludwig Mathey, and Darrick E Chang, "Designing exotic many-body states of atomic spin and motion in photonic crystals", Nature communications **8**, 1–9 (2017).

[77] Subir Sachdev, "Bekenstein-hawking entropy and strange metals", Physical Review X **5**, 041025 (2015).

[78] Alexei Kitaev, *A simple model of quantum holography.* Talks at KITP program: Entanglement in Strongly-Correlated Quantum Matter., 2015.

[79] Edward Witten, "Non-abelian bosonization in two dimensions", in *Bosonization* (World Scientific, 1994), pages 201–218.

[80] T Gruner and D-G Welsch, "Green-function approach to the radiation-field quantization for homogeneous and inhomogeneous kramers-kronig dielectrics", Physical Review A **53**, 1818 (1996).

[81] Ho Trung Dung, Ludwig Knöll, and Dirk-Gunnar Welsch, "Resonant dipole-dipole interaction in the presence of dispersing and absorbing surroundings", Physical Review A **66**, 063810 (2002).

[82] Gerasimos Angelatos, "Theory and applications of light-matter interactions in quantum dot nanowire photonic crystal systems", PhD thesis (2015).

[83] Ana Asenjo-Garcia, JD Hood, DE Chang, and HJ Kimble, "Atom-light interactions in quasi-one-dimensional nanostructures: a green's-function perspective", Physical Review A **95**, 033818 (2017).

[84] Ana Asenjo-Garcia, M Moreno-Cardoner, Andreas Albrecht, HJ Kimble, and Darrick E Chang, "Exponential improvement in photon storage fidelities using subradiance and "selective radiance" in atomic arrays", Physical Review X **7**, 031024 (2017).

[85] Dieter Jaksch and Peter Zoller, "Creation of effective magnetic fields in optical lattices: the hofstadter butterfly for cold neutral atoms", New Journal of Physics **5**, 56 (2003).

[86] Alejandro Bermudez, Tobias Schaetz, and Diego Porras, "Synthetic gauge fields for vibrational excitations of trapped ions", Physical review letters **107**, 150501 (2011).

[87] Simcha Korenblit, Dvir Kafri, Wess C Campbell, Rajibul Islam, Emily E Edwards, Zhe-Xuan Gong, Guin-Dar Lin, Lu-Ming Duan, Jungsang Kim, Kihwan Kim, et al., "Quantum simulation of spin models on an arbitrary lattice with trapped ions", New Journal of Physics **14**, 095024 (2012).

[88] Monika Aidelsburger, Marcos Atala, Michael Lohse, Julio T Barreiro, B Paredes, and Immanuel Bloch, "Realization of the hofstadter hamiltonian with ultracold atoms in optical lattices", Physical review letters **111**, 185301 (2013).

[89] Florentin Reiter and Anders S. Sørensen, "Effective operator formalism for open quantum systems", Phys. Rev. A **85**, 032111 (2012).

[90] V Kalmeyer and RB Laughlin, "Equivalence of the resonating-valence-bond and fractional quantum hall states", Physical review letters **59**, 2095 (1987).

[91] Bela Bauer, Lukasz Cincio, Brendan P Keller, Michele Dolfi, Guifre Vidal, Simon Trebst, and Andreas WW Ludwig, "Chiral spin liquid and emergent anyons in a kagome lattice mott insulator", Nature communications **5**, 1–8 (2014).

[92] Krishna Kumar, Kai Sun, and Eduardo Fradkin, "Chiral spin liquids on the kagome lattice", Physical Review B **92**, 094433 (2015).

[93] Karim Essafi, Owen Benton, and Ludovic DC Jaubert, "A kagome map of spin liquids from xxz to dzyaloshinskii–moriya ferromagnet", Nature Communications **7**, 1–7 (2016).

[94] Leon Balents, Matthew PA Fisher, and Steven M Girvin, "Fractionalization in an easy-axis kagome antiferromagnet", Physical Review B **65**, 224412 (2002).

[95] Sergei V Isakov, Matthew B Hastings, and Roger G Melko, "Topological entanglement entropy of a bose–hubbard spin liquid", Nature Physics **7**, 772–775 (2011).

[96] Michel JP Gingras and Paul A McClarty, "Quantum spin ice: a search for gapless quantum spin liquids in pyrochlore magnets", Reports on Progress in Physics **77**, 056501 (2014).

[97] C. Castelnovo, R. Moessner, and S. L. Sondhi, "Magnetic monopoles in spin ice", Nature **451**, 42–45 (2008).

[98] Alexey Vyacheslavovich Gorshkov, M Hermele, V Gurarie, C Xu, Paul S Julienne, J Ye, Peter Zoller, Eugene Demler, Mikhail D Lukin, and AM Rey, "Two-orbital su (n) magnetism with ultracold alkaline-earth atoms", Nature physics **6**, 289–295 (2010).

[99] Yoshinori Tokura and Naoto Nagaosa, "Orbital physics in transition-metal oxides", science **288**, 462–468 (2000).

[100] N Read and Subir Sachdev, "Valence-bond and spin-peierls ground states of low-dimensional quantum antiferromagnets", Physical review letters **62**, 1694 (1989).

[101] J Brad Marston and Ian Affleck, "Large-n limit of the hubbard-heisenberg model", Physical Review B **39**, 11538 (1989).

[102] Martin Greiter and Stephan Rachel, "Valence bond solids for su (n) spin chains: exact models, spinon confinement, and the haldane gap", Physical Review B **75**, 184441 (2007).

[103] Ian Affleck, "Quantum spin chains and the haldane gap", Journal of Physics: Condensed Matter **1**, 3047 (1989).

[104] Julius Wess and Bruno Zumino, "Consequences of anomalous ward identities", Physics Letters B **37**, 95–97 (1971).

[105] Subir Sachdev and Jinwu Ye, "Gapless spin-fluid ground state in a random quantum heisenberg magnet", Physical review letters **70**, 3339 (1993).

[106] Alexei Kitaev, "Hidden correlations in the hawking radiation and thermal noise", in Talk given at the fundamental physics prize symposium, Vol. 10 (2014).

[107] Stephen H Shenker and Douglas Stanford, "Black holes and the butterfly effect", Journal of High Energy Physics **2014**, 1–25 (2014).

[108] Juan Maldacena, Stephen H Shenker, and Douglas Stanford, "A bound on chaos", Journal of High Energy Physics **2016**, 1–17 (2016).

[109] Edward Witten, "Global aspects of current algebra", Nuclear Physics B **223**, 422–432 (1983).

[110] Edward Witten, "Quantum field theory and the jones polynomial", Communications in Mathematical Physics **121**, 351–399 (1989).

[111] Olabode M Sule, Hitesh J Changlani, Isao Maruyama, and Shinsei Ryu, "Determination of tomonaga-luttinger parameters for a two-component liquid", Physical Review B **92**, 075128 (2015).

[112] Marcello Dalmonte, Benoît Vermersch, and Peter Zoller, "Quantum simulation and spectroscopy of entanglement hamiltonians", Nature Physics **14**, 827–831 (2018).

[113] Hui Li and F Duncan M Haldane, "Entanglement spectrum as a generalization of entanglement entropy: identification of topological order in non-abelian fractional quantum hall effect states", Physical review letters **101**, 010504 (2008).

[114] C Senko, J Smith, P Richerme, A Lee, WC Campbell, and C Monroe, "Coherent imaging spectroscopy of a quantum many-body spin system", Science **345**, 430–433 (2014).

[115] Pasquale Calabrese and John Cardy, "Entanglement entropy and conformal field theory", Journal of physics a: mathematical and theoretical **42**, 504005 (2009).

[116] Daniel Barredo, Sylvain de Léséleuc, Vincent Lienhard, Thierry Lahaye, and Antoine Browaeys, "An atom-by-atom assembler of defect-free arbitrary two-dimensional atomic arrays", Science **354**, 1021–1023 (2016).

[117] Manuel Endres, Hannes Bernien, Alexander Keesling, Harry Levine, Eric R. Anschuetz, Alexandre Krajenbrink, Crystal Senko, Vladan Vuletic, Markus Greiner, and Mikhail D. Lukin, "Atom-by-atom assembly of defect-free one-dimensional cold atom arrays", Science **354**, 1024–1027 (2016).

[118] Hyosub Kim, Woojun Lee, Han-gyeol Lee, Hanlae Jo, Yunheung Song, and Jaewook Ahn, "In situ single-atom array synthesis using dynamic holographic optical tweezers", Nature Communications **7**, 13317 (2016).

[119] Y Meng, A Dareau, P Schneeweiss, and A Rauschenbeutel, "Near-ground-state cooling of atoms optically trapped 300 nm away from a hot surface", Physical Review X **8**, 031054 (2018).

[120] Peter L McMahon, Alireza Marandi, Yoshitaka Haribara, Ryan Hamerly, Carsten Langrock, Shuhei Tamate, Takahiro Inagaki, Hiroki Takesue, Shoko Utsunomiya, Kazuyuki Aihara, et al., "A fully programmable 100-spin coherent ising machine with all-to-all connections", Science **354**, 614–617 (2016).

[121] Yoshitaka Haribara, Hitoshi Ishikawa, Shoko Utsunomiya, Kazuyuki Aihara, and Yoshihisa Yamamoto, "Performance evaluation of coherent ising machines against classical neural networks", Quantum Science and Technology **2**, 044002 (2017).

[122] Xingsheng Luan, Jean-Baptiste Béguin, Alex P Burgers, Zhongzhong Qin, Su-Peng Yu, and Harry J Kimble, "The integration of photonic crystal waveguides with atom arrays in optical tweezers", Advanced Quantum Technologies **3**, 2000008 (2020).

[123] Sougato Bose, "Quantum communication through an unmodulated spin chain", Physical review letters **91**, 207901 (2003).

[124] Matthias Christandl, Nilanjana Datta, Artur Ekert, and Andrew J Landahl, "Perfect state transfer in quantum spin networks", Physical review letters **92**, 187902 (2004).

[125] Mauro Paternostro, GM Palma, MS Kim, and G Falci, "Quantum-state transfer in imperfect artificial spin networks", Physical Review A **71**, 042311 (2005).

[126] Man-Hong Yung and Sougato Bose, "Perfect state transfer, effective gates, and entanglement generation in engineered bosonic and fermionic networks", Physical Review A **71**, 032310 (2005).

[127] Carlo Di Franco, Mauro Paternostro, and MS Kim, "Perfect state transfer on a spin chain without state initialization", Physical review letters **101**, 230502 (2008).

[128] Norman Y Yao, Liang Jiang, Alexey V Gorshkov, Peter C Maurer, Geza Giedke, J Ignacio Cirac, and Mikhail D Lukin, "Scalable architecture for a room temperature solid-state quantum information processor", Nature communications **3**, 1–8 (2012).

[129] Norman Y Yao, Chris R Laumann, Alexey V Gorshkov, Hendrik Weimer, Liang Jiang, J Ignacio Cirac, Peter Zoller, and Mikhail D Lukin, "Topologically protected quantum state transfer in a chiral spin liquid", Nature communications **4**, 1–8 (2013).

[130] S-P Yu, JD Hood, JA Muniz, MJ Martin, Richard Norte, C-L Hung, Seán M Meenehan, Justin D Cohen, Oskar Painter, and HJ Kimble, "Nanowire photonic crystal waveguides for single-atom trapping and strong light-matter interactions", Applied Physics Letters **104**, 111103 (2014).

[131] Thomas F Krauss, "Slow light in photonic crystal waveguides", Journal of Physics D: Applied Physics **40**, 2666 (2007).

[132] M. Arcari, I. Söllner, A. Javadi, S. Lindskov Hansen, S. Mahmoodian, J. Liu, H. Thyrrestrup, E. H. Lee, J. D. Song, S. Stobbe, and P. Lodahl, "Near-unity coupling efficiency of a quantum emitter to a photonic crystal waveguide", Phys. Rev. Lett. **113**, 093603 (2014).

[133] Peter Lodahl, Sahand Mahmoodian, and Søren Stobbe, "Interfacing single photons and single quantum dots with photonic nanostructures", Rev. Mod. Phys. **87**, 347–400 (2015).

[134] Steven G Johnson and John D Joannopoulos, "Block-iterative frequency-domain methods for maxwell's equations in a planewave basis", Optics express **8**, 173–190 (2001).

[135] Ardavan F Oskooi, David Roundy, Mihai Ibanescu, Peter Bermel, John D Joannopoulos, and Steven G Johnson, "Meep: a flexible free-software package for electromagnetic simulations by the fdtd method", Computer Physics Communications **181**, 687–702 (2010).

[136] Wonseok Shin and Shanhui Fan, "Choice of the perfectly matched layer boundary condition for frequency-domain maxwell's equations solvers", Journal of Computational Physics **231**, 3406–3431 (2012).

[137] Kazuaki Sakoda, *Optical properties of photonic crystals*, Vol. 80 (Springer Science & Business Media, 2004).

[138] C Van Vlack and Stephen Hughes, "Finite-difference time-domain technique as an efficient tool for calculating the regularized green function: applications to the local-field problem in quantum optics for inhomogeneous lossy materials", Optics Letters **37**, 2880–2882 (2012).

[139] M Kanskar, P Paddon, V Pacradouni, R Morin, A Busch, Jeff F Young, SR Johnson, Jim MacKenzie, and T Tiedje, "Observation of leaky slab modes in an air-bridged semiconductor waveguide with a two-dimensional photonic lattice", Applied physics letters **70**, 1438–1440 (1997).

[140] KB Crozier, Virginie Lousse, Onur Kilic, Sora Kim, Shanhui Fan, and Olav Solgaard, "Air-bridged photonic crystal slabs at visible and near-infrared wavelengths", Physical Review B **73**, 115126 (2006).

[141] Simon Bernard, Christoph Reinhardt, Vincent Dumont, Yves-Alain Peter, and Jack C Sankey, "Precision resonance tuning and design of sin photonic crystal reflectors", Optics Letters **41**, 5624–5627 (2016).

[142] Fabrice Gerbier and Yvan Castin, "Heating rates for an atom in a far-detuned optical lattice", Physical Review A **82**, 013615 (2010).

[143] RA Cline, JD Miller, MR Matthews, and DJ Heinzen, "Spin relaxation of optically trapped atoms by light scattering", Optics letters **19**, 207–209 (1994).

[144] Chigak Itoi and Masa-Hide Kato, "Extended massless phase and the haldane phase in a spin-1 isotropic antiferromagnetic chain", Physical Review B **55**, 8295 (1997).

[145] Lucile Savary and Leon Balents, "Quantum spin liquids: a review", Reports on Progress in Physics **80**, 016502 (2016).

[146] Eric Dennis, Alexei Kitaev, Andrew Landahl, and John Preskill, "Topological quantum memory", Journal of Mathematical Physics **43**, 4452–4505 (2002).

[147] Sergey Bravyi, Matthew B Hastings, and Spyridon Michalakis, "Topological quantum order: stability under local perturbations", Journal of mathematical physics **51**, 093512 (2010).

[148] Sankar Das Sarma, Michael Freedman, and Chetan Nayak, "Topological quantum computation", Physics today **59**, 32–38 (2006).

[149] Chetan Nayak, Steven H Simon, Ady Stern, Michael Freedman, and Sankar Das Sarma, "Non-abelian anyons and topological quantum computation", Reviews of Modern Physics **80**, 1083 (2008).

[150] Roman M Lutchyn, Jay D Sau, and S Das Sarma, "Majorana fermions and a topological phase transition in semiconductor-superconductor heterostructures", Physical review letters **105**, 077001 (2010).

[151] KJ Satzinger, Y-J Liu, A Smith, C Knapp, M Newman, C Jones, Z Chen, C Quintana, X Mi, A Dunsworth, et al., "Realizing topologically ordered states on a quantum processor", Science **374**, 1237–1241 (2021).

[152] Cheng Peng, Yi-Fan Jiang, Dong-Ning Sheng, and Hong-Chen Jiang, "Doping quantum spin liquids on the kagome lattice", Advanced Quantum Technologies **4**, 2000126 (2021).

[153] Jinsheng Wen, Shun-Li Yu, Shiyan Li, Weiqiang Yu, and Jian-Xin Li, "Experimental identification of quantum spin liquids", npj Quantum Materials **4**, 1–9 (2019).

[154] Yi Zhou, Kazushi Kanoda, and Tai-Kai Ng, "Quantum spin liquid states", Rev. Mod. Phys. **89**, 025003 (2017).

[155] Giuliano Giudici, Mikhail D Lukin, and Hannes Pichler, "Dynamical preparation of quantum spin liquids in rydberg atom arrays", arXiv preprint arXiv:2201.04034 (2022).

[156] J. M. Raimond, M. Brune, and S. Haroche, "Manipulating quantum entanglement with atoms and photons in a cavity", Rev. Mod. Phys. **73**, 565–582 (2001).

[157] H. Walther, B. T. H. Varcoe, B.-G. Englert, and T. Becker, "Cavity quantum electrodynamics", Rep. Prog. Phys. **69**, 1325 (2006).

[158] D. E. Chang, J. S. Douglas, A. González-Tudela, C.-L. Hung, and H. J. Kimble, "Colloquium: quantum matter built from nanoscopic lattices of atoms and photons", Rev. Mod. Phys. **90**, 031002 (2018).

[159] Alexandre Blais, Arne L. Grimsmo, S. M. Girvin, and Andreas Wallraff, "Circuit quantum electrodynamics", Rev. Mod. Phys. **93**, 025005 (2021).

[160] K.H. Drexhage, "Influence of a dielectric interface on fluorescence decay time", Journal of Luminescence **1-2**, 693–701 (1970).

[161] L. A. Orozco, A. T. Rosenberger, and H. J. Kimble, "Intrinsic dynamical instability in optical bistability with two-level atoms", Phys. Rev. Lett. **53**, 2547–2550 (1984).

[162] Randall G. Hulet, Eric S. Hilfer, and Daniel Kleppner, "Inhibited spontaneous emission by a Rydberg atom", Phys. Rev. Lett. **55**, 2137–2140 (1985).

[163] Gerald Gabrielse and Hans Dehmelt, "Observation of inhibited spontaneous emission", Phys. Rev. Lett. **55**, 67–70 (1985).

[164] Gerhard Rempe, Herbert Walther, and Norbert Klein, "Observation of quantum collapse and revival in a one-atom maser", Phys. Rev. Lett. **58**, 353–356 (1987).

[165] R. J. Thompson, G. Rempe, and H. J. Kimble, "Observation of normal-mode splitting for an atom in an optical cavity", Phys. Rev. Lett. **68**, 1132–1135 (1992).

[166] M. Brune, F. Schmidt-Kaler, A. Maali, J. Dreyer, E. Hagley, J. M. Raimond, and S. Haroche, "Quantum rabi oscillation: a direct test of field quantization in a cavity", Phys. Rev. Lett. **76**, 1800–1803 (1996).

[167] R. J. Thompson, Q. A. Turchette, O. Carnal, and H. J. Kimble, "Nonlinear spectroscopy in the strong-coupling regime of cavity qed", Phys. Rev. A **57**, 3084–3104 (1998).

[168] A. Wallraff, D. I. Schuster, A. Blais, L. Frunzio, R. S. Huang, J. Majer, S. Kumar, S. M. Girvin, and R. J. Schoelkopf, "Strong coupling of a single photon to a superconducting qubit using circuit quantum electrodynamics", Nature **431**, 162–167 (2004).

[169] J. P. Reithmaier, G. Sek, A. Loffler, C. Hofmann, S. Kuhn, S. Reitzenstein, L. V. Keldysh, V. D. Kulakovskii, T. L. Reinecke, and A. Forchel, "Strong coupling in a single quantum dot–semiconductor microcavity system", Nature **432**, 197–200 (2004).

[170] Peter Lodahl, A. Floris van Driel, Ivan S. Nikolaev, Arie Irman, Karin Overgaag, Daniël Vanmaekelbergh, and Willem L. Vos, "Controlling the dynamics of spontaneous emission from quantum dots by photonic crystals", Nature **430**, 654–657 (2004).

[171] Dirk Englund, David Fattal, Edo Waks, Glenn Solomon, Bingyang Zhang, Toshihiro Nakaoka, Yasuhiko Arakawa, Yoshihisa Yamamoto, familyi=c., given=Jelena, giveni=J., ,, and, "Controlling the spontaneous emission rate of single quantum dots in a two-dimensional photonic crystal", Phys. Rev. Lett. **95**, 013904 (2005).

[172] Takao Aoki, Barak Dayan, E. Wilcut, W. P. Bowen, A. S. Parkins, T. J. Kippenberg, K. J. Vahala, and H. J. Kimble, "Observation of strong coupling between one atom and a monolithic microresonator", Nature **443**, 671–674 (2006).

[173] J. Kasprzak, M. Richard, S. Kundermann, A. Baas, P. Jeambrun, J. M. J. Keeling, F. M. Marchetti, M. H. Szymańska, R. André, J. L. Staehli, V. Savona, P. B. Littlewood, B. Deveaud, and Le Si Dang, "Bose–einstein condensation of exciton polaritons", Nature **443**, 409–414 (2006).

[174] S. Gopalakrishnan, B. L. Lev, and P. M. Goldbart, "Emergent crystallinity and frustration with bose–einstein condensates in multimode cavities", Nature Phys. **5**, 845–850 (2009).

[175] Matt Eichenfield, Jasper Chan, Ryan M. Camacho, Kerry J. Vahala, and Oskar Painter, "Optomechanical crystals", Nature **462**, 78–82 (2009).

[176] Kristian Baumann, Christine Guerlin, Ferdinand Brennecke, and Tilman Esslinger, "Dicke quantum phase transition with a superfluid gas in an optical cavity", Nature **464**, 1301–1306 (2010).

[177] E. Vetsch, D. Reitz, G. Sagué, R. Schmidt, S. T. Dawkins, and A. Rauschenbeutel, "Optical interface created by laser-cooled atoms trapped in the evanescent field surrounding an optical nanofiber", Phys. Rev. Lett. **104**, 203603 (2010).

[178] D. Fausti, R. I. Tobey, N. Dean, S. Kaiser, A. Dienst, M. C. Hoffmann, S. Pyon, T. Takayama, H. Takagi, and A. Cavalleri, "Light-induced superconductivity in a stripe-ordered Cuprate", Science **331**, 189–191 (2011).

[179] Justin G. Bohnet, Zilong Chen, Joshua M. Weiner, Dominic Meiser, Murray J. Holland, and James K. Thompson, "A steady-state superradiant laser with less than one intracavity photon", Nature **484**, 78–81 (2012).

[180] A. Goban, K. S. Choi, D. J. Alton, D. Ding, C. Lacroûte, M. Pototschnig, T. Thiele, N. P. Stern, and H. J. Kimble, "Demonstration of a state-insensitive, compensated nanofiber trap", Phys. Rev. Lett. **109**, 033603 (2012).

[181] Thibault Peyronel, Ofer Firstenberg, Qi-Yu Liang, Sebastian Hofferberth, Alexey V. Gorshkov, Thomas Pohl, Mikhail D. Lukin, and Vladan Vuletić, "Quantum nonlinear optics with single photons enabled by strongly interacting atoms", Nature **488**, 57–60 (2012).

[182] Stephan Ritter, Christian Nölleke, Carolin Hahn, Andreas Reiserer, Andreas Neuzner, Manuel Uphoff, Martin Mücke, Eden Figueroa, Joerg Bochmann, and Gerhard Rempe, "An elementary quantum network of single atoms in optical cavities", Nature **484**, 195–200 (2012).

[183] Ofer Firstenberg, Thibault Peyronel, Qi-Yu Liang, Alexey V. Gorshkov, Mikhail D. Lukin, and Vladan Vuletić, "Attractive photons in a quantum nonlinear medium", Nature **502**, 71–75 (2013).

[184] A. Goban, C.-L. Hung, S.-P. Yu, J. D. Hood, J. A. Muniz, J. H. Lee, M. J. Martin, A. C. McClung, K. S. Choi, D. E. Chang, O. Painter, and H. J. Kimble, "Atom-light interactions in photonic crystals", Nature Comm. **5**, 3808 (2013).

[185] Jan Petersen, Jürgen Volz, and Arno Rauschenbeutel, "Chiral nanophotonic waveguide interface based on spin-orbit interaction of light", Science **346**, 67–71 (2014).

[186] Julian Léonard, Andrea Morales, Philip Zupancic, Tilman Esslinger, and Tobias Donner, "Supersolid formation in a quantum gas breaking a continuous translational symmetry", Nature **543**, 87–90 (2017).

[187] P. Forn-Díaz, J. J. García-Ripoll, B. Peropadre, J. L. Orgiazzi, M. A. Yurtalan, R. Belyansky, C. M. Wilson, and A. Lupascu, "Ultrastrong coupling of a single artificial atom to an electromagnetic continuum in the nonperturbative regime", Nature Physics **13**, 39–43 (2017).

[188] Varun D. Vaidya, Yudan Guo, Ronen M. Kroeze, Kyle E. Ballantine, Alicia J. Kollár, Jonathan Keeling, and Benjamin L. Lev, "Tunable-range, photon-mediated atomic interactions in multimode cavity QED", Phys. Rev. X **8**, 011002 (2018).

[189] Alicia J. Kollár, Mattias Fitzpatrick, and Andrew A. Houck, "Hyperbolic lattices in circuit quantum electrodynamics", Nature **571**, 45–50 (2019).

[190] Mohammad Mirhosseini, Eunjong Kim, Xueyue Zhang, Alp Sipahigil, Paul B. Dieterle, Andrew J. Keller, Ana Asenjo-Garcia, Darrick E. Chang, and Oskar Painter, "Cavity quantum electrodynamics with atom-like mirrors", Nature **569**, 692–697 (2019).

[191] Yudan Guo, Ronen M. Kroeze, Varun D. Vaidya, Jonathan Keeling, and Benjamin L. Lev, "Sign-changing photon-mediated atom interactions in multimode cavity quantum electrodynamics", Phys. Rev. Lett. **122**, 193601 (2019).

[192] Neil V. Corzo, Jérémy Raskop, Aveek Chandra, Alexandra S. Sheremet, Baptiste Gouraud, and Julien Laurat, "Waveguide-coupled single collective excitation of atomic arrays", Nature **566**, 359–362 (2019).

[193] Emily J. Davis, Gregory Bentsen, Lukas Homeier, Tracy Li, and Monika H. Schleier-Smith, "Photon-mediated spin-exchange dynamics of spin-1 atoms", Phys. Rev. Lett. **122**, 010405 (2019).

[194] A. Thomas, L. Lethuillier-Karl, K. Nagarajan, R. M. A. Vergauwe, J. George, T. Chervy, A. Shalabney, E. Devaux, C. Genet, J. Moran, and T. W. Ebbesen, "Tilting a ground-state reactivity landscape by vibrational strong coupling", Science **363**, 615–619 (2019).

[195] Bharath Kannan, Max J. Ruckriegel, Daniel L. Campbell, Anton Frisk Kockum, Jochen Braumüller, David K. Kim, Morten Kjaergaard, Philip Krantz, Alexander Melville, Bethany M. Niedzielski, Antti Vepsäläinen, Roni Winik, Jonilyn L. Yoder, Franco Nori, Terry P. Orlando, Simon Gustavsson, and William D. Oliver, "Waveguide quantum electrodynamics with superconducting artificial giant atoms", Nature **583**, 775–779 (2020).

[196] Jun Rui, David Wei, Antonio Rubio-Abadal, Simon Hollerith, Johannes Zeiher, Dan M. Stamper-Kurn, Christian Gross, and Immanuel Bloch, "A subradiant optical mirror formed by a single structured atomic layer", Nature **583**, 369–374 (2020).

[197] Logan W. Clark, Nathan Schine, Claire Baum, Ningyuan Jia, and Jonathan Simon, "Observation of Laughlin states made of light", Nature **582**, 41–45 (2020).

[198] Avikar Periwal, Eric S. Cooper, Philipp Kunkel, Julian F. Wienand, Emily J. Davis, and Monika Schleier-Smith, "Programmable interactions and emergent geometry in an array of atom clouds", Nature **600**, 630–635 (2021).

[199] Yudan Guo, Ronen M. Kroeze, Brendan P. Marsh, Sarang Gopalakrishnan, Jonathan Keeling, and Benjamin L. Lev, "An optical lattice with sound", Nature **599**, 211–215 (2021).

[200] Eunjong Kim, Xueyue Zhang, Vinicius S. Ferreira, Jash Banker, Joseph K. Iverson, Alp Sipahigil, Miguel Bello, Alejandro González-Tudela, Mohammad Mirhosseini, and Oskar Painter, "Quantum electrodynamics in a topological waveguide", Phys. Rev. X **11**, 011015 (2021).

[201] Hideki Konishi, Kevin Roux, Victor Helson, and Jean-Philippe Brantut, "Universal pair polaritons in a strongly interacting fermi gas", Nature **596**, 509–513 (2021).

[202] Maximilian Zanner, Tuure Orell, Christian M. F. Schneider, Romain Albert, Stefan Oleschko, Mathieu L. Juan, Matti Silveri, and Gerhard Kirchmair, "Coherent control of a multi-qubit dark state in waveguide quantum electrodynamics", Nature Physics **18**, 538–543 (2022).

[203] Mi Lei, Rikuto Fukumori, Jake Rochman, Bihui Zhu, Manuel Endres, Joonhee Choi, and Andrei Faraon, "Many-body cavity quantum electrodynamics with driven inhomogeneous emitters", arXiv:2208.04345 (2022).

[204] Zeyang Li, Boris Braverman, Simone Colombo, Chi Shu, Akio Kawasaki, Albert F. Adiyatullin, Edwin Pedrozo-Peñafiel, Enrique Mendez, familyi=c., given=Vladan, giveni=V., ,, and, "Collective spin-light and light-mediated spin-spin interactions in an optical cavity", PRX Quantum **3**, 020308 (2022).

[205] Nick Sauerwein, Francesca Orsi, Philipp Uhrich, Soumik Bandyopadhyay, Francesco Mattiotti, Tigrane Cantat-Moltrecht, Guido Pupillo, Philipp Hauke, and Jean-Philippe Brantut, "Engineering random spin models with atoms in a high-finesse cavity", arXiv:2208.09421 (2022).

[206] Davide Dreon, Alexander Baumgärtner, Xiangliang Li, Simon Hertlein, Tilman Esslinger, and Tobias Donner, "Self-oscillating pump in a topological dissipative atom–cavity system", Nature **608**, 494–498 (2022).

[207] H. J. Carmichael, "Photon antibunching and squeezing for a single atom in a resonant cavity", Phys. Rev. Lett. **55**, 2790–2793 (1985).

[208] G. Rempe, R. J. Thompson, R. J. Brecha, W. D. Lee, and H. J. Kimble, "Optical bistability and photon statistics in cavity quantum electrodynamics", Phys. Rev. Lett. **67**, 1727–1730 (1991).

[209] Perry R. Rice and H. J. Carmichael, "Photon statistics of a cavity-qed laser: a comment on the laser–phase-transition analogy", Phys. Rev. A **50**, 4318–4329 (1994).

[210] H. J. Kimble, "Strong interactions of single atoms and photons in cavity QED", Physica Scripta **T76**, 127 (1998).

[211] H. J. Carmichael, "Breakdown of photon blockade: a dissipative quantum phase transition in zero dimensions", Phys. Rev. X **5**, 031028 (2015).

[212] N. Defenu, T. Donner, T. Macri, G. Pagano, S. Ruffo, and A. Trombettoni, "Long-range interacting quantum systems", arXiv:2109.01063 (2021).

[213] Linus Pauling, "The structure and entropy of ice and of other crystals with some randomness of atomic arrangement", Journal of the American Chemical Society **57**, 2680–2684 (1935).

[214] P. W. Anderson, "Ordering and antiferromagnetism in ferrites", Phys. Rev. **102**, 1008–1013 (1956).

[215] M. J. Harris, S. T. Bramwell, D. F. McMorrow, T. Zeiske, and K. W. Godfrey, "Geometrical frustration in the ferromagnetic pyrochlore $Ho_2Ti_2O_7$", Phys. Rev. Lett. **79**, 2554–2557 (1997).

[216] A. P. Ramirez, A. Hayashi, R. J. Cava, R. Siddharthan, and B. S. Shastry, "Zero-point entropy in 'spin ice'", Nature **399**, 333–335 (1999).

[217] Steven T. Bramwell and Michel J. P. Gingras, "Spin ice state in frustrated magnetic pyrochlore materials", Science **294**, 1495–1501 (2001).

[218] Michael Hermele, Matthew P. A. Fisher, and Leon Balents, "Pyrochlore photons: the U(1) spin liquid in a $S = \frac{1}{2}$ three-dimensional frustrated magnet", Phys. Rev. B **69**, 064404 (2004).

[219] A. W. Glaetzle, M. Dalmonte, R. Nath, I. Rousochatzakis, R. Moessner, and P. Zoller, "Quantum spin-ice and dimer models with rydberg atoms", Phys. Rev. X **4**, 041037 (2014).

[220] Louis-Paul Henry and Tommaso Roscilde, "Order-by-disorder and quantum coulomb phase in quantum square ice", Phys. Rev. Lett. **113**, 027204 (2014).

[221] Alessio Celi, Benoît Vermersch, Oscar Viyuela, Hannes Pichler, Mikhail D. Lukin, and Peter Zoller, "Emerging two-dimensional gauge theories in Rydberg configurable arrays", Phys. Rev. X **10**, 021057 (2020).

[222] Andrew D. King, Cristiano Nisoli, Edward D. Dahl, Gabriel Poulin-Lamarre, and Alejandro Lopez-Bezanilla, "Qubit spin ice", Science **373**, 576–580 (2021).

[223] P. W. Anderson, "The resonating valence bond state in La_2CuO_4 and superconductivity", Science **235**, 1196–1198 (1987).

[224] X. G. Wen, "Mean-field theory of spin-liquid states with finite energy gap and topological orders", Phys. Rev. B **44**, 2664–2672 (1991).

[225] N. Read and Subir Sachdev, "Large-n expansion for frustrated quantum antiferromagnets", Phys. Rev. Lett. **66**, 1773–1776 (1991).

[226] T. Senthil and Matthew P. A. Fisher, "Z_2 Gauge theory of electron fractionalization in strongly correlated systems", Phys. Rev. B **62**, 7850–7881 (2000).

[227] T. Senthil, Ashvin Vishwanath, Leon Balents, Subir Sachdev, and Matthew P. A. Fisher, "Deconfined quantum critical points", Science **303**, 1490–1494 (2004).

[228] C. Broholm, R. J. Cava, S. A. Kivelson, D. G. Nocera, M. R. Norman, and T. Senthil, "Quantum spin liquids", Science **367**, eaay0668 (2020).

[229] H. R. Kong, J. R. Taylor, Y. Dong, and K. S. Choi, "Observation of cavity-stabilized spin liquids in reactive many-body QED", arXiv:XXXX.XXXX (2022).

[230] Arezoo Mokhberi, Markus Hennrich, and Ferdinand Schmidt-Kaler, *Trapped Rydberg ions: a new platform for quantum information processing*, edited by Louis F. Dimauro, Hélène Perrin, and Susanne F. Yelin, Vol. 69, Advances In Atomic, Molecular, and Optical Physics (Academic Press, 2020), page 233.

[231] Konstantinos Orfanakis, Sai Kiran Rajendran, Valentin Walther, Thomas Volz, Thomas Pohl, and Hamid Ohadi, "Rydberg exciton–polaritons in a Cu_2O microcavity", Nature Materials **21**, 767–772 (2022).

[232] H. R. Kong, D. Byer, Y.-S. Lee, C. Liu, M. Moreno, M. Sabooni, R. Simpson, J. Taylor, C. Warner, and K. S. Choi, "An advanced apparatus for strongly-coupled many-body quantum electrodynamics", arXiv:XXXX.XXXX (2022).

[233] Yu-Ting Chen, Michal Szurek, Beili Hu, Julius de Hond, Boris Braverman, and Vladan Vuletic, "A high finesse bow-tie cavity for strong atom-photon coupling in Rydberg arrays", arXiv:2207.06876 (2022).

[234] Henning Labuhn, Daniel Barredo, Sylvain Ravets, Sylvain de Léséleuc, Tommaso Macrì, Thierry Lahaye, and Antoine Browaeys, "Tunable two-dimensional arrays of single Rydberg atoms for realizing quantum ising models", Nature **534**, 667–670 (2016).

[235] Hannes Bernien, Sylvain Schwartz, Alexander Keesling, Harry Levine, Ahmed Omran, Hannes Pichler, Soonwon Choi, Alexander S. Zibrov, Manuel Endres, Markus Greiner, Vladan Vuletić, and Mikhail D. Lukin, "Probing many-body dynamics on a 51-atom quantum simulator", Nature **551**, 579–584 (2017).

[236] Sylvain de Léséleuc, Vincent Lienhard, Pascal Scholl, Daniel Barredo, Sebastian Weber, Nicolai Lang, Hans Peter Büchler, Thierry Lahaye, and Antoine Browaeys, "Observation of a symmetry-protected topological phase of interacting bosons with Rydberg atoms", Science **365**, 775–780 (2019).

[237] Alexander Keesling, Ahmed Omran, Harry Levine, Hannes Bernien, Hannes Pichler, Soonwon Choi, Rhine Samajdar, Sylvain Schwartz, Pietro Silvi, Subir Sachdev, Peter Zoller, Manuel Endres, Markus Greiner, Vladan Vuletić, and Mikhail D. Lukin, "Quantum Kibble–Zurek mechanism and critical dynamics on a programmable Rydberg simulator", Nature **568**, 207–211 (2019).

[238] Sepehr Ebadi, Tout T. Wang, Harry Levine, Alexander Keesling, Giulia Semeghini, Ahmed Omran, Dolev Bluvstein, Rhine Samajdar, Hannes Pichler, Wen Wei Ho, Soonwon Choi, Subir Sachdev, Markus Greiner, Vladan Vuletić, and Mikhail D. Lukin, "Quantum phases of matter on a 256-atom programmable quantum simulator", Nature **595**, 227–232 (2021).

[239] Pascal Scholl, Michael Schuler, Hannah J. Williams, Alexander A. Eberharter, Daniel Barredo, Kai-Niklas Schymik, Vincent Lienhard, Louis-Paul Henry, Thomas C. Lang, Thierry Lahaye, Andreas M. Läuchli, and Antoine Browaeys, "Quantum simulation of 2d antiferromagnets with hundreds of Rydberg atoms", Nature **595**, 233–238 (2021).

[240] G. Semeghini, H. Levine, A. Keesling, S. Ebadi, T. T. Wang, D. Bluvstein, R. Verresen, H. Pichler, M. Kalinowski, R. Samajdar, A. Omran, S. Sachdev, A. Vishwanath, M. Greiner, V. Vuletić, and M. D. Lukin, "Probing topological spin liquids on a programmable quantum simulator", Science **374**, 1242–1247 (2021).

[241] M. Saffman, T. G. Walker, and K. Mølmer, "Quantum information with Rydberg atoms", Rev. Mod. Phys. **82**, 2313–2363 (2010).

[242] Federica M. Surace, Paolo P. Mazza, Giuliano Giudici, Alessio Lerose, Andrea Gambassi, and Marcello Dalmonte, "Lattice gauge theories and string dynamics in Rydberg atom quantum simulators", Phys. Rev. X **10**, 021041 (2020).

[243] Ruben Verresen, Mikhail D. Lukin, and Ashvin Vishwanath, "Prediction of toric code topological order from Rydberg blockade", Phys. Rev. X **11**, 031005 (2021).

[244] Rhine Samajdar, Wen Wei Ho, Hannes Pichler, Mikhail D. Lukin, and Subir Sachdev, "Quantum phases of Rydberg atoms on a kagome lattice", Proceedings of the National Academy of Sciences **118**, e2015785118 (2021).

[245] A Yu Kitaev, "Fault-tolerant quantum computation by anyons", Annals of Physics **303**, 2–30 (2003).

[246] Alexei Kitaev, "Anyons in an exactly solved model and beyond", Annals of Physics **321**, 2–111 (2006).

[247] Y. Dong, J. Taylor, H. R. Kong, and K. S. Choi, "Bootstrapping universal quantum simulator from many-body qed with dissipative constraints", arXiv:XXXX.XXXX (2022).

[248] Daniel Klaus Burgarth, Paolo Facchi, Vittorio Giovannetti, Hiromichi Nakazato, Saverio Pascazio, and Kazuya Yuasa, "Exponential rise of dynamical complexity in quantum computing through projections", Nature Communications **5**, 5173 (2014).

[249] F. Verstraete, V. Murg, and J.I. Cirac, "Matrix product states, projected entangled pair states, and variational renormalization group methods for quantum spin systems", Advances in Physics **57**, 143–224 (2008).

[250] G. Baskaran, Z. Zou, and P.W. Anderson, "The resonating valence bond state and high-tc superconductivity — a mean field theory", Solid State Communications **63**, 973–976 (1987).

[251] Ying Dong, J. Taylor, Youn Seok Lee, H. R. Kong, and K. S. Choi, "Waveguide-qed platform for synthetic quantum matter", Phys. Rev. A **104**, 053703 (2021).

[252] Leo Zhou and Dorit Aharonov, "Strongly universal hamiltonian simulators", arXiv:2102.02991 (2022).

[253] K. Stannigel, P. Hauke, D. Marcos, M. Hafezi, S. Diehl, M. Dalmonte, and P. Zoller, "Constrained dynamics via the zeno effect in quantum simulation: implementing non-abelian lattice gauge theories with cold atoms", Phys. Rev. Lett. **112**, 120406 (2014).

[254] A.M. Polyakov, "Quark confinement and topology of gauge theories", Nuclear Physics B **120**, 429–458 (1977).

[255] Wen-Jun Hu, Federico Becca, Alberto Parola, and Sandro Sorella, "Direct evidence for a gapless Z_2 spin liquid by frustrating néel antiferromagnetism", Phys. Rev. B **88**, 060402 (2013).

[256] Francesco Ferrari and Federico Becca, "Gapless spin liquid and valence-bond solid in the J_1-J_2 heisenberg model on the square lattice: insights from singlet and triplet excitations", Phys. Rev. B **102**, 014417 (2020).

[257] Henry Shackleton, Alex Thomson, and Subir Sachdev, "Deconfined criticality and a gapless $\mathbb{Z}_2$ spin liquid in the square-lattice antiferromagnet", Phys. Rev. B **104**, 045110 (2021).

[258] T.F. Gallagher, *Rydberg atoms*, Cambridge Monographs on Atomic, Molecular and Chemical Physics (Cambridge University Press, 1994).

[259] L Hartmann, W Dür, and H-J Briegel, "Steady-state entanglement in open and noisy quantum systems", Physical Review A **74**, 052304 (2006).